ELECTRON TRANSPORT THROUGH NANOSCOPIC STRUCTURES

A Dissertation

Presented to the Faculty of the Graduate School

of Cornell University

in Partial Fulfillment of the Requirements for the Degree of

Doctor of Philosophy

by

Stephan Braig

August 2005

© 2005 Stephan Braig

ALL RIGHTS RESERVED

ELECTRON TRANSPORT THROUGH NANOSCOPIC STRUCTURES

Stephan Braig, Ph.D.

Cornell University 2005

This doctoral dissertation is concerned with modeling electron transport through nanoscopic structures, such as quantum dots, metal particles, or molecules.

In **Chapter 2**, we consider statistical correlations between the heights of conductance peaks corresponding to two different levels in a Coulomb-blockaded quantum dot. Correlations exist for two peaks at the same magnetic field if the field does not fully break time-reversal symmetry as well as for peaks at different values of a magnetic field that fully breaks time-reversal symmetry.

In **Chapter 3**, we present a density-matrix rate-equation approach to sequential tunneling through a metal particle weakly coupled to ferromagnetic leads. Our formalism is valid for an arbitrary number of electrons on the dot, for an arbitrary angle between the polarization directions of the leads, and with or without spin-orbit scattering on the metal particle. Interestingly, we find that the density-matrix description may be necessary even for metal particles with unpolarized leads if three or more single-electron levels contribute to the transport current and electron-electron interactions in the metal particle are described by the 'universal interaction Hamiltonian'.

In **Chapters 4 and 5**, we consider transport through molecular devices with strong coupling to a single vibrational mode for the case that the vibration is damped by coupling to the environment. We focus on the weak tunneling limit,

for which a rate-equation approach is valid. The role of the environment can be characterized by a frequency-dependent frictional damping term and corresponding resonance frequency shift. We calculate current-voltage curves in Chapter 4 and find qualitative agreement between our theory and recent experiments on C_{60} single-molecule devices. In Chapter 5, we see that, depending on how the characteristic length scales of the van der Waals and electrostatic interaction of the molecule with the environment compare to each other, orthogonality catastrophe may appear or disappear, resulting in a smooth or discontinuous current-voltage curve, respectively.

Finally, in **Chapter 6**, we investigate the influence of electron-phonon coupling on the current through a metallic single-walled carbon nanotube. In particular, we consider the high-energy optical and zone-boundary phonons and calculate an effective high-bias electron scattering rate, which is close to the experimentally observed value.

BIOGRAPHICAL SKETCH

The author, Stephan Braig, was born in Regensburg, Germany, on May 16th 1978 as the third son of Dr. Christa Braig and Dr. Werner Braig. Growing up in Germany, he was in the fortunate situation to be provided with an education that was of high quality yet free. After elementary school, he attended the *Gymnasium* in Neutraubling, Germany, from which he graduated and received his *Abitur* with distinction (best of year) in June 1997, majoring in Physics, Mathematics, Latin, and Economics/Law. He then went on to study Physics and Mathematics at the University of Heidelberg, Germany, starting October 1997 and took the *Vordiplom* examination in Physics in April 1999, followed by the *Vordiplom* in Mathematics in July 1999. For the academic year 2000/2001, he was offered the opportunity to study at Cornell University as an exchange student. He accepted the generous offer by Cornell University to continue his studies as a full-time Ph.D. student in the Physics Department, motivated by a research project in Prof. Matthias Neubert's research group in Theoretical High-Energy Physics. Attracted by the field of Nanoscopic and Mesoscopic Physics, he joined Prof. Piet W. Brouwer's research group in Spring 2002 and completed his Ph.D. work in Theoretical Nanoscopic and Mesoscopic Physics as a member of the Laboratory of Atomic and Solid State Physics at Cornell University.

To my parents

ACKNOWLEDGEMENTS

"Eine Arbeit wie diese wird eigentlich nie fertig."

- Johann Wolfgang von Goethe

Translating Goethe into English is quite arguably a non-trivial task, but since this dissertation is supposed to be submitted in English, I will try my translation skills on the above quote: "Work like this is never really finished." More than just a grain of truth about the open-endedness of academic projects is encapsulated in this saying, which is why I owe it to a large number of people that my endeavor of obtaining a Ph.D. in Theoretical Physics has indeed come to a successful conclusion. I have to apologize in advance should I have forgotten to mention anyone who I should have mentioned.

First and foremost, I would like to thank my advisor Piet Brouwer for an amazing time as a member of his group. It is hard to imagine that I could have fared any better with a different advisor, both on a professional and on a personal level. I have nothing but the utmost respect for his physical insight, his knowledge, and his ethical values. I very much appreciate the numerous times we spent in his office brainstorming ideas or discussing how to best proceed in a calculation, and it reflects his approachability and his patience that he was always willing to provide me with alternative explanations or with more details on a subject that I had not fully understood yet. Whatever physical understanding of nanoscopic and mesoscopic systems I can claim as mine is for the most part due to Piet's toy models and to his ability to break down complex problems into digestible pieces.

Another major contribution to my graduate career came from Karsten Flensberg from the University of Copenhagen, who spent a sabbatical year at Cornell,

and with whom I ended up working very closely during his visit. I will never forget how much fun it was to discuss physics with him, while at the same time learning about his approach to problems and his techniques.

One could call it the foundation of my research efforts that was laid in my first year and a half at Cornell, which I spent working with Matthias Neubert. Again I was fortunate to have found an advisor who was willing to spend time explaining both techniques and the broader physical picture to me, and he helped me gain insight into research at the forefront of high-energy physics. I also appreciated the fact that he was very understanding and supportive when I told him about my plan to switch to Piet's group, motivated by my more prominent interest in nanoscale physics.

Much of the credit for submitting this dissertation is also due to the two other members of my Special Committee, Paul McEuen and Jim Sethna. I would already consider being at the same university a privilege, but receiving suggestions and constructive feedback from them naturally amounted to an even more exciting experience. Thank you very much for all the time and effort that went into guiding me through physical problems as well as for the trust in my skills. Along similar lines, I would like to thank Dan Ralph for his making time whenever I approached him for discussions, and Bob Buhrman for his help as leader of the IRG-A research section of the Cornell Center for Materials Research (CCMR), which provided me with funding under NSF grant no. DMR 0079992. Sparkling thanks to David Mermin for his contribution to the reception after my thesis defense in the form of a 'champagne endowment'.

I would have been much harder to endure an office without windows for a prolonged period of time without my office mate (and research group mate) Shaffique

Adam. Be it for discussions revolving around physics or everyday life, or simply for venting frustration, Shaffique was there and made graduate life more interesting and joyful. In the same spirit, I would like to thank Sourish Basu, who joined our office for my final year as a graduate student. I would also like to thank all other members of Piet's research group for their support and for sharing their ideas and insights, namely Markus Kindermann and Saar Rahav, as well as the former members Misha Polianski, Prashant Sharma, Michael Crawford, and Denis Gorokhov. Furthermore, many thanks to my fellow theoretical graduate students and postdocs on the 5th and 6th floor of Clark Hall for discussions and random conversations: Connie Chang, Siew-Ann Cheong, Valerie Coffman, Dan Goldbaum, Simon Gravel, Uzi Hizi, Yor Limkumnerd, Ivan Rankenburg, David Roundy, Theja de Silva, Pierre Thibault, Hande Üstünel, and Josh Waterfall. I owe the same tribute to the experimentalists that I sometimes dared to track down in their dungeons in the basement of Clark Hall: Ethan Bernard, Kirill Bolotin, Markus Brink, Scott Bunch, Alex Champagne, Luke Donev, Jacob Grose, Benjamin Hunt, Shahal Ilani, Dan Johnson, Ferdinand Kümmeth, Ethan Minot, Abhay Pasupathy, Sami Rosenblatt, Vera Sazonova, Gil Toombes, Jonathan Wrubel, Yuval Yaish, and Xinjian Zhou.

Administrative tasks as a graduate student would not have been as easy as they were had there not been the ubiquitous helping hands from the administrative staff, be it of the Physics Department (Deb Hatfield, Lisa Margosian, John Miner, Rosemary French), of the Laboratory of Atomic and Solid State Physics (Douglas Milton, Connie Wright, Becky Jantz, Larisa Vygran, Judy Wilson), or of the Cornell Center for Materials Research (Lynda Keister, Melinda Stelick, Ivan Johnson). Special thanks to Connie Wright for providing fruit macédoine for the

reception after my thesis defense. Thanks also to Nevjinder Singhota, Kevin Dilley, Juliane Bauer-Hutchinson, and the other Outreach folks for keeping me alive by continuously providing me with food in exchange for my involvement in the outreach program. Moreover, special thanks to the computer gurus in the basement of Clark Hall (Barry Robinson, Mitch Collinsworth, David Botsch) who always tried to the best of their knowledge to resolve any computer incident that was unplanned for. I am very grateful to Mary Schlarb, Mariah Sawyer, and all the other staff at the International Students and Scholars Office for their knowledgeable guidance in maintaining proper legal status in the United States, as well as to Veronica Blodgett and Demetra Dentes from Cornell Career Services for their career-related advice.

Pertaining to my role as Graduate Student Representative, I would like to thank the fellow members of the Council of Representative and of the Graduate and Professional Student Assembly for their work. In particular, I would like to thank the members of the Codes and Judicial Committee under chair Rich Helms for the professional yet friendly atmosphere in which we conducted our discussions. Thanks also to Tammy Bishop for desperately trying to accommodate the schedules of everyone involved.

Life at Cornell would not have been half the fun it turned out to be had I not taken advantage of the diverse course offerings at Cornell, in particular Cornell's language classes. I would like to thank the lecturers and teaching assistants of the French and Spanish sections of the Department of Romance Studies for putting up with me as a graduate student in my desire to learn new languages. In this spirit, I also thank whoever implemented the idea that graduate students can take or audit almost any class at Cornell. Many thanks to Melissa Coto for her patience

in improving my Spanish conversation skills and simply for indulging me with her company.

On the sportive side, I found a group of people at Cornell that were enthusiastic enough about ballroom dancing to inspire me to get out on the dance floor and to compete in International and American ballroom dances. I met some very special people as part of the ballroom crowd, and I would like to thank in particular Alvina Kittur for a wonderful time on and off the dance floor, as well as the other most prominent figures on the ballroom dance team for their support: Sonya Beletskaya, Alex Nemiroski, Andy Sfekas, Ellan Spero, and Kazuha Watanabe.

Surviving the long Ithaca winter (which, by the way, is by no means as harsh as everyone makes it out to be) was made quite easy by taking advantage of the skiing resort next door. Thanks to my fellow skiers Marko Nanias, Ethan Bernard, Shaffique Adam, and Jeandrew Brink for some great times on the slopes, even though Ethan succumbed to the dark side at some point and took on snowboarding for reasons beyond my comprehension. There are too many sportive activities to list all of them, but I would like to single out another one, namely horseback riding: many thanks to Donna Cassidy-Hanley for giving me instructions in the art of horseback riding that surpassed any instructions I had ever experienced.

The friends that I have found at Cornell provided and still provide an invaluable contribution to my life. In particular, I would like to thank Marko Nanias and Ethan Bernard for their eager participation in indulging in virtual realities (also thanks to Mark Wyman for joining us eventually) and for good times in general. The quasi-weekly lunch hour with the aforementioned people always provided ample opportunity to relax and, of course, to complain about the intricacies with which a graduate student is faced. Many thanks to Steve Drasco, Tanja Hinderer,

and Etienne Racine for their Skat endeavors, as well as to Nick Jones and Quentin Mason simply for being the Aussie and Brit that they are. Many thanks also to Sash Sarangi for spending a week discovering San Francisco with me.

There are quite a few friends that I have not mentioned yet since they do not really fit into any of the above categories, but who were simply fun to hang out with (I guess that is enough of a category): Faisal Ahmad, Maurizio Chinchio, Chris Deufel, Sean Garner, Saikat Ghosh, Dan Hertz, Jim van Howe, Jay Hubisz, Björn Lange, Louis Leblond, Jason Marshall, Bridget Meeds, Gil Paz, Deniz Sezer, Matthew Shepherd, Ben Shlaer, and Nick Taylor. I would also like to mention some of my dear friends from Germany with whom I somehow managed to stay in touch over the years and who do not mind being called up after a long time of no communication: Sandra Normann, Anna and Regina Sanders, Tanja Stenzel, and Hendrik Lambrecht.

I saved the final paragraph for arguably the most influential group of people: my family, in particular my parents. They have always been there to support me, to give advice when asked (or even when not asked), or simply to cheer me up. I cannot recall a single instance during my obtaining the Ph.D. in which my parents were not willing to listen to my thoughts and concerns, be it late at night or early in the morning. I lack the words to describe how grateful I really am for the support that they have given me, both morally and in monetary form, and for the sacrifices that they have made in order to enable me to pursue my dreams.

Ithaca, August 2005

TABLE OF CONTENTS

Biographical Sketch . . . iii
Acknowledgements . . . v
List of Figures . . . xiv
List of Symbols . . . xvi
List of Publications . . . xx

1 Introduction **1**
1.1 Quantum Dots and Molecules . . . 2
1.1.1 Rate equations . . . 2
1.1.2 Wave-function correlations in quantum dots . . . 6
1.1.3 Tunneling through molecules . . . 9
1.2 Useful Facts about (Metallic) Carbon Nanotubes . . . 11
1.2.1 Nanotube classification . . . 11
1.2.2 Electronic band structure and Fermi points . . . 13
1.2.3 Metallic versus non-metallic nanotubes . . . 18
1.2.4 Electron-phonon coupling . . . 22

Bibliography for Chapter 1 **24**

2 Conductance Peak Height Correlations for a Coulomb-Blockaded Quantum Dot in a Weak Magnetic Field **26**
2.1 Introduction . . . 26
2.2 RMT Model . . . 28
2.3 Wave-Function Correlations and Peak-Height Correlator . . . 31
2.3.1 Weak magnetic field . . . 32
2.3.2 Different large magnetic fields . . . 35
2.4 Application to Spin-Orbit Scattering and Spectral Scrambling . . . 38

Bibliography for Chapter 2 **41**

3 Rate Equations for Coulomb Blockade with Ferromagnetic Leads **43**
3.1 Introduction . . . 43
3.2 Matrix Rate-Equation Formalism . . . 46
3.2.1 Single doubly degenerate level . . . 46
3.2.2 General formalism . . . 50
3.2.3 Unpolarized leads . . . 51
3.3 Application to Spin-Polarized Transport . . . 54
3.3.1 Single doubly occupied level . . . 54
3.3.2 Case of up to three electrons on the dot . . . 55
3.4 Influence of Spin-Orbit Scattering . . . 62
3.5 Conclusion . . . 63

Bibliography for Chapter 3 **65**

4 Vibrational Sidebands and Dissipative Tunneling in Molecular Transistors **68**
4.1 Introduction . . . 68
4.2 Model Hamiltonian . . . 72
4.3 Rate Equations and Current Formula . . . 76
4.4 Without Coupling to the Environment . . . 78
4.5 With Coupling to the Environment . . . 80
4.6 Models for $\mathcal{S}(\omega)$ . . . 82
4.6.1 Frequency-independent quality factor Q . . . 82
4.6.2 Coupling to a substrate . . . 86
4.7 I-V Curves . . . 92
4.8 Summary and Discussion . . . 95
4.8.1 Summary . . . 95
4.8.2 Comparison with experiments . . . 96

Bibliography for Chapter 4 **99**

5 Dissipative Tunneling and Orthogonality Catastrophe in Molecular Transistors **101**
5.1 Introduction . . . 101
5.2 Model Hamiltonian . . . 109
5.3 Current Formula . . . 115
5.4 Influence of the Coupling to the Environment . . . 116
5.5 Summary and Discussion . . . 122

Bibliography for Chapter 5 **124**

6 Electron-Phonon Scattering in Metallic Carbon Nanotubes **126**
6.1 Introduction . . . 126
6.2 Electron-Phonon Scattering Hamiltonian . . . 131
6.3 Relevant Scattering Processes . . . 133
6.4 Band Gap and Scattering Matrix Element . . . 135
6.5 Fermi's Golden Rule and Factors of Two . . . 139
6.5.1 Zone-boundary phonons with nonzero $\mathbf{q} \approx \pm 2\mathbf{k}_F$ . . . 139
6.5.2 Optical and acoustic phonons with $\mathbf{q} \approx 0$ . . . 140
6.6 Thermal Occupation . . . 141
6.7 Results for the Mean Free Paths . . . 142

Bibliography for Chapter 6 **145**

A Chapter 3: Rotation Matrices **147**
A.1 Two Dimensions: Spin-1/2 Doublet . . . 147
A.2 Three Dimensions: Spin-1 Triplet . . . 148

A.3 Four Dimensions: Spin-3/2 Quadruplet 148
A.4 Four Dimensions: Spin-1/2 Quadruplet 149

B Chapter 6: Symmetry Argument for Electron-Phonon Coupling 151

LIST OF FIGURES

1.1 Equivalent circuit for a quantum dot. 3
1.2 Hexagonal lattice structure of a graphene sheet. 12
1.3 Reciprocal lattice of graphene. 14
1.4 Electronic band structure of graphene close to the Fermi level. . . . 16
1.5 Two independent sets of Fermi points in graphene. 17
1.6 Stripes of allowed electron momenta in nanotubes. 19
1.7 Sketch of the electronic energy bands near the Fermi level. 20

2.1 Schematic of the quantum dot. 29
2.2 Conductance correlations in the GOE-GUE crossover. 34
2.3 Conductance correlations in the GUE-GUE crossover. 37

3.1 Metal particle attached to two ferromagnetic leads. 47
3.2 Spin on the dot as a function of source-drain voltage. 59
3.3 Excerpt from the conductance peak spectrum. 60
3.4 Normalized conductance peaks for different polarization orientations. 61

4.1 Illustration of the molecular transistor. 70
4.2 I-V characteristics without coupling to the environment. 79
4.3 The function $F(\xi)$ and its integral for different values of g and frequency-independent Q. 84
4.4 The integral of the function F for $g = 4$ and different Q at zero temperature. 85
4.5 Frictional damping term $\mathcal{S}(\omega)$. 90
4.6 The function $F(\xi)$ and its integral for different values of g, making use of Eq. (4.56) for $\mathcal{S}(\omega)$. 91
4.7 I-V characteristics for $g = 0.5$, 1, 2, and frequency-independent $Q = 5$ at zero temperature. 93
4.8 I-V characteristics for $g = 0.5$, 1, and 2 using Eq. (4.56) for $\mathcal{S}(\omega)$ at zero temperature, calculated for a C_{60} molecule on gold. 94
4.9 Example of a fit to the experimental curves of Ref. [2] using the substrate model (4.56) for a C_{60} molecule on gold, with $g = 2$ and $D/D_0 = 0.75$. 97

5.1 Illustration of the molecule attached to a substrate. 103
5.2 Electric fields induced by a charge on the molecule. 105
5.3 Sketch of the difference between dipolar (dashed line) and monopolar case (solid line) in the I-V characteristics. 108
5.4 Size of the discontinuity in the I-V characteristics. 121

6.1 Sketch of the possible phonon scattering processes for right movers at approximately half-filled bands. 134

6.2 Sketch of the electronic band structure in a metallic SWNT with and without backscattering. 137

B.1 Transverse and longitudinal optical mode in an armchair nanotube. 152

LIST OF SYMBOLS

Notation	Description
$\mathbf{r}$	Boldface font indicates vector quantity
r	Italic font indicates scalar (absolute value for vectors)
$\dot{x}$	Time derivative of variable x
∂_x, $\partial/\partial x$	Partial derivative with respect to x
D_x	Derivative operator $\partial_x x \partial_x$
$[a, b]$	Commutator $ab - ba$
$\{a, b\}$	Anti-commutator $ab + ba$
$\vert \dots \vert$	Absolute value
$(\dots)^\dagger$	Hermitian conjugation
$(\dots)^T$	Transposition
$\langle \dots \vert$, $\vert \dots \rangle$	Dirac bra and ket
$\langle \dots \rangle$	Chap. 2: probability average; Chaps. 4 & 5: thermal average
$\langle \dots \rangle_\rho$	Probability average performed at constant ρ
$\langle \dots \rangle_c$	Connected part of a probability average
$P(\dots)$	Probability distribution
$P_c(\dots)$	Connected part of joint probability distribution
$\mathrm{P}\int \dots$	Cauchy principal value
Re, Im	Real and imaginary part
tr M	Trace of matrix M

Symbol	Description
a_p	Displacement amplitude
$\mathbf{a}_1$, $\mathbf{a}_2$	Two-dimensional hexagonal lattice vectors
α	Lead/branch index; Chap. 2: GOE-GUE crossover parameter
$B(\omega)$, $B^R(\omega)$	Phonon Green's functions
$\mathbf{B}$	Magnetic field vector
β_j	Coupling between x_0 and x_j
c	Speed of light
C_d	Capacitance of the quantum dot
C_g	Gate capacitance
$C_{\mu\nu}$	First moment of $P_c(g_\mu, g_\nu)$
D	Spread of van der Waals interaction
D_0	Diameter of the C_{60} molecule, approx. 10.4Å
$D^\alpha_{\mathbf{k},\mathbf{q}}$	Electron-phonon scattering matrix element
$\mathbf{D}(\mathbf{k}, \mathbf{k}')$	Dynamical matrix of the substrate
δ_{mn}	Kronecker delta
$\delta(\mathbf{x})$	Delta function

Symbol	Description
Δ	Mean energy level spacing of the dot
$\Delta_{\mathbf{q}}$	Band gap induced by phonon mode $\mathbf{q}$
$\Delta(\omega)$	Measure of electrostatic versus van der Waals interaction
e	Electron charge
E_C	Charging energy of the system
E_T	Thouless energy
ε_0	Chap. 3: energy of zero occupation
	Chaps. 4 & 5: molecular electronic energy level
$\varepsilon_{\mathbf{k}}$	Energy of mode $\mathbf{k}$
ε_R, ε_L	Energy of right- or left-moving electron
f_α	Electronic distribution function for lead α
f_k	Two-dimensional Fourier-Bessel transform of $f(r)$
f_k^R, f_k^L	Electronic distribution function for right and left movers
$f(\mathbf{r})$	Spatial distribution of van der Waals interaction
$f^R(\varepsilon)$, $f^L(\varepsilon)$	Electronic distribution function for right and left movers
$F(\omega)$	Generalized Franck-Condon factor including dissipation
$F_0(\omega)$	$F(\omega)$ without coupling to the environment
$\mathcal{F}$	Van der Waals force on the molecule
g	Chaps. 2 & 3: dimensionless conductance;
	Chaps. 4 & 5: oscillator coupling strength
g_μ	Dimensionless conductance peak height for energy level μ
$g(\mathbf{r})$	Spatial distribution of electrostatic interaction
G	Linear-response conductance
$\mathbf{G}_1$, $\mathbf{G}_2$	Reciprocal lattice vectors for the hexagonal lattice
$\mathbf{G}(\mathbf{r})$	Electrostatic force on the substrate
γ_α, $\bar{\gamma}_\alpha$	Spinor tunneling amplitudes
$\gamma^{\pm}_{\alpha;k,k'}$	Many-electron tunneling amplitudes for lead α
Γ (Γ_α)	Tunneling rate (through lead α)
Γ_{ij}	Transition rate between initial state j and final state i
h ($\hbar$)	Planck's quantum constant ($h/2\pi$)
I (I_α)	Current (through lead α)
$I_n(z)$	Modified n^{th} Bessel function of the first kind
J	Exchange interaction strength
k_B	Boltzmann constant
k_M	Spring constant modeling van der Waals potential
$\mathbf{k}_F$	Fermi wave vector
$K_n(x)$	Modified n^{th} Bessel function of the second kind
l	Mean free path
ℓ_T	Length after which electrons have obtained the phonon energy
ℓ_{hp}	Scattering length off high-energy phonons
ℓ_{low}, ℓ_{high}	Low- and high-bias mean free path
ℓ_{ac}, ℓ_{op}, ℓ_{zb}	Scattering length off acoustic, optical, zone-boundary phonons

Symbol	Description
L	Chap. 2: linear dot size; Chap. 6: length of the nanotube
λ (λ_j)	Coupling between x_0 (x_j) and the charge on the molecule
λ_L	Elastic Lamé coefficient
m_0	Mass of the molecule
m_j	Masses of environmental phonons
m_α ($\bar{m}_\alpha$)	Spinor (anti-)parallel to the polarization direction of lead α
μ_L	Elastic Lamé coefficient
$n_\alpha(\varepsilon)$	Fermi distribution function for lead α
$n_B(\varepsilon)$	Bose-Einstein distribution function
$N^\alpha(\varepsilon)$	Phonon distribution function for branch α
ν_α	Density of states in lead α
η	Real and positive infinitesimal number
p_n	Scalar occupation probability for state n
$\|\psi_\mathbf{k}\rangle$	Tight-binding wave function for wave vector $\mathbf{k}$
$\psi_\mu(\mathbf{r})$	Spatial electronic wave function of energy level μ
P (P_α)	Degree of polarization (of lead α)
Q	Quality factor
$\|\mathbf{R}_i\rangle$	Localized wave function for lattice site $\mathbf{R}_i$
R_{low}, R_{high}	Low- and high-bias resistance
R_{cont}	Contact resistance
$\rho_{\mu\nu}$ ($\tilde{\rho}_{\mu\nu}$)	Orthogonal (unitary) invariant
ρ_1, ρ_k	Single-electron and many-electron density matrix
ρ	Mass density; Chap. 3: density matrix
ρ_R	One-dimensional resistivity
S, S_z	Total spin and z component of spin
σ	Electron spin
σ_j	Pauli matrices
$\mathcal{S}(\omega)$, $\bar{\mathcal{S}}(\omega)$	Frictional damping term for x_0; $\bar{\mathcal{S}}(\omega) = \mathcal{S}(\omega) - \mathcal{S}(0)$
t (t_{ij})	Tight-binding hopping element (between sites i and j)
T	Temperature
T_R, T_L	Transmission probability for right or left contact
T_{xx}, T_{xr}	Components of the stress tensor
$\tau^\alpha_\mathbf{q}$	Electron-phonon scattering time
$u(\mathbf{r})$	Substrate displacement
$u^\alpha_\mathbf{q}$	Displacement of phonon mode $\mathbf{q}$ in branch α
u_0 (u^α_0)	Displacement normalization (for phonon branch α)
U ($\tilde{U}$)	Coulomb repulsion (shifted by phonon interaction)
v_F	Fermi velocity
v_k	Electron velocity for mode k
v_s, (v_l, v_t)	Sound velocity (longitudinal, transverse)
v_μ ($v_{\mu,m}$)	Eigenvector of random matrix (component m)

Symbol	Description
V	Bias voltage
V_g	Gate voltage
ω_0 ($\bar{\omega}_0$)	Molecular resonance frequency ($\bar{\omega}_0^2 = \omega_0^2 + \mathcal{S}(0)$)
ω_j	Frequencies of environmental phonons
$\omega_{\mathbf{q}}^{\alpha}$	Frequency of phonon mode $\mathbf{q}$ in branch α
$\omega_{\min}$	Smallest environmental phonon frequency
x_0	Center-of-mass coordinate of the molecule
x_j	Coordinates of environmental phonons
Ξ	Deformation potential

LIST OF PUBLICATIONS

Theoretical Condensed-Matter Physics

- Stephan Braig and Piet W. Brouwer,
  Rate Equations for Coulomb Blockade with Ferromagnetic Leads,
  Phys. Rev. B **71**, 195324 (2005).
  [Chapter 3]

- Stephan Braig and Karsten Flensberg,
  Dissipative Tunneling and Orthogonality Catastrophe in Molecular Transistors,
  Phys. Rev. B **70**, 085317 (2004).
  [Chapter 5]

- Ji-Yong Park, Sami Rosenblatt, Yuval Yaish, Vera Sazonova, Hande Üstünel, Stephan Braig, T. A. Arias, Piet W. Brouwer, and Paul L. McEuen,
  Electron-Phonon Scattering in Metallic Single-Walled Carbon Nanotubes,
  Nano Lett. **4**, 517 (2004).
  [Chapter 6]

- Stephan Braig and Karsten Flensberg,
  Vibrational Sidebands and Dissipative Tunneling in Molecular Transistors,
  Phys. Rev. B **68**, 205324 (2003).
  [Chapter 4]

- Stephan Braig, Shaffique Adam, and Piet W. Brouwer,
  Conductance Peak Height Correlations for a Coulomb-Blockaded Quantum Dot in a Weak Magnetic Field,
  Phys. Rev. B **68**, 035323 (2003).
  [Chapter 2]

Theoretical High-Energy Physics

- Thomas Becher, Stephan Braig, Matthias Neubert, and Alexander L. Kagan,
  Constraints on Light Bottom Squarks from Radiative B-Meson Decays,
  Phys. Lett. B **540**, 278 (2002).

- Thomas Becher, Stephan Braig, Matthias Neubert, and Alexander L. Kagan,
  Flavor-Change with Ultra-Light Sbottom and Gluinos,
  hep-ph/0112129.

Chapter 1

Introduction

In the following, we will give a brief overview of the material presented in subsequent chapters or elaborate on certain physical facts that are at the root of the theoretical phenomena treated in these chapters:

Chapter 2 deals with how correlations in quantum dot wave functions affect the conductance through the dot, see also Secs. 1.1.1 and 1.1.2.

Chapter 3 treats the formalism of density-matrix rate equations for metal grains connected to ferromagnetic leads, see also Sec. 1.1.1.

Chapters 4 and 5 are concerned with the coupling of transport electrons to vibrational modes in molecular transistors, see also Sec. 1.1.3.

Chapter 6 provides details on the coupling of electrons to high-energy phonons in metallic single-walled carbon nanotubes, see also Sec. 1.2.

1.1 Quantum Dots and Molecules

A quantum dot can be characterized as a confined region in space with dimensions in the range of nanometers, for instance a metal nanoparticle, a single molecule, or an area defined within a two-dimensional electron gas (2DEG) in GaAs heterostructures. In Fig. 1.1, we show the equivalent circuit for such a quantum dot: the confined region is coupled to leads by virtue of tunnel junctions with tunneling rates Γ_R and Γ_L, and we model the electrostatic influence of the environment by a gate capacitance C_g and a gate voltage V_g.

The small size of the quantum dot determines its physical features. Its small capacitance C_d leads to a large charging energy $E_C = e^2/2C_d$, which makes it hard to add electrons to the quantum dot. At low bias voltages and low temperatures, it can actually be impossible to add or remove an electron from the dot, a phenomenon commonly referred to as *Coulomb blockade*. Drawing from the quantum mechanical analog of "particle in a box" eigenenergies, its small size can also result in a separation between energy levels Δ that is large enough to make it necessary to describe the energy spectrum as a set of discrete energy levels rather than as a continuum of energies.

1.1.1 Rate equations

Apart from thermal broadening of the energy levels, we also need to take the tunneling broadening $\hbar\Gamma$ into account, which is due to the tunneling of electrons into and out of the confined region. Depending on whether we are faced with $\hbar\Gamma \ll k_B T, \Delta$ or $\hbar\Gamma \gg k_B T, \Delta$, different theoretical frameworks are applicable: the latter regime would require field-theoretical methods to incorporate the effect

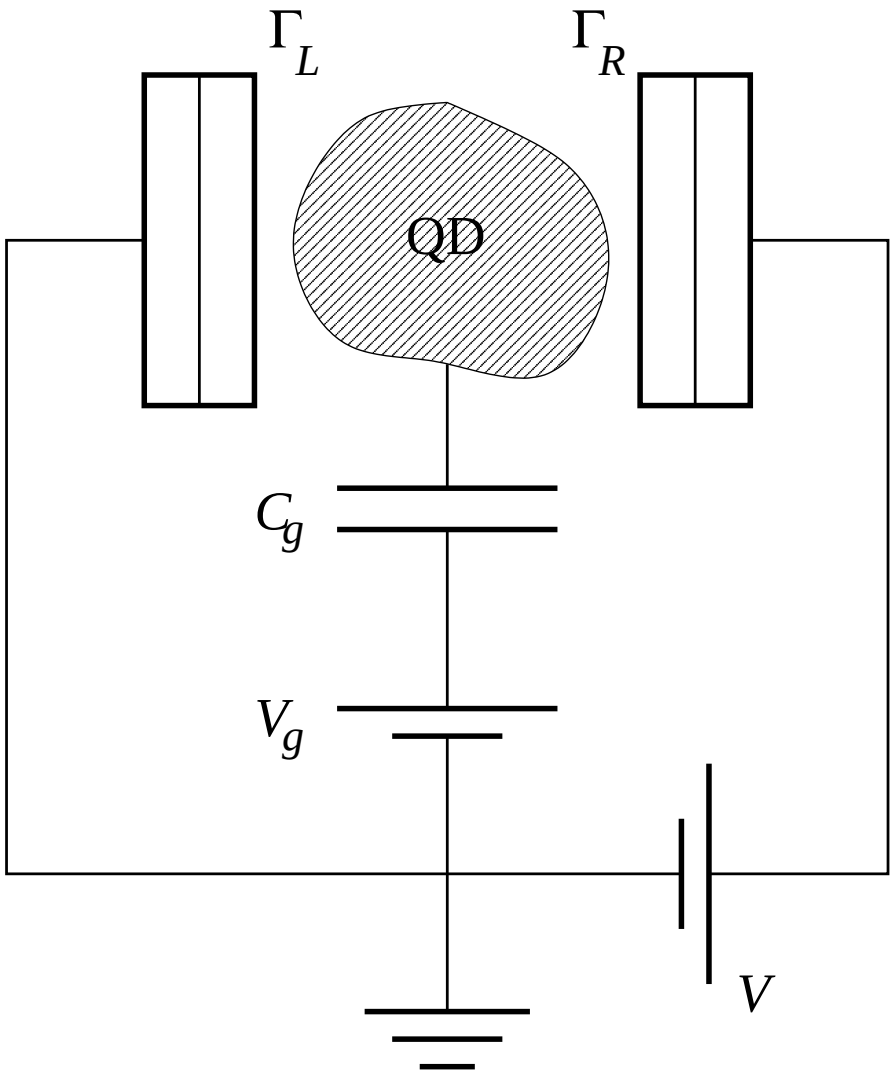

Figure 1.1: Equivalent circuit for a quantum dot.

The quantum dot is a confined region that is coupled to leads by virtue of tunnel junctions with tunneling rates Γ_R and Γ_L, and that is coupled capacitively (C_g) to a gate voltage V_g. The dot is biased by a voltage V.

of tunneling appropriately, whereas the former regime allows for leading order perturbation theory in the tunneling rates. Both Chapters 2 and 3 assume the tunneling rates to be within this perturbative regime, for which the formalism of rate equations has been shown to provide an accurate yet simple[1] description of the physics of electron transport through the quantum dot. The idea behind rate equations is that we have a set of states, labeled by n, with occupation probabilities p_n for each of the possible states. The tunneling of electrons allows for transitions between the different states with transition rates Γ_{ij}, where i and j label the initial state and final state, respectively. We can then write down equations that describe the time evolution of the set of probabilities $\{p_n\}$,

$$\dot{p}_n = \sum_j \left[\Gamma_{nj} p_j - \Gamma_{jn} p_n\right]. \tag{1.1}$$

In principle, one would now have to solve this set of coupled first-order differential equations in order to describe the dynamics of the system, which can be a non-trivial task. Life turns out to be much simpler if we are only interested in what happens in the steady state, which implies $\dot{p}_n = 0$ for all n. Fortunately, for many a situation, such a steady-state solution is indeed sufficient for understanding the physical phenomena exhibited by the system of interest. Rate equations have thus been tremendously successful in describing electron transport through nanoscopic or mesoscopic structures in the Coulomb blockade regime, in particular since they encapsulate interesting phenomena within a transparent and intuitive formalism.

Without any real justification, we simply assumed that we can identify and label the different states of the system (i.e., the quantum dot) by scalar probabilities p_n. In fact, the reason why Chapter 3 exists is that there are situations in which

[1] "Simple" compared to the full-fledged machinery of (non-)equilibrium quantum field theory.

scalar probabilities fail to describe the physics of the system at hand. One of the ramifications of having to describe the system quantum mechanically rather than classically is the appearance of coherent superpositions of states, a simple example of which is the coherent superposition of spin-up and spin-down states for a single electron.

For illustration purposes, suppose that we have a quantum dot with a single electronic level that can feature zero, single, or double occupation. In general, we would have to describe the occupation of the quantum dot by a 4×4 density matrix ρ (the singly occupied state has two orthogonal realizations, commonly labeled spin up and spin down) but since we work in the limit $\hbar\Gamma \ll E_C$, states corresponding to different occupation numbers are well separated in energy. In other words, the phase factor $e^{iE_C/\hbar\Gamma}$ associated with transitions between different occupation numbers oscillates so fast that all coherence is lost, and thus the off-diagonal elements in the density matrix that describe such superpositions of different occupation numbers are zero. Energy-degenerate states, on the other hand, remain phase coherent, which leads to non-zero entries in the density matrix. As a result, ρ reduces to block-diagonal form,

$$\rho = \begin{pmatrix} p_0 & 0 & 0 & 0 \\ 0 & \rho_1^{11} & \rho_1^{12} & 0 \\ 0 & \rho_1^{21} & \rho_1^{22} & 0 \\ 0 & 0 & 0 & p_2 \end{pmatrix}, \tag{1.2}$$

where p_0 and p_2 are scalar probabilities describing single and double occupation, respectively, whereas the ρ_1^{ij} are the elements of the 2×2 density matrix ρ_1 that describes the twofold-degenerate singly occupied state. The aforementioned scalar rate equations follow from the above if the symmetries of the system allow for

choosing a basis such that ρ is in fact fully diagonal.

Generalizing to multiple energy levels, we may need to resort to matrices of size up to $M \times M$, where M is the number of degenerate states available for coherent superposition, in order to appropriately describe the occupation "probabilities" on the quantum dot. The case of a normal metal particle connected to spin-polarized ferromagnetic leads provides for such a scenario that can make matrices necessary rather than scalars, and we elaborate on this in Chapter 3.

1.1.2 Wave-function correlations in quantum dots

Just as the eigenenergies of a particle in a box vary with the size of the box, the eigenenergies of a quantum dot depend on its size and shape, and so do the electronic wave functions that correspond to the eigenenergies. Even slight variations can induce a significant effect on the distribution of energy levels or on the spatial form of the wave functions in the dot. Since any two experimental setups are doomed to feature quite different microscopic details, it is therefore not sensible to try and develop a theory tailored to a particular dot shape. Rather, we would want to make statements that capture universal properties of ensembles of quantum dots. Experimentally, such ensembles do not necessarily have to be physically different dots but can also be the same dot in different regimes of its energy-level spectrum.

A very successful tool to describe such universal properties can be found in *random-matrix theory*. The basic idea behind random-matrix theory is to take a very large matrix that features the same symmetries as the quantum dot with matrix elements distributed according to an appropriately chosen probability dis-

tribution.[2] The eigenvalues of such a matrix turn out to correspond to a certain realization of energy levels in a quantum dot, and the eigenvectors map to the electronic wave functions [1], where the single eigenvector components can be interpreted as the value of the wave functions at certain locations in the quantum dot [2]. Taking an ensemble of such matrices and performing the average over the ensemble, we can thus make statements about universal properties of quantum dots that feature certain symmetries. It is important to note, however, that it is not known which matrix maps to which specific quantum dot, only the ensemble-averaged quantities can be mapped to each other.

The two symmetry classes relevant for Chapter 2 are the *Gaussian Orthogonal Ensemble* (GOE) and the *Gaussian Unitary Ensemble* (GUE). In simple terms, the GOE consists of real symmetric matrices and corresponds physically to the situation that spin-rotation symmetry and time-reversal symmetry are preserved in the quantum dot. The GUE, on the other hand, consists of complex hermitian matrices and corresponds to the preservation of spin-rotation symmetry but to the breaking of time-reversal symmetry, which can be accomplished in experiments by a magnetic field that is weak compared to the Zeeman field. It is not only possible, however, to pick matrices from these pure ensembles, but rather we can define a "crossover" between the two pure regimes, which is for instance useful for studying what happens in the system at the onset of breaking time-reversal symmetry. Let S be a real and symmetric $N \times N$ matrix, and let A be a real and antisymmetric $N \times N$ matrix, both independently distributed with the same

[2]In most cases, a Gaussian distribution will be the distribution of choice in accord with the central-limit theorem.

Gaussian distribution, then we can model this crossover by the matrix

$$H = S + i\frac{\alpha}{\sqrt{2N}}A, \tag{1.3}$$

where we introduced the crossover parameter α, and N is large [3]. In fact, we can relate α to the magnetic field that breaks time-reversal symmetry, see Chapter 2, Eq. (2.5). For a more thorough treatment of symmetry classes and random-matrix theory in general, we refer to Ref. [3] and other literature as cited in Chapter 2.

Given a set of eigenvectors of these random matrices, it is an interesting question whether or not different eigenvectors v_μ (or even eigenvector components $v_{\mu,m}$) are correlated with each other, or whether they are independently distributed. Since Gaussian variables have zero mean, a convenient measure of such correlations are the orthogonal invariants [4]

$$\rho_{\mu\nu} \equiv v_\mu^T v_\nu. \tag{1.4}$$

Fluctuating $|\rho_{\mu\mu}|^2$, the so-called phase rigidity, indicates that eigenvector components within a single eigenvector are correlated, whereas nonzero and fluctuating $\rho_{\mu\nu}$ for $\mu \neq \nu$ is a sign of correlations between different wave vectors [4]. It turns out that, if both eigenvectors v_μ and v_ν are chosen from one of the pure ensembles GOE or GUE, then no correlations exist. The situation is quite different, however, if the v_μ are taken from the set of eigenvectors of (1.3) corresponding to the crossover regime. In this case, correlations between eigenvectors (i.e., between different quantum dot wave functions) and eigenvector components exist (i.e., between values of wave functions at different locations) [4]. Interestingly enough, correlations also appear for eigenvectors that are taken from the crossover for different large values of the crossover parameter α. Physically, the latter corresponds to correlations of wave functions for different magnetic fields.

Now that we have established that either different wave functions or the values of the same wave function at different locations can be correlated in certain regimes, the natural question to ask is how or whether these correlations can be observed in experiments. To this end, we turn our attention to the conductance through a Coulomb-blockaded quantum dot in Chapter 2. Solving the scalar rate equations of Sec. 1.1.1 in linear response for this scenario, Beenakker obtained an expression for the conductance as a function of bias and gate voltage in Ref. [5], and he was able to explain the experimentally observed appearance of peaks in the differential conductance through the dot. Furthermore, he related the conductance peak heights to the tunneling rates into and out of the quantum dot. For weak tunneling, the tunneling rates follow from Fermi's Golden rule as being proportional to the square of the electronic wave functions at the tunneling sites [2], hence a connection between the dot wave functions and the conductance peak heights is established. Correlations in the wave functions should therefore be visible in the conductance peaks, which is the topic of Chapter 2.

1.1.3 Tunneling through molecules

In Chapters 4 and 5, we will turn our attention to electrons tunneling through molecules, with special focus on the experiments performed by Park *et al.* [6] involving C_{60} buckeyballs in a transistor setup, see Fig. 4.1 in Chapter 4. In many ways, molecules like the C_{60} buckeyball share characteristics with quantum dots. They are well-defined regions in space, they are relatively small, and thus feature relatively large charging energies. As a result, they can exhibit the physical signatures of Coulomb blockade, and very much the same theoretical techniques can be applied to electron transport through molecules.

There is at least one important difference, though, that makes molecules even more special than quantum dots: in contrast to the spatially fixed and stationary quantum dots, molecules feature intrinsic vibrational modes as well as center-of-mass (displacement) modes, and the coupling of such vibrational modes to the electrons that are passing through the molecule opens up a whole new range of physical phenomena. Very striking evidence for the existence of such electron-phonon coupling was found for the first time in Ref. [6], where the discrete low-energy vibrational modes showed up as peaks in the differential conductance through the molecule. In particular, the center-of-mass mode that corresponds to the wiggling of the molecule in between the two leads was believed to have been detected, and Chapters 4 and 5 provide for additional theoretical evidence that this identification is indeed correct.

However, the main purpose of these two chapters is to shed light on how the electrons can dissipate energy into the leads as a result of this coupling to the vibrational modes, and how this dissipation channel influences the current-voltage (I-V) characteristics of the molecule. The reason why the molecular phonons can provide for an additional dissipation channel is that the molecular phonons are in turn coupled to the phonons in the leads, which we model as a bosonic bath of harmonic oscillators, and can thus loose their energy to these environmental phonons.

In Chapters 4 and 5, we will describe the tunneling electrons by virtue of the rate equation approach that we introduced in Sec. 1.1.1. This choice is justified by the parameters of the experiment in Ref. [6], which featured very small tunneling rates into and out of the molecule. (Other theoretical works have considered the opposite regime of strong tunnel coupling, see for instance Ref. [7].) Since the

tunneling rates Γ are small, the time scale $1/\Gamma$ that describes how long a tunneling electron remains on the molecule is rather large compared to all other time scales in the problem. In particular, any distortion of the equilibrium distribution of the environmental phonons can be assumed to disappear very fast. We therefore work with equilibrium (Bose-Einstein) distributions for the phonons. Non-equilibrium phonons, which can be relevant in particular for other tunneling regimes, have been focused on in different works, see for instance Refs. [8, 9].

1.2 Useful Facts about (Metallic) Carbon Nanotubes

Mostly without going into the details of the derivations, we will state general facts about single-walled carbon nanotubes (SWNT) that are useful for understanding the calculations outlined in Chapter 6. For a more rigorous and in-depth treatment of carbon nanotubes, we refer to Ref. [10].

1.2.1 Nanotube classification

One of the simplest ways by which one can construct a nanotube theoretically is by taking a graphene sheet and rolling it up into cylindrical form. If the diameter of the cylinder is on the order of nanometers, a nanotube is born. (The actual production of nanotubes is of course quite different, see for instance Ref. [11]) The atomic structure of a graphene sheet is described by a hexagonal lattice, see Fig. 1.2, and we therefore see that the atomic structure on the wall of the resulting nanotube relative to its cylinder axis will depend on which direction we choose as the "rolling direction". There are of course an infinite number of structures we

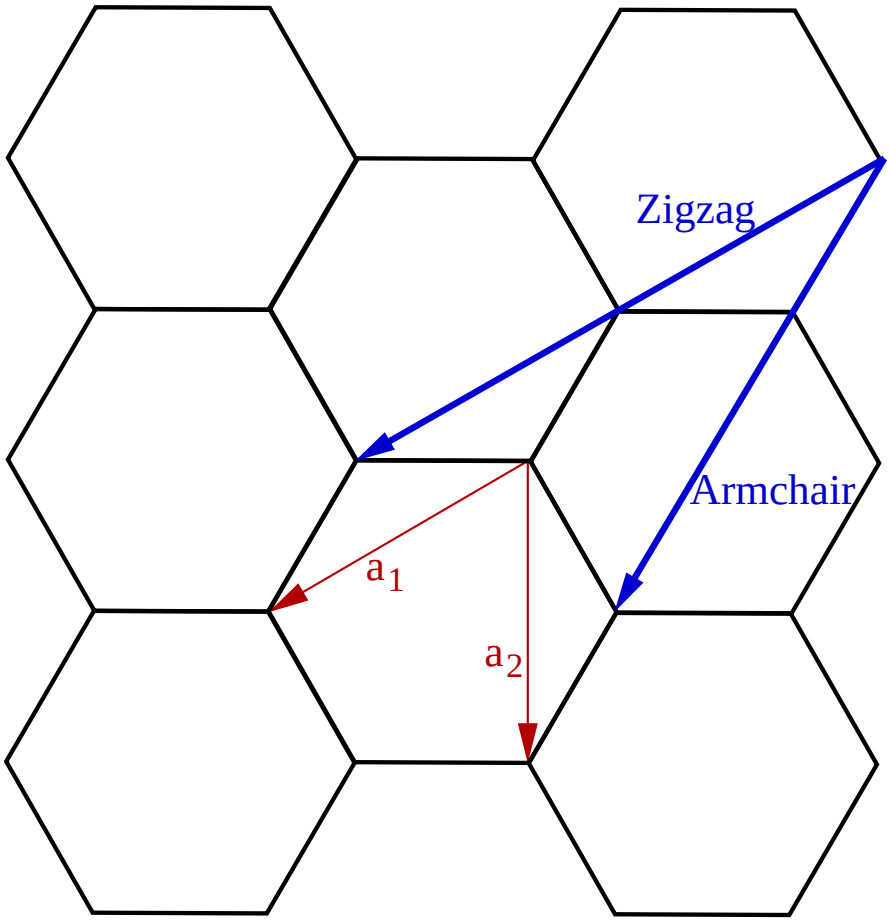

Figure 1.2: Hexagonal lattice structure of a graphene sheet.

In addition to the lattice vectors $\mathbf{a}_1$ and $\mathbf{a}_2$, we depict the directions in which the graphene sheet would have to be rolled in order to obtain a $(2, 0)$ zigzag nanotube or a $(1, 1)$ armchair nanotube, respectively.

could thus create, but one generally distinguishes between two main antagonists: armchair nanotubes and zigzag nanotubes. In Fig. 1.2, we indicate the rolling directions for these two types by vectors. Depending on which combination of lattice vectors $\mathbf{a}_1$ and $\mathbf{a}_2$ spans the circumference of the nanotube, we label them by integers n_1 and n_2 as (n_1, n_2) tubes, where all $(n, 0)$ tubes are zigzag tubes, whereas all (n, n) tubes are armchair tubes. The depicted rolling vectors correspond to a $(2, 0)$ zigzag tube and a $(1, 1)$ armchair tube, respectively.

1.2.2 Electronic band structure and Fermi points

The reciprocal lattice of a graphene sheet again features a hexagonal structure, as is depicted in Fig. 1.3, and the corner points coincide with the Fermi points for half-filled bands.[3] Within a tight-binding model, we can very easily determine the direction and length of the Fermi wave vector $\mathbf{k}_F$. Assuming that only nearest neighbors contribute, we can write down the following tight-binding Hamiltonian

$$H_{\mathrm{tb}} = \sum_{\mathbf{R}_i} \left[\varepsilon_i \left|\mathbf{R}_i\right\rangle \left\langle \mathbf{R}_i\right| + \sum_{\mathbf{r}_j \in \mathrm{N.N.}} t_{ij} \left|\mathbf{R}_i\right\rangle \left\langle \mathbf{r}_j\right| \right], \tag{1.5}$$

where $|\mathbf{R}_i\rangle$ is the local wave function at lattice site $\mathbf{R}_i$, ε_i is the on-site energy, t_{ij} is the hopping matrix element between lattice sites $\mathbf{R}_i$ and $\mathbf{R}_j$, and the summation over $\mathbf{r}_j$ extends over nearest neighbors only. The electronic tight-binding wave function $|\psi_{\mathbf{k}}\rangle$ for wave vector $\mathbf{k}$ can then be written as [12]

$$\left|\psi_{\mathbf{k}}\right\rangle = \sum_{\mathbf{R}_j} e^{i\mathbf{k}\cdot\mathbf{R}_j} \left|\mathbf{R}_j\right\rangle, \tag{1.6}$$

[3] It turns out that the electron density in graphene is such that the bands are approximately half filled.

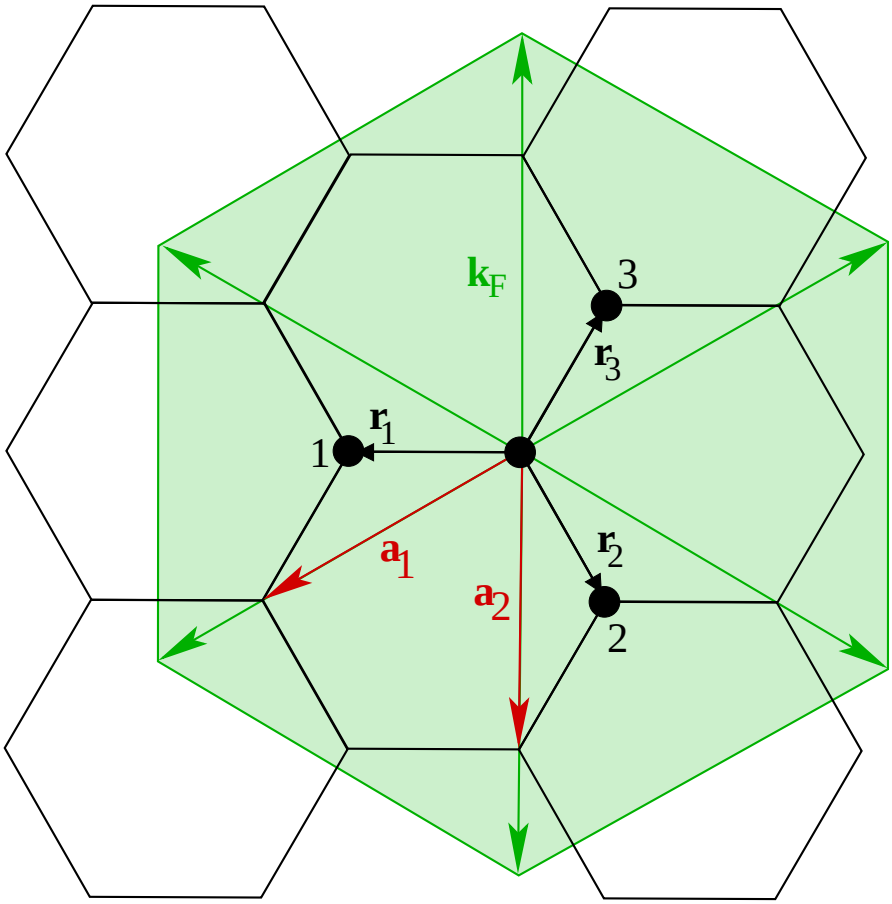

Figure 1.3: Reciprocal lattice of graphene.

The shaded area is the first Brillouin zone of the graphene lattice. For half-filled bands, the corner points coincide with the Fermi surface which form a set of six points.

and using the Schrödinger equation, we obtain

$$H_{\mathrm{tb}} \left|\psi_{\mathbf{k}}\right\rangle = \sum_{\mathbf{R}_i} \varepsilon_i e^{i\mathbf{k}\cdot\mathbf{R}_i} \left|\mathbf{R}_i\right\rangle + \sum_{\mathbf{R}_i} \sum_{\mathbf{r}_j \in \mathrm{N.N.}} t_{ij} e^{i\mathbf{k}\cdot\mathbf{r}_j} \left|\mathbf{R}_i\right\rangle . \tag{1.7}$$

Upon multiplication with $\langle\mathbf{R}_n|$ from the left, this results in the well-known formula for the tight-binding energy at lattice site n,

$$\varepsilon_{n,\mathrm{tb}} = \varepsilon_n + t \sum_{\mathbf{r}_j \in \mathrm{N.N.}} e^{i\mathbf{k}\cdot\mathbf{r}_j}, \tag{1.8}$$

where we defined $\varepsilon_{n,\mathrm{tb}} \equiv \langle\mathbf{R}_n| H_{\mathrm{tb}} \left|\psi_{\mathbf{k}}\right\rangle$, we chose $\mathbf{R}_n$ as the origin, and we made use of the fact that, in equilibrium and for nearest-neighbor interactions, all the t_{ij} are equal. For half-filled bands, the Fermi wave vector exactly coincides with the point at which the tight-binding contribution to the energy is zero, which implies that we can find the Fermi wave vector by solving

$$0 = \sum_{\mathbf{r}_j \in \mathrm{N.N.}} e^{i\mathbf{k}_F\cdot\mathbf{r}_j}. \tag{1.9}$$

From Fig. 1.3, we can immediately see that choosing $\mathbf{k}_F$ orthogonal to $\mathbf{r}_1$ in Fig. 1.3 makes the imaginary part of the right hand side disappear. The real part, on the other hand, allows us to determine the length k_F,

$$\cos\left(\frac{k_F|\mathbf{a}_1|}{2}\right) = -\frac{1}{2}, \qquad \Rightarrow \qquad k_F = \frac{4}{3}\frac{\pi}{|\mathbf{a}_1|}, \tag{1.10}$$

where $|\mathbf{a}_1| = |\mathbf{a}_2| = \sqrt{3}|\mathbf{r}_{1,2,3}|$ is the equilibrium graphene lattice constant.

In fact, calculating the full band structure for graphene close to the Fermi points results in a "double-cone" band structure as depicted in Fig. 1.4. For half-filled bands, we can see that the Fermi surface reduces to the aforementioned set of six Fermi points. Not all of these points are independent, rather we find that there are two independent sets of three Fermi points, each set featuring Fermi points that are related to each other by a reciprocal lattice vector. We display these two sets of Fermi points in Fig. 1.5.

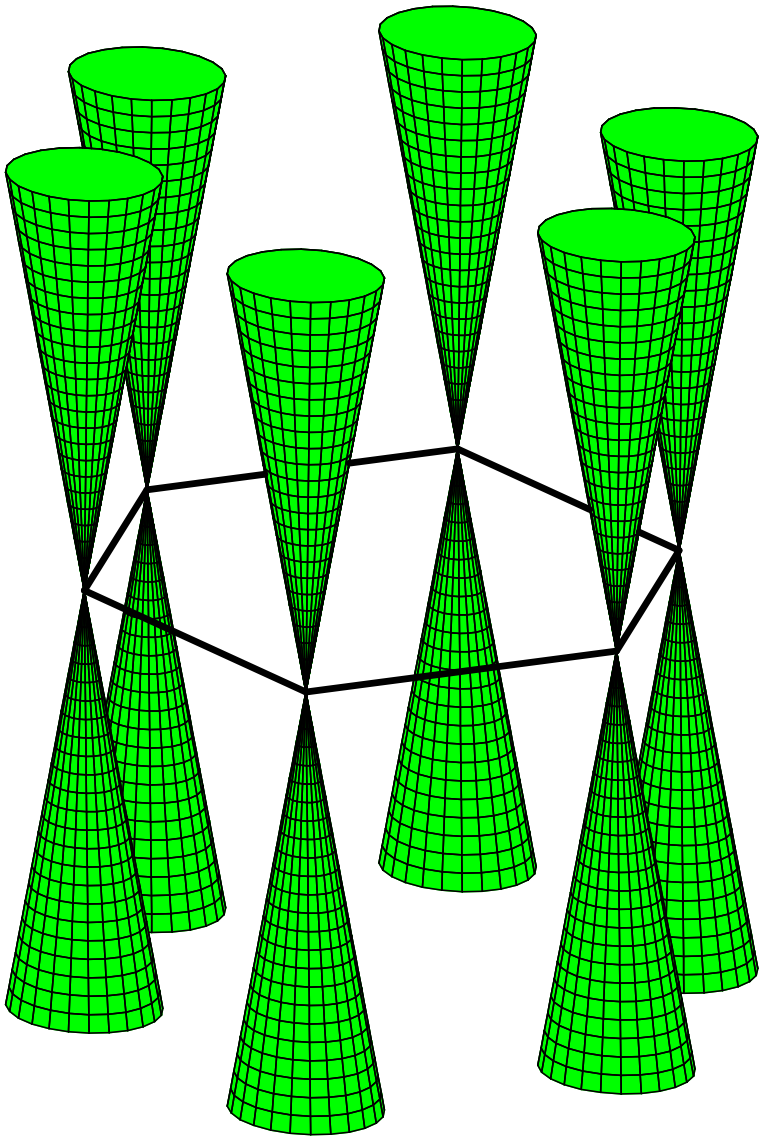

Figure 1.4: Electronic band structure of graphene close to the Fermi level.

The electronic band structure in momentum space close to the Fermi level is approximately given by double cones with tips touching at the Fermi points. The Fermi surface is therefore reduced to a set of six Fermi points. In fact, we only have two non-equivalent Fermi points since two sets of three Fermi points are related by reciprocal lattice vectors, see also Fig. 1.5.

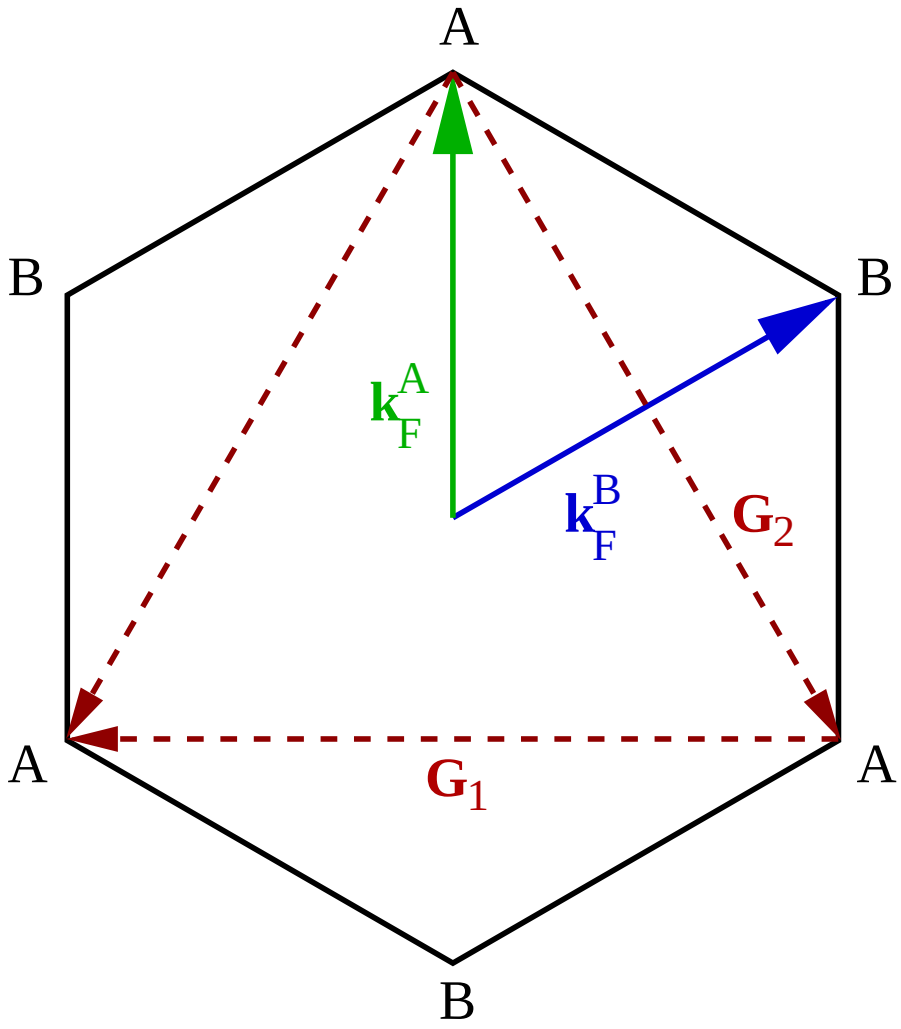

Figure 1.5: Two independent sets of Fermi points in graphene.

The two sets of Fermi points consist of the points labeled A and B, respectively. All A (B) points can be reached from any other point within the same set by virtue of a linear combination of reciprocal lattice vectors $\mathbf{G}_1$ and $\mathbf{G}_2$.

1.2.3 Metallic versus non-metallic nanotubes

One of the reasons why armchair nanotubes and zigzag nanotubes can be seen as antagonists is that armchair nanotubes are always metallic, whereas only a subset of zigzag nanotubes has metallic features. We can understand this from the following argument: perpendicular to the direction of the nanotube, we have periodic boundary conditions for the electronic wave functions due to the cylindrical form of nanotubes. This immediately leads to quantization of the transverse electron momenta since we need to impose that

$$e^{ik_\perp 2\pi r_{\mathrm{nt}}} = 1, \tag{1.11}$$

where r_{nt} is the radius of the nanotube. We therefore have stripes of allowed electron momenta that are parallel to the nanotube axis, see Fig. 1.6. Given the above quantization condition (1.11), we can see that the stripes are denser for larger diameter of the tube. The only invariant is the central stripe through the origin of the Brillouin zone.

Whether or not a nanotube is metallic or semiconducting is determined by whether or not there is a band gap at the Fermi level. For half-filled nanotubes, this immediately translates to whether or not one of the aforementioned stripes goes through one of the Fermi points (metallic) or not (semiconducting). As apparent from Fig. 1.6, armchair nanotubes are always metallic since the central stripe will always go through two Fermi points no matter what the diameter of the nanotube is. The situation is different for zigzag nanotubes since only specific diameters will result in quantization conditions consistent with a stripe going through a Fermi point. It turns out that such special quantization conditions are fulfilled for $(3n, 0)$ zigzag nanotubes, where n is an integer.

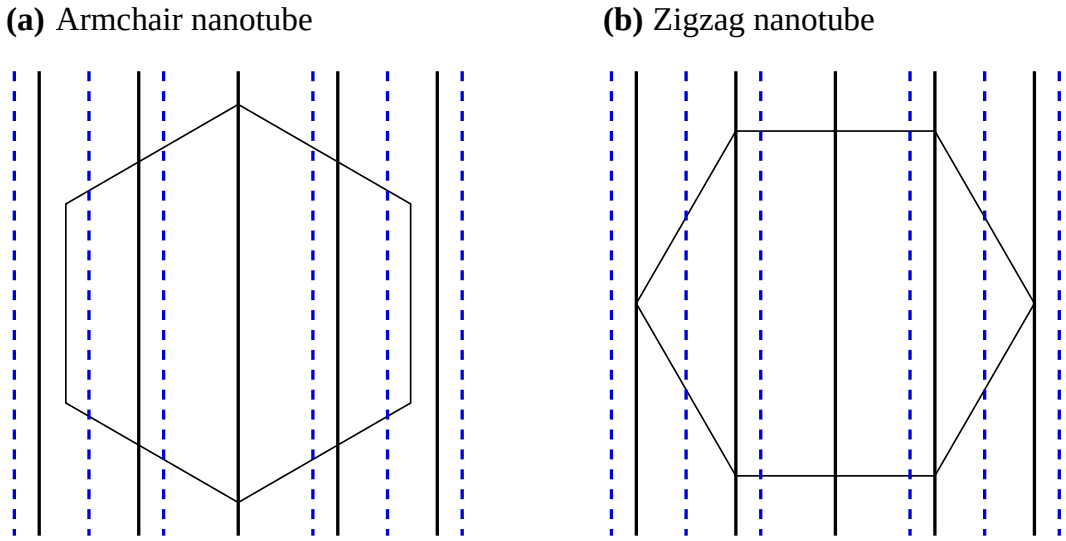

Figure 1.6: Stripes of allowed electron momenta in nanotubes.

We sketch the stripe structure of allowed electron momenta for **(a)** armchair and **(b)** zigzag nanotubes for two different diameters of the tube, depicted by solid and dashed stripes. Armchair tubes always feature at least one stripe that touches a Fermi point, whereas zigzag tubes vary in that regard: only $(3n, 0)$ nanotubes with n an integer (solid stripes in **(b)** as one example) feature quantization conditions such that stripes go through Fermi points. As a result, all armchair nanotubes are metallic, whereas only $(3n, 0)$ zigzag nanotubes are.

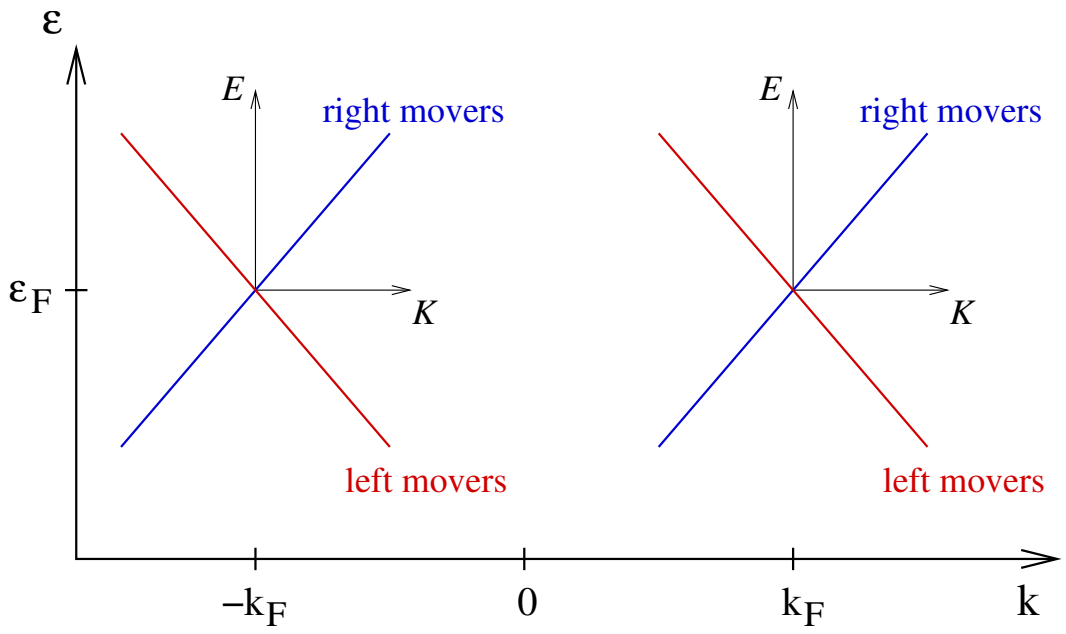

Figure 1.7: Sketch of the electronic energy bands near the Fermi level.

It can be convenient to define E as the energy relative to the Fermi energy. Since we have a linear dispersion relation about the Fermi points, we can easily define the wave vector K relative to $\pm k_F$, so that $E_{R/L}(K) = \pm\hbar v_F K$.

The stripes therefore define an effectively one-dimensional band structure, which can be approximated by a "double-cross" structure as depicted in Fig. 1.7. These crosses develop from cutting the electron cones of Fig. 1.4 along the stripes that go through the Fermi points.[4] Since there are two independent Fermi points, this reduced one-dimensional band structure features two crosses rather than only one.

The dispersion relation in the vicinity of the Fermi points is linear, but we have to distinguish between right and left movers, see Fig. 1.7. In this effective one-dimensional notation, we can write

$$\varepsilon_R(k) = \hbar v_F(k \mp k_F), \qquad \varepsilon_L(k) = \hbar v_F(-k \pm k_F), \tag{1.12}$$

where $\varepsilon_R(k)$ and $\varepsilon_L(k)$ are the energies for right-moving and left-moving electrons, respectively, the upper (lower) sign corresponds to the right (left) cross in Fig. 1.7, and $\hbar v_F k_F$ is the Fermi energy. We thus immediately see that the density of states $|\partial k/\partial\varepsilon| = (\hbar v_F)^{-1}$ for both right and left movers. It can turn out to be convenient to define energies E relative to the Fermi energy and to measure one-dimensional wave vectors K relative to k_F, which is indicated in Fig. 1.7 by the little coordinate systems at the two Fermi points. In this notation, we would have

$$E_R(K) = \hbar v_F K, \qquad E_L(K) = -\hbar v_F K, \tag{1.13}$$

for each of the two Fermi points.

[4]The next higher (lower) band corresponding to the neighboring stripe of allowed transverse electron momentum is so much higher (lower) in energy that it does not play any role for the electron-transport considerations in Chapter 6 and can therefore be neglected for our purposes.

1.2.4 Electron-phonon coupling

In Chapter 6, we consider the coupling between electrons and phonons in SWNTs, which constitutes a backscattering[5] mechanism that leaves its signature in the resistivity of the nanotube. In fact, we need to distinguish between the different types of phonons in order to identify their contribution to the resistivity, see also Fig. 6.1 in Chapter 6. At room temperature, the low-bias resistivity is determined by the low-energy acoustic phonons since the other high-energy phonons (such as breathing modes, optical phonons, or zone-boundary phonons) are not thermally populated at these temperatures nor can they be created due to the limited bias voltage. Both experimental measurements and theoretical estimates suggest that the acoustic-phonon scattering is weak with long mean free paths on the order of several hundred nanometers to several micrometers [13, 14, 15, 16, 17, 18, 19, 20]. At high enough bias voltages, the situation is different since high-energy phonons can be emitted. Yao *et al.* [21] showed that the corresponding high-energy phonon scattering rate is rapid enough to lead to a saturation of the current, but no exact value was extracted. It is therefore of interest to accurately determine the high-energy phonon scattering length, which, in conjunction with previously determined acoustic-phonon scattering lengths, allows for making statements about the strength of the electron-phonon coupling for all types of phonons.

In a recent paper [19], the mean free paths for electrons scattering off low-energy acoustic phonons and high-energy optical and zone-boundary phonons were investigated more thoroughly for a metallic single-walled carbon nanotube. The mean free paths in the low-bias regime (ℓ_{low}) and high-bias regime (ℓ_{high}) were

[5] "Backscattering" refers to scattering events that scatter right-moving electrons into the left-moving branch of the electronic dispersion, or vice versa.

extracted from the experimental I-V curves and were compared to theoretical estimates. The values that were found in this experiment suggested that ℓ_{high} is on the order of 10nm, in agreement with the general predictions of Ref. [21], and another experimental group independently found similar results [20]. Theoretical estimates for ℓ_{high} based on Fermi's Golden Rule resulted in values of the same order of magnitude, and the main subject of Chapter 6 is to show how these theoretical estimates were obtained and how the theoretical parameters relate to experimental observables.

BIBLIOGRAPHY

[1] C. W. J. Beenakker, Phys. Rev. B **44**, 1646 (1991).

[2] I. L. Aleiner, P. W. Brouwer, and L. I. Glazman, Phys. Rep. **358**, 309 (2002).

[3] C. W. J. Beenakker, Rev. Mod. Phys. **69**, 731 (1997).

[4] S. Adam, P. W. Brouwer, J. P. Sethna, and X. Waintal, Phys. Rev. B **66**, 165310 (2002).

[5] C. W. J. Beenakker, Phys. Rev. B **44**, 1646 (1991).

[6] H. Park, J. Park, A. K. L. Lim, E. H. Anderson, A. P. Alivisatos, and P. L. McEuen, Nature **407**, 57 (2000).

[7] K. Flensberg, Phys. Rev. B **68**, 205323 (2003).

[8] V. Aji, J. E. Moore, and C. M. Varma, cond-mat/0302222.

[9] A. Mitra, I. Aleiner, and A. J. Millis, Phys. Rev. B **69**, 245302 (2004).

[10] R. Saito, G. Dresselhaus, and M. S. Dresselhaus, *Physical properties of carbon nanotubes* (Imperial College Press, London, 1998).

[11] J. Kong, H. T. Soh, A. M. Cassell, C. F. Quate, and H. Dai, Nature **395**, 878 (1998).

[12] N. W. Ashcroft and N. D. Mermin, *Solid State Physics* (Saunders College Publishing, Orlando, 1976), p. 437-440.

[13] C. L. Kane, E. J. Mele, R. S. Lee, J. E. Fischer, P. Petit, H. Dai, A. Thess, R. E. Smalley, A. R. M. Verschueren, S. J. Tans, and C. Dekker, Europhys. Lett. 1998 **41**, 683 (1998).

[14] J. Appenzeller, R. Martel, P. Avouris, H. Stahl, and B. Lengeler, Appl. Phys. Lett. **78**, 3313 (2001).

[15] R. A. Jishi, M. S. Dresselhaus, and G. Dresselhaus, Phys. Rev. B **48**, 11385 (1993).

[16] H. Suzuura and T. Ando, Phys. Rev. B **65**, 235412 (2002).

[17] A. Bachtold, M. S. Fuhrer, S. Plyasunov, M. Forero, E. H. Anderson, A. Zettl, and P. L. McEuen, Phys. Rev. Lett. **84**, 6082 (2000).

[18] T. Hertel, R. Fasel, and G. Moos, Appl. Phys. A: Mater. Sci. Process. **75**, 449 (2002).

[19] J.-Y. Park, S. Rosenblatt, Y. Yaish, V. Sazonova, H. Ustunel, S. Braig, T. A. Arias, P. W. Brouwer, and P. L. McEuen, Nano Lett. **4**, 517 (2004).

[20] A. Javey, J. Guo, M. Paulsson, Q. Wang, D. Mann, M. Lundstrom, and H. Dai, Phys. Rev. Lett. **92**, 106804 (2004).

[21] Z. Yao, C. L. Kane, , and C. Dekker, Phys. Rev. Lett. **84**, 294 (2000).

Chapter 2

Conductance Peak Height Correlations for a Coulomb-Blockaded Quantum Dot in a Weak Magnetic Field

2.1 Introduction

Measurement of conductance peak heights in a Coulomb-blockaded quantum dot is one of few experimental tools to access properties of single-electron wave functions in quantum dots. Experimentally, the probability distribution of the conductance peak heights in quantum dots with an irregular shape was found to be in good agreement with predictions from random-matrix theory (RMT) [1], both without magnetic field and in the presence of a time-reversal symmetry breaking magnetic field [2, 3]. According to random-matrix theory, wave functions in a chaotic

quantum dot have a universal distribution, independent of details of the dot's shape or mean free path, and wave-function elements are independently Gaussian distributed real or complex numbers depending on the presence or absence of time-reversal symmetry, respectively. There are no long-range correlations within a chaotic wave function and no correlations between different wave functions [4, 5].

It is known that non-universal correlations between different wave functions and, hence, correlations between conductance peak heights exist in both ballistic and diffusive dots [6]. In ballistic quantum dots, such correlations are the result of wave-function scarring [7], which causes a slow modulation of the variance $\langle|\psi_\mu(\mathbf{r})|^2\rangle$ as a function of the level index μ and the position $\mathbf{r}$, although the RMT prediction for peak-height statistics remains valid for peaks at nearby energies [8]. The scarring effect disappears in the limit of large quantum dots, and is absent in quantum dots with scatterers smaller than the Fermi wavelength. In disordered quantum dots (mean free path l much smaller than dot size L), correlations between conductance peak heights are found to be of relative order $(\Delta/E_\mathrm{T})\ln(L/l)$ [5, 9], where E_T is the Thouless energy of the quantum dot and Δ the mean level spacing.

Here we address two other mechanisms for peak-height correlations. On the one hand, we investigate correlations at a weak perpendicular magnetic field that only partially breaks time-reversal symmetry. These correlations follow from underlying correlations of wave functions, which were reported previously in Ref. [10]. On the other hand, we also find correlations between peaks corresponding to different wave functions at two different values of a large magnetic field that fully breaks time-reversal symmetry. Unlike the two other causes for peak-height correlations, the source of correlations under investigation in this chapter is universal and survives in the limit of large quantum dots. Furthermore, these correlations are not only

of direct experimental relevance when Coulomb-blockade peaks are measured as a function of an external magnetic field, but our results also pertain to the case of quantum dots with weak spin-orbit scattering. We elaborate on this aspect at the end of the chapter.

This chapter is organized as follows: in Sec. 2.2, we introduce the Pandey-Mehta Hamiltonian, which is the RMT Hamiltonian appropriate for our calculations. We then proceed in Sec. 2.3 to formulate the problem in terms of orthogonal invariants of the Pandey-Mehta Hamiltonian and derive a general expression for the wave-function correlator distribution function. This result is employed to calculate the actual peak-height correlator distribution function whose first moment is compared to numerical RMT simulations, both for the case of a weak magnetic field (Sec. 2.3.1) and different large magnetic fields (Sec. 2.3.2). Finally, we apply our results to correlations in presence of spin-orbit coupling and to "spectral scrambling" in Sec. 2.4.

2.2 RMT Model

At temperatures $k_BT \ll \Delta$, the maximum conductance $G_\mu^{\rm peak}$ of a Coulomb-blockade conductance peak is a function of the wave function $\psi_\mu(\mathbf{r})$ of the resonant state $|\mu\rangle$ only [11, 12],

$$G_\mu^{\rm peak} = \left(\frac{e^2}{h}\frac{V\Delta}{\kappa k_BT}\right)\frac{T_L|\psi_\mu(\mathbf{r}_L)|^2 T_R|\psi_\mu(\mathbf{r}_R)|^2}{T_L|\psi_\mu(\mathbf{r}_L)|^2 + T_R|\psi_\mu(\mathbf{r}_R)|^2}. \tag{2.1}$$

Here, V is the area of the quantum dot, $\kappa = \frac{3}{2} + \sqrt{2}$, $\mathbf{r}_R$ and $\mathbf{r}_L$ are the positions of the tunneling contacts connecting the dot to source and drain reservoirs (see Fig. 2.1), and T_L, $T_R \ll 1$ are the transmission probabilities of the contacts. Equation (2.1) is valid in the experimentally relevant range of thermally broadened

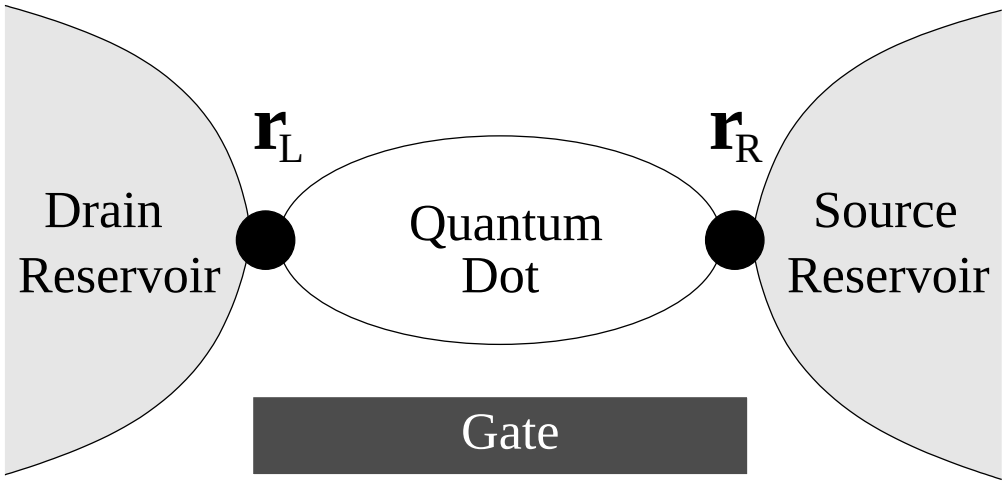

Figure 2.1: Schematic of the quantum dot.

The quantum dot is connected to source and drain reservoirs by tunneling contacts at $\mathbf{r}_R$ and $\mathbf{r}_L$ and is capacitively coupled to a gate.

conductance peaks, $(T_L + T_R)\Delta \ll k_B T \ll \Delta$. The index μ is defined with respect to the orbital state. In the presence of spin degeneracy, each orbital state gives rise to two conductance peaks, although these two peaks do not need to appear in succession [13, 14]. We express our results in terms of the distribution of the dimensionless peak height g_μ,

$$G_\mu^{\text{peak}} = g_\mu \left(\frac{e^2}{h} \frac{\Delta}{\kappa k_B T} \right) \frac{T_L T_R}{T_L + T_R}, \tag{2.2}$$

and calculate the connected part of the joint conductance peak height distribution for two different levels μ and ν,

$$P_c(g_\mu, g_\nu) = P(g_\mu, g_\nu) - P(g_\mu) P(g_\nu). \tag{2.3}$$

The single-peak distribution $P(g_\mu)$ for the case of weak magnetic fields was calculated by Alhassid *et al.* [15].

Within random-matrix theory, the effect of a magnetic field is described by the Pandey-Mehta Hamiltonian [16]

$$H(\alpha) = S + i \frac{\alpha}{\sqrt{2N}} A, \tag{2.4}$$

where S and A are symmetric and antisymmetric $N \times N$ matrices, respectively, with identical and independent Gaussian distributions. The parameter α is proportional to the magnetic field B,

$$\alpha = \gamma \frac{eBV}{hc} \sqrt{\frac{E_T}{\Delta}}, \tag{2.5}$$

where γ is a constant of order unity that depends on the precise geometry of the dot, for example $\gamma = \sqrt{\pi/2}$ for a diffusive disk of radius L ($E_T = \hbar v_F l / L^2$) and $\gamma = \pi/\sqrt{8}$ for a ballistic disk with diffusive boundary scattering ($E_T = \hbar v_F / L$) [17, 18, 19].

2.3 Wave-Function Correlations and Peak-Height Correlator

The joint distribution of eigenvectors of the Pandey-Mehta Hamiltonian (2.4) is determined by the orthogonal invariants $\rho_{\mu\nu} \equiv v_\mu^T v_\nu$, where the superscript T denotes transposition [10]. At fixed $\rho_{\mu\nu}$ and for large N, eigenvector components are distributed according to a multivariate Gaussian distribution with covariance matrix determined by the pair correlators

$$\langle v_{\mu,m}^* v_{\nu,n} \rangle_\rho = \frac{\delta_{mn}\delta_{\mu\nu}}{N}, \quad \langle v_{\mu,m} v_{\nu,n} \rangle_\rho = \frac{\delta_{mn}\rho_{\mu\nu}}{N}. \tag{2.6}$$

The distribution of the orthogonal invariants is known for the limiting cases $|\varepsilon_\mu - \varepsilon_\nu| \gg \Delta$ or $\alpha \gg 1$, when their distribution is Gaussian with zero mean and with variance [10]

$$\langle |\rho_{\mu\nu}|^2 \rangle = \frac{2\alpha^2(1+\delta_{\mu\nu})}{4\alpha^4 + \pi^2(\varepsilon_\mu - \varepsilon_\nu)^2/\Delta^2}. \tag{2.7}$$

Furthermore, if $|\varepsilon_\mu - \varepsilon_\nu| \gg \Delta$ or $\alpha \gg 1$, $|\rho_{\mu\mu}|^2$ and $|\rho_{\nu\nu}|^2$ are statistically independent. Eq. (2.7) is also valid in the limit $\alpha \ll 1$, if an additional average over the energy levels $\varepsilon_\mu - \varepsilon_\nu$ is taken. No analytical results are known for the distribution of the orthogonal invariants $\rho_{\mu\nu}$ when $\mu \neq \nu$, α is of order unity, and $|\varepsilon_\mu - \varepsilon_\nu| \lesssim \Delta$.

Using the correspondence between the eigenvectors of the Pandey-Mehta Hamiltonian and the wave functions in the quantum dot, we identify $\psi_\mu(\mathbf{r}_L)$ with $v_{\mu,1}$ and $\psi_\mu(\mathbf{r}_R)$ with $v_{\mu,2}$. We are interested in the joint distribution of the wave functions corresponding to the levels μ and ν and abbreviate $x_1 = N|v_{\mu,1}|^2$, $x_2 = N|v_{\mu,2}|^2$, $y_1 = N|v_{\nu,1}|^2$, and $y_2 = N|v_{\nu,2}|^2$. To leading order in $\rho_{\mu\nu}$, the connected part of an average of the form $\langle x_1^k x_2^l y_1^m y_2^n \rangle_c = \langle x_1^k x_2^l y_1^m y_2^n \rangle - \langle x_1^k x_2^l \rangle \langle y_1^m y_2^n \rangle$ can be calculated

with the help of Wick's theorem and Eq. (2.6),

$$\left\langle x_1^k x_2^l y_1^m y_2^n \right\rangle_c = \langle |\rho_{\mu\nu}|^2 \rangle \left[k^2 m^2 \left\langle x_1^{k-1} x_2^l \right\rangle \left\langle y_1^{m-1} y_2^n \right\rangle + l^2 n^2 \left\langle x_1^k x_2^{l-1} \right\rangle \left\langle y_1^m y_2^{n-1} \right\rangle \right].$$

In the regimes $|\epsilon_\mu - \epsilon_\nu| \gg \Delta$ or $\alpha \gg 1$, this relation allows us to express the connected part of the joint distribution function $P_c(x_1, x_2; y_1, y_2) = P(x_1, x_2; y_1, y_2) - P(x_1, x_2)P(y_1, y_2)$ in terms of the distribution functions $P(x_1, x_2)$ and $P(y_1, y_2)$ for elements of a single eigenvector,

$$P_c(x_1, x_2; y_1, y_2) = \frac{2\alpha^2}{4\alpha^4 + \pi^2(\varepsilon_\mu - \varepsilon_\nu)^2/\Delta^2} \sum_{j=1}^{2} D_{x_j} P(x_1, x_2) D_{y_j} P(y_1, y_2), \quad (2.8)$$

where $D_x \equiv \partial_x x \partial_x$. The distribution $P(x_1, x_2)$ for a single wave function of the Pandey-Mehta Hamiltonian was calculated by Fal'ko and Efetov [20].

2.3.1 Weak magnetic field

Using Eq. (2.8), the calculation of the peak-height correlation function $P_c(g_\mu, g_\nu)$ becomes a matter of quadrature. Closed-form results can be obtained for the case $\alpha \gg 1$,

$$P_c(g_\mu, g_\nu) = \frac{1}{2\alpha^2} e^{-g_\mu - g_\nu} (1 - g_\mu)(1 - g_\nu) \quad (2.9)$$

for highly asymmetric tunneling contacts ($T_L \ll T_R$), whereas for symmetric contacts ($T_L = T_R$)

$$P_c(g_\mu, g_\nu) = \frac{1}{16\alpha^2} W(g_\mu) W(g_\nu), \quad (2.10)$$

where the function W is a linear combination involving modified Bessel functions,

$$W(g) = 2g\, e^{-g} \left[(2 - 2g) K_0(g) + (1 - 2g) K_1(g) \right]. \quad (2.11)$$

The degree of correlation is well characterized by the first moment of $P_c(g_\mu, g_\nu)$,

$$C_{\mu\nu} = \langle g_\mu g_\nu \rangle - \langle g_\mu \rangle \langle g_\nu \rangle. \tag{2.12}$$

In the regime $\alpha \gg 1$ we find from Eqs. (2.9) and (2.10)

$$C_{\mu\nu} = \frac{1}{2\alpha^2} \quad \text{if } T_L \ll T_R, \tag{2.13a}$$

$$C_{\mu\nu} = \frac{1}{9\alpha^2} \quad \text{if } T_L = T_R. \tag{2.13b}$$

For very weak magnetic fields, $\alpha \ll 1$, evaluation of the correlator P_c requires knowledge of the $|\mu - \nu|$-level spacing distribution functions for the Gaussian Orthogonal Ensemble of random-matrix theory. Although the solution to this problem is known in the form of a product of eigenvalues of a certain integral equation [21], no closed-form expressions exist to the best of our knowledge. Moreover, if the energy levels μ and ν are nearest neighbors, small-α perturbation theory fails for small level separations. (Upon averaging over energy, Eq. (2.7) gives a logarithmic divergence.) This problem can be circumvented, noting that the orthogonal invariants $\rho_{\mu\nu}$, the only source of correlations if $\alpha \ll 1$, are completely determined by properties of the two energy levels under consideration. Therefore, the peak-height correlations may be calculated using a 2×2 Hamiltonian instead of the full $N \times N$ random matrix. In the eigenvector basis of the Pandey-Mehta Hamiltonian (2.4) at $\alpha = 0$, the appropriate two-level Hamiltonian reads

$$\mathcal{H} = \begin{pmatrix} \varepsilon_\mu & i\alpha A_{\mu\nu}/\sqrt{2N} \\ i\alpha A_{\nu\mu}/\sqrt{2N} & \varepsilon_\nu \end{pmatrix}, \tag{2.14}$$

where ε_μ and ε_ν are the two energy levels at $\alpha = 0$, and $A_{\mu\nu} = -A_{\nu\mu}$ is the corresponding matrix element of the perturbing matrix A, see Eq. (2.4). Solving for the eigenvectors of $\mathcal{H}$ and calculating the distribution of $\rho_{\mu\nu}$ exactly, we were able to compute the small-α behavior of the correlator $C_{\mu\nu}$ for $\nu = \mu + 1$,

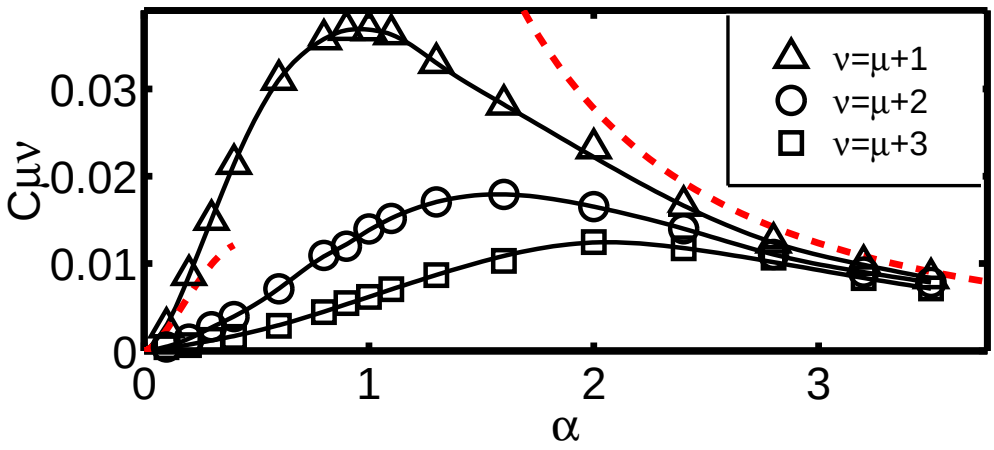

Figure 2.2: Conductance correlations in the GOE-GUE crossover.

The correlator $C_{\mu\nu}$ for energy levels μ and $\nu = \mu + 1$, $\mu + 2$, $\mu + 3$ for symmetric tunneling contacts, $T_L = T_R$. The data points are the result of numerical diagonalizations of the Pandey-Mehta Hamiltonian (2.4). The solid curves are drawn as a guide to the eye. The dashed lines show the large-α and small-α asymptotes (2.13b) and (2.15b), respectively.

$$C_{\mu\nu} \approx \frac{\alpha^2}{2\pi}\left(\ln\frac{4\pi}{\alpha^2} - 2\right) \quad \text{if } T_L \ll T_R, \tag{2.15a}$$

$$C_{\mu\nu} \approx \frac{3\alpha^2}{16\pi}\ln\frac{0.569}{\alpha^2} \qquad \text{if } T_L = T_R. \tag{2.15b}$$

The numerical coefficients inside the logarithms in Eqs. (2.15) were obtained by making use of the Wigner surmise $P(s) = (\pi s/2)\exp(-\pi s^2/4)$ as a numerical approximation to the distribution of nearest-neighbor spacings $s = |\varepsilon_{\mu+1} - \varepsilon_\mu|/\Delta$ [21].

A comparison of our results with the result of numerical diagonalizations of the Pandey-Mehta Hamiltonian is shown in Fig. 2.2 for the case of symmetric tunneling contacts. We used random matrices of sizes $N = 100$, 200, and 400 and extrapolated to $N \to \infty$ to eliminate finite-N effects. Note that throughout the magnetic-field range of interest, correlations between peaks are positive: small peaks are more likely to be surrounded by small peaks, and large peaks attract more large peaks.

2.3.2 Different large magnetic fields

We now turn to correlations between conductance peaks at *different large* values of the magnetic field. In particular, we are interested in the connected part of the joint distribution $P(g_\mu, g'_\nu)$ where g_μ is a (dimensionless) peak height at magnetic-field strength α, while g_ν is a peak height of a different orbital state at a different magnetic-field strength α'. (Magnetic-field autocorrelations for the same peak were studied by Bruus *et al.* in Ref. [22].) Peaks corresponding to different wave functions are uncorrelated if measured at the same value of the magnetic field, but correlated at different values of the magnetic field. In order to describe these correlations, we still employ the Pandey-Mehta Hamiltonian (2.4) but now take α and α' large. The joint distribution of eigenvectors v_μ and v_ν at different values of

α is thus characterized by the unitary invariants

$$\tilde{\rho}_{\mu\nu} = v_\mu^\dagger(\alpha) v_\nu(\alpha'), \tag{2.16}$$

where $v_\mu(\alpha)$ denotes the eigenvector of the μth level at magnetic-field strength α. At fixed $\tilde{\rho}_{\mu\nu}$, the eigenvector components are distributed according to a multivariate Gaussian distribution with covariance matrix determined by the pair correlator,

$$\langle v^*_{\mu,m}(\alpha) v_{\nu,n}(\alpha')\rangle_{\tilde{\rho}} = \frac{\delta_{mn}\tilde{\rho}_{\mu\nu}}{N}. \tag{2.17}$$

The second moments $\langle|\tilde{\rho}_{\mu\nu}|^2\rangle$ are known in the regimes $|\varepsilon_\mu - \varepsilon_\nu| \gg \min(\Delta, |\alpha'-\alpha|\Delta)$ or $|\alpha' - \alpha| \gg 1$ [23],

$$\langle|\tilde{\rho}_{\mu\nu}|^2\rangle = \frac{2(\alpha'-\alpha)^2}{(\alpha'-\alpha)^4 + 4\pi^2(\varepsilon_\mu - \varepsilon_\nu)^2/\Delta^2}. \tag{2.18}$$

The remainder of the calculation proceeds as before, the only difference being the slightly different expression for the average $\langle|\tilde{\rho}_{\mu\nu}|^2\rangle$ in this case. We thus obtain

$$P_c(g_\mu, g'_\nu) = \frac{2(\alpha'-\alpha)^2(1-g_\mu)(1-g_\nu)}{(\alpha'-\alpha)^4 + 4\pi^2(\varepsilon_\mu - \varepsilon_\nu)^2/\Delta^2} e^{-g_\mu - g'_\nu} \tag{2.19}$$

in the limit $T_L \ll T_R$, whereas

$$P_c(g_\mu, g'_\nu) = \frac{1}{4}\frac{(\alpha'-\alpha)^2 W(g_\mu) W(g'_\nu)}{(\alpha'-\alpha)^4 + 4\pi^2(\varepsilon_\mu - \varepsilon_\nu)^2/\Delta^2} \tag{2.20}$$

for symmetric tunneling contacts, with the function $W(g)$ as defined in Eq. (2.11). For the correlator $C_{\mu\nu} = \langle g_\mu g'_\nu\rangle - \langle g_\mu\rangle\langle g'_\nu\rangle$, this implies

$$C_{\mu\nu} = \frac{2(\alpha'-\alpha)^2}{(\alpha'-\alpha)^4 + 4\pi^2(\varepsilon_\mu - \varepsilon_\nu)^2/\Delta^2} \qquad \text{if } T_L \ll T_R, \tag{2.21a}$$

$$C_{\mu\nu} = \frac{4(\alpha'-\alpha)^2}{9(\alpha'-\alpha)^4 + 36\pi^2(\varepsilon_\mu - \varepsilon_\nu)^2/\Delta^2} \qquad \text{if } T_L = T_R. \tag{2.21b}$$

For $|\alpha' - \alpha| \gg 1$ this result is also valid for the case $\mu = \nu$ and agrees with previous work by Bruus *et al.* in Ref. [22]. In Fig. 2.3, we compare $C_{\mu\nu}$ to numerical

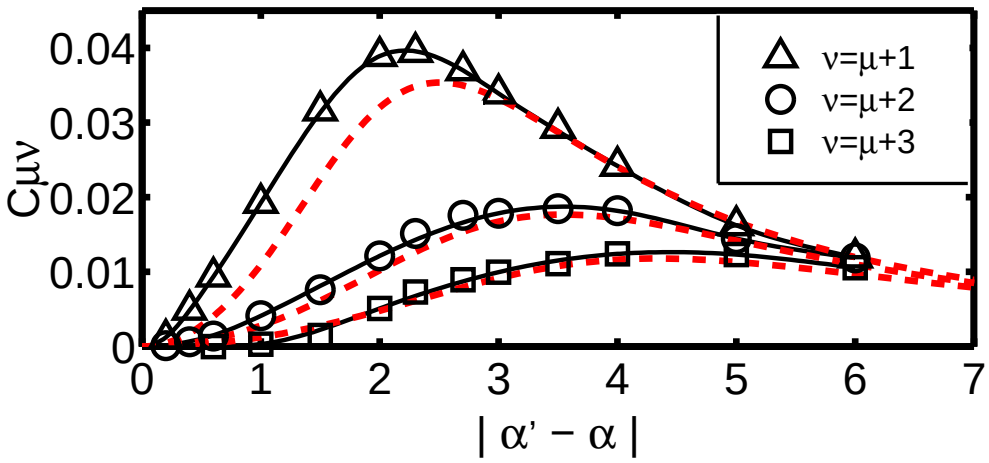

Figure 2.3: Conductance correlations in the GUE-GUE crossover.

The correlator $C_{\mu\nu}$ for different conductance peak heights at different values of the magnetic field, for energy levels μ and $\nu = \mu + 1$, $\mu + 2$, $\mu + 3$ and symmetric tunneling contacts, $T_L = T_R$. The data points are the result of numerical diagonalizations of the Pandey-Mehta Hamiltonian (2.4). The solid curves are drawn as a guide to the eye. The dashed curves show Eq. (2.21b) with $\varepsilon_\mu - \varepsilon_\nu = (\mu - \nu)\Delta$, which is asymptotically correct for large $|\alpha' - \alpha|$ or large $|\mu - \nu|$.

diagonalizations of the Pandey-Mehta Hamiltonian (2.4), using random matrices of sizes $N = 100$, 150, and 300 with extrapolation to $N \to \infty$ to eliminate finite-N effects.

2.4 Application to Spin-Orbit Scattering and Spectral Scrambling

Although our calculations were performed for peak-height correlations that resulted from an external magnetic field or a change in the external magnetic field, they can also be of relevance as an effective description of correlations due to spin-orbit scattering in GaAs quantum dots or due to "spectral scrambling".

In two-dimensional GaAs quantum dots, spin-orbit scattering is described by the following two-dimensional effective Hamiltonian [24],

$$H_{\rm SO} = \frac{1}{2m}\left[\frac{p_2\sigma_1}{\lambda_2} - \frac{p_1\sigma_2}{\lambda_1}\right].$$

Here, σ_i are Pauli-matrices, and λ_1, λ_2 are length scales associated with spin-orbit coupling along the directions $\hat{\mathbf{x}}_1$ and $\hat{\mathbf{x}}_2$ that span the plane in which the dot is formed. In the limit where λ_1, λ_2 are large compared to the linear dot size L, the spin-orbit contribution can be mapped onto an effective magnetic field $\mathbf{B}_{\rm SO}$ by means of a suitable unitary transformation of $H_{\rm SO}$ [24],

$$\tilde{H}_{\rm SO} = \frac{1}{2m}\left(\mathbf{p} - \mathbf{a}_\perp\right)^2 - \frac{\mathbf{p}^2}{2m}, \tag{2.22}$$

where

$$\mathbf{a}_\perp = \frac{\sigma_3}{4\lambda_1\lambda_2}[\hat{\mathbf{x}}_3 \times \mathbf{r}]. \tag{2.23}$$

is the vector potential that generates the leading spin-orbit effect. Hence, weak spin-orbit scattering takes the form of an effective magnetic field $B_{\rm SO} = \hbar c/2e\lambda_1\lambda_2$ of opposite sign for the two spin directions and perpendicular to the plane of the two-dimensional electron gas in which the dot is formed. The parameter α in the Pandey-Mehta Hamiltonian (2.4) is then given by

$$\alpha = \pm\gamma \frac{V}{4\pi\lambda_1\lambda_2}\sqrt{\frac{E_T}{\Delta}}, \tag{2.24}$$

where the $\pm$ corresponds to the two spin directions, and γ is the same geometric factor as in Sec. 2.2. Experimental estimates suggest $\alpha \lesssim 1$, which implies that the effective magnetic field is weak enough to only partially break time-reversal symmetry [25].

The peak-height correlations for a weak magnetic field calculated in Sec. 2.3.1 thus provide a good description of intrinsic peak-height correlations for a quantum dot with weak spin-orbit scattering in the absence of an external magnetic field. On the other hand, when a large external magnetic field B is applied perpendicular to the dot, electrons move in different effective magnetic fields $B \pm B_{\rm SO}$, depending on the direction of their spin. At zero temperature, conductance peaks correspond to resonant tunneling for one of the two spin directions. Our calculations in Sec. 2.3.2 show that peaks originating from resonances with the same spin direction, i.e., $|\alpha' - \alpha| = 0$, will have uncorrelated heights, whereas peaks originating from resonances with opposite spin will have correlated heights, corresponding to the case of large magnetic fields with magnetic-field strength difference $|\alpha' - \alpha| = \gamma(V/2\pi\lambda_1\lambda_2)\sqrt{E_T/\Delta}$.

"Scrambling" is the effect that each electron added to the quantum dot causes a small change to the self-consistent potential in the dot [26, 27]. Hence, every conductance peak is taken at a slightly different realization of the dot's potential.

While this leads to a *decorrelation* of peak heights corresponding to the same orbital state, scrambling also causes a positive correlation between peak heights corresponding to different orbital states, as we have shown above for the case of a large applied magnetic field. (In the unitary ensemble, a change in potential has the same effect as a change in the applied magnetic field. The situation at zero applied magnetic field would correspond to the orthogonal ensemble of random-matrix theory, for which the calculation proceeds along the same lines and gives similar results.) The effect of adding n electrons to a disordered quantum dot corresponds to a parameter change $|\alpha' - \alpha| \sim n\sqrt{\Delta/E_{\mathrm{T}}}$ [27], where E_{T} is the Thouless energy. Hence, we conclude from our calculations that the resulting correlations between peak heights are of order $n^2\Delta/E_{\mathrm{T}}$. While such correlations may be of numerical importance, its dependence on the ratio E_{T}/Δ is the same as that of the non-universal peak-height correlations in a disordered dot [5]. We therefore see that both types of correlations need to be taken into account for a complete understanding of spectral scrambling effects.

BIBLIOGRAPHY

[1] R. A. Jalabert, A. D. Stone, and Y. Alhassid, Phys. Rev. Lett. **68**, 3468 (1992).

[2] J. A. Folk, S. R. Patel, S. F. Godijn, A. G. Huibers, S. M. Cronenwett, C. M. Marcus, K. Campman, and A. C. Gossard, Phys. Rev. Lett. **76**, 1699 (1996).

[3] A. M. Chang, H. U. Baranger, L. N. Pfeiffer, K. W. West, and T. Y. Chang, Phys. Rev. Lett. **76**, 1695 (1996).

[4] M. V. Berry, Proc. R. Soc. London A **400**, 229 (1985).

[5] A. D. Mirlin, Phys. Rep. **326**, 259 (2000).

[6] Thermal smearing, which causes several consecutive wavefunctions to contribute to a single conductance peak, becomes ineffective for temperatures $kT \ll \Delta$, although temperature effects remain relevant for T as low as $k_B T \sim 0.1\Delta$, see G. Usaj and H. U. Baranger, Phys. Rev. B **67** 121308(R) (2003), and Y. Alhassid and T. Rupp, Phys. Rev. Lett. **91**, 056801 (2003)

[7] E. J. Heller, in *Chaos and Quantum Physics,* edited by M. J. Giannoni, A. Voros, and J. Zinn-Justin (Elsevier, New York, 1991).

[8] E. E. Narimanov, N. R. Cerruti, H. U. Baranger, and S. Tomsovic, Phys. Rev Lett. **83**, 2640 (1999).

[9] Y. M. Blanter and A. D. Mirlin, Phys. Rev. E **55**, 6514 (1997).

[10] S. Adam, P. W. Brouwer, J. P. Sethna, and X. Waintal, Phys. Rev. B **66**, 165310 (2002).

[11] C. W. J. Beenakker, Phys. Rev. B **44**, 1646 (1991).

[12] I. L. Aleiner, P. W. Brouwer, and L. I. Glazman, Phys. Rep. **358**, 309 (2002).

[13] P. W. Brouwer, Y. Oreg, and B. I. Halperin, Phys. Rev. B **60**, 13977 (1999).

[14] H. U. Baranger, D. Ullmo, and L. I. Glazman, Phys. Rev. B **61**, 2425 (2000).

[15] Y. Alhassid, J. N. Hormuzdiar, and N. D. Whelan, Phys. Rev. B **58**, 4866 (1998).

[16] A. Pandey and M. L. Mehta, Commun. Math. Phys. **87**, 449 (1983).

[17] K. Frahm and J.-L. Pichard, J. Physique I **5**, 847 (1995).

[18] C. W. J. Beenakker, Rev. Mod. Phys. **69**, 731 (1997).

[19] M. L. Polianski and P. W. Brouwer, J. Phys. A **36**, 3215 (2003).

[20] V. I. Fal'ko and K. B. Efetov, Phys. Rev. Lett. **77**, 912 (1996).

[21] M. L. Mehta, *Random Matrices*, 2nd ed. (Academic Press, Boston, 1991).

[22] H. Bruus, C. H. Lewenkopf, and E. R. Mucciolo, Phys. Rev. B **53**, 9968 (1996).

[23] M. Wilkinson and P. N. Walker, J. Phys. A: Math. Gen. **28**, 6143 (1995).

[24] I. L. Aleiner and V. I. Fal'ko, Phys. Rev. Lett. **87**, 256801 (2001).

[25] D. M. Zumbuhl, J. B. Miller, C. M. Marcus, K. Campman, and A. C. Gossard, Phys. Rev. Lett. **89**, 276803 (2002).

[26] Y. Alhassid and S. Malhotra, Phys. Rev. B **60**, 16315 (1999).

[27] Y. Alhassid and Y. Gefen, cond-mat/0101461 (2001).

Chapter 3

Rate Equations for Coulomb Blockade with Ferromagnetic Leads

3.1 Introduction

Spin-polarized electron tunneling is essential to spin-based electronics [1] and nanoscale magnetics based on the spin-transfer effect [2, 3]. Whereas tunneling through a single tunnel barrier, either between two ferromagnets or between a ferromagnet and a normal metal, has been studied since the mid 1970s [4], the study of spin-polarized transport through mesoscopic double tunneling junctions is more recent. Double mesoscopic junctions are of interest because of the small capacitance of the central region in between the tunneling junctions, which allows electrons to be transported one by one [5]. Experiments have been reported both for normal-metal leads with a ferromagnetic island between the junctions [6, 7]

and for a normal island with spin-polarized junctions [8, 9, 10]. A large number of theoretical works has dealt with these cases [11, 12, 13, 14, 15, 16, 17, 18, 19, 20, 21, 22, 23, 24, 25, 26, 27, 28, 29, 30].

In this work, we consider the case of a normal-metal island with ferromagnetic leads. If the temperature is much larger than the tunneling rates onto or off the island, electron tunneling is sequential. In that case, quantum mechanical correlations between electrons in different states are lost because of thermal smearing, and a simple description in terms of rate equations applies. Depending on whether the temperature is small or large compared to the level spacing in the island, these rate equations describe the probability to find a certain number of electrons on the island [31, 32, 33] or the occupation of the electronic states in the island [34, 35].

Whereas the rate-equation approach was applied straightforwardly to ferromagnetic leads with collinear polarizations [20, 28], application to leads with non-collinear polarizations requires a formulation in terms of the density matrices of degenerate levels, not the occupations of states [29, 30]. (If spin degeneracy on the normal-metal island is lifted, for instance by a magnetic field, scalar rate equations remain valid despite polarized leads.) There are two reasons for this additional complication: First, with non-collinear polarizations, no common quantization direction exists, and one cannot avoid a formulation of the problem in which electrons tunnel into superpositions of states with different spin projections [16]. Second, coupling to the ferromagnetic leads slightly lifts the spin degeneracy and leads to a slow precession of the spin on the dot [29]. The use of density matrices instead of occupation probabilities in the rate-equation formalism allows for the inclusion of correlations between different quantum states [36, 37]. Since the temperature is much larger than the escape rate to the leads, only correlations between states

with the same energy need to be taken into account.

Density-matrix rate equations were first used to describe transport through a metal particle (or a quantum dot or a single molecule) with spin-polarized tunnel contacts in a recent paper by König and Martinek [29] (see also Ref. [30]). These authors used the Keldysh formalism to derive the density-matrix rate equations for a dot in which only one level contributes to transport. The purpose of the present work is to formulate a density-matrix rate equation for quantum dots in which many electronic levels contribute to transport and to simplify the derivation of Ref. [30]. The extension to many levels is relevant for the analysis of experimental data, since the majority of experiments feature high bias voltages at which more than one electronic level contributes to the current [38].

A remarkable result of our study is that a formulation in terms of density-matrix rate equations is not only needed for spin-polarized leads with non-collinear polarization directions, but that it may also be necessary for unpolarized leads or for spin-polarized leads with collinear polarization directions if the metal island has a large dimensionless conductance g. These relatively large metal particles or quantum dots have degenerate or almost-degenerate many-electron levels. Correlations between the degenerate states persist during the time an electron occupies the quantum dot and need to be accounted for using a description in terms of a density matrix. The origin of the degeneracy is that in large-g metal grains or quantum dots electronic interactions are described by the 'universal interaction Hamiltonian' [39]. With this interaction, many-electron levels with three or more singly occupied single-electron levels are degenerate if their spin is not maximal. For example, there are four degenerate states with three singly occupied levels and total spin $S = 1/2$. A rate equation in terms of scalar occupation probabili-

ties only [40] will fail to describe correlations between these degenerate states. A detailed description of this case will be given in Sec. 3.2.3.

3.2 Matrix Rate-Equation Formalism

We consider a metal particle — or a quantum dot or a single molecule — that is attached to a number of ferromagnetic leads via tunneling contacts with a conductance much smaller than the conductance quantum e^2/h. A schematic drawing of a metal particle with two leads is shown in Fig. 3.1. In our formulation of the problem, we assume that all leads are fully polarized; a partially polarized lead is simply represented by two fully polarized leads with different densities of states and different tunneling rates. We assume that the temperature T is much larger than the tunneling rates to and from the leads. This is the regime for which rate equations have been shown to be a valid description of metal particles without spin-polarized leads.

3.2.1 Single doubly degenerate level

In order to make the connection to previous works [16, 29, 30], we first develop the formalism for the case of nonlinear transport through a single level. Our approach is closely connected to the works by Nazarov [36] and Gurvitz [37], who used rate equations to describe high-bias transport through a sequence of tunnel barriers. For a metal particle in which only one level is relevant for transport, we need to consider occupation of the level by zero, one, or two electrons, at energies ε_0, ε_1, and ε_2, respectively. The precise value of these energies depends on the charging energy and exchange interaction of the metal particle, the voltages on

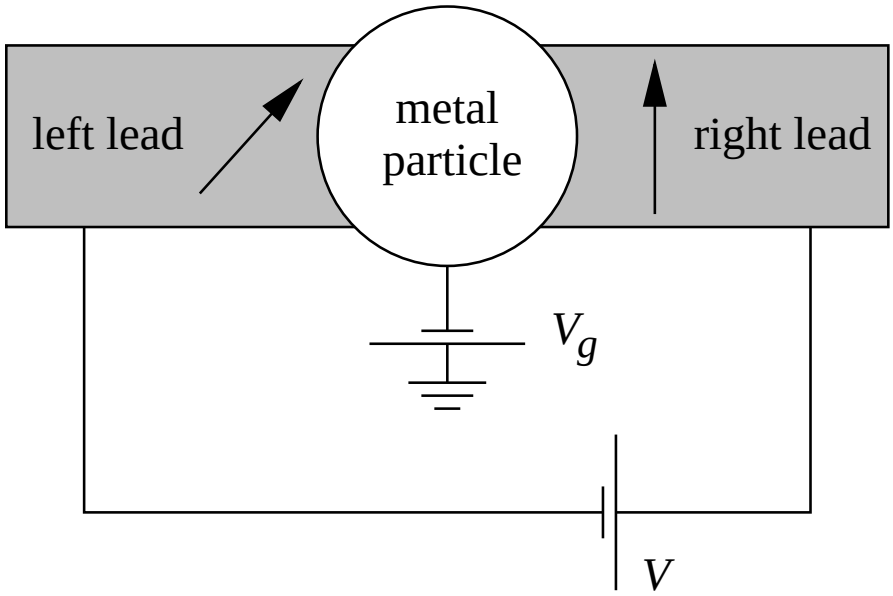

Figure 3.1: Metal particle attached to two ferromagnetic leads.

The metal particle is attached to two ferromagnetic leads with polarization directions that do not necessarily have to be collinear. In addition to a bias voltage V, the metal particle is coupled capacitively to a gate voltage V_g.

nearby gates, etc. For occupation by zero or two electrons, the many-electron level is non-degenerate, and we can use scalars p_0 and p_2 to describe the probability to find the particle in a state with zero or two electrons, respectively. If the level is occupied by one electron only, one needs to use a 2×2 density matrix ρ_1 to fully describe the state of the particle. Conservation of probability implies

$$p_0 + \mathrm{tr}\, \rho_1 + p_2 = 1. \tag{3.1}$$

Without tunneling to and from the reservoirs, p_0, ρ_1, and p_2 are time independent. The time dependence of p_0, ρ_1, and p_2 then arises from tunneling of electrons onto or off the metal particle: real tunneling processes shift the number of electrons on the metal particle, whereas virtual tunneling processes cause a precession of the spin if the level is singly occupied. The net tunneling rate to and from lead α depends on the direction of the polarization in that lead, which we describe by means of the spinors m_α ($\bar{m}_\alpha$) pointing parallel (anti-parallel) to the polarization direction of lead α, the tunneling rate Γ_α for electrons with spin m_α, and the distribution function f_α in lead α. In order to describe both the virtual and real tunneling processes, we combine the rate Γ_α and the spinors m_α and $\bar{m}_\alpha$ into the spinor tunneling amplitudes

$$\gamma_\alpha = \Gamma_\alpha^{1/2} m_\alpha, \quad \bar{\gamma}_\alpha = \Gamma_\alpha^{1/2} \bar{m}_\alpha, \tag{3.2}$$

with $\gamma_\alpha^\dagger \gamma_\alpha = \bar{\gamma}_\alpha^\dagger \bar{\gamma}_\alpha = \Gamma_\alpha$ and $\gamma_\alpha^\dagger \bar{\gamma}_\alpha = 0$.

Virtual tunneling processes can be described by the effective Hamiltonian [41]

$$H_1 = \frac{\hbar}{4\pi} \mathrm{P} \int d\xi \sum_\alpha (1 - 2 f_\alpha(\xi)) \left[\frac{\gamma_\alpha \gamma_\alpha^\dagger}{\varepsilon_1 - \varepsilon_0 - \xi} + \frac{\bar{\gamma}_\alpha \bar{\gamma}_\alpha^\dagger}{\varepsilon_2 - \varepsilon_1 - \xi} \right],$$

where P denotes the Cauchy principal value. Note that if $\varepsilon_2 - \varepsilon_1 = \varepsilon_1 - \varepsilon_0$, one has H_1 proportional to the unit matrix in spin space and thus $[H_1, \rho_1] = 0$: virtual

excitations do not cause a spin precession without interactions [29]. The time evolution of the scalars p_0 and p_2 and the 2×2 matrix ρ_1 is described by the equations [29, 30]

$$\frac{\mathrm{d}p_0}{\mathrm{d}t} = \sum_\alpha (1 - f_\alpha(\varepsilon_1 - \varepsilon_0))\gamma_\alpha^\dagger \rho_1 \gamma_\alpha - \sum_\alpha f_\alpha(\varepsilon_1 - \varepsilon_0)\gamma_\alpha^\dagger p_0 \gamma_\alpha, \tag{3.3}$$

$$\frac{\mathrm{d}p_2}{\mathrm{d}t} = \sum_\alpha f_\alpha(\varepsilon_2 - \varepsilon_1)\bar{\gamma}_\alpha^\dagger \rho_1 \bar{\gamma}_\alpha - \sum_\alpha (1 - f_\alpha(\varepsilon_2 - \varepsilon_1))\bar{\gamma}_\alpha^\dagger p_2 \bar{\gamma}_\alpha, \tag{3.4}$$

$$\begin{aligned}\frac{\mathrm{d}\rho_1}{\mathrm{d}t} = {} & \frac{i}{\hbar}(\rho_1 H_1 - H_1 \rho_1) \\ & + \sum_\alpha f_\alpha(\varepsilon_1 - \varepsilon_0)\gamma_\alpha p_0 \gamma_\alpha^\dagger - \frac{1}{2}\sum_\alpha (1 - f_\alpha(\varepsilon_1 - \varepsilon_0)) \left[\gamma_\alpha \gamma_\alpha^\dagger \rho_1 + \rho_1 \gamma_\alpha \gamma_\alpha^\dagger\right] \\ & + \sum_\alpha (1 - f_\alpha(\varepsilon_2 - \varepsilon_1))\bar{\gamma}_\alpha p_2 \bar{\gamma}_\alpha^\dagger - \frac{1}{2}\sum_\alpha f_\alpha(\varepsilon_2 - \varepsilon_1) \left[\bar{\gamma}_\alpha \bar{\gamma}_\alpha^\dagger \rho_1 + \rho_1 \bar{\gamma}_\alpha \bar{\gamma}_\alpha^\dagger\right],\end{aligned} \tag{3.5}$$

whereas the current through each of the tunnel contacts is calculated as [34, 35]

$$\begin{aligned}I_\alpha = {} & f_\alpha(\varepsilon_1 - \varepsilon_0)\gamma_\alpha^\dagger p_0 \gamma_\alpha - (1 - f_\alpha(\varepsilon_1 - \varepsilon_0))\gamma_\alpha^\dagger \rho_1 \gamma_\alpha \\ & + f_\alpha(\varepsilon_2 - \varepsilon_1)\bar{\gamma}_\alpha^\dagger \rho_1 \bar{\gamma}_\alpha - (1 - f_\alpha(\varepsilon_2 - \varepsilon_1))\bar{\gamma}_\alpha^\dagger p_2 \bar{\gamma}_\alpha.\end{aligned} \tag{3.6}$$

For $f_\alpha = 0$ or $f_\alpha = 1$, Eqs. (3.3)–(3.6) follow from considering the escape of electrons or holes from the metal particle into vacuum [36, 37, 42]. The factors f_α and $(1 - f_\alpha)$, which also appear in the scalar rate equations [34, 35], are inserted to reflect the modification of tunneling rates by the electron distribution in the leads. This simple way of accounting for the presence of electrons in the leads is no longer valid when correlations between the electrons in the leads and in the metal particle are formed, such as is the case in the Kondo effect [22, 23, 24, 25, 26, 43, 44]. We remark that, since Eqs. (3.3)–(3.6) are meant to describe transport at the lowest order in Γ_α only, the energy shift implied by the Hamiltonian H_1 need not be included in the argument of the distribution function f_α. For that reason,

Eqs. (3.3)–(3.6) describe both the case of low bias and high bias, in contrast to the formalism of Refs. [37, 42], which is appropriate for high bias only. Also note that Eqs. (3.3)–(3.5) are consistent with probability conservation, Eq. (3.1), and that they reduce to the standard rate equations [34, 35] once the polarizations in the leads are collinear.

3.2.2 General formalism

For the general description, we consider a normal-metal particle with many-electron levels ε_k, each of which has degeneracy j_k. The many-electron states are labeled $|k,m\rangle$, where $m = 1,\ldots,j_k$. The number of electrons in state $|k,m\rangle$ is denoted by N_k. Real and virtual transitions between many-electron states are possible because of tunneling of electrons between the metal particle and the source and drain reservoirs. As before, we assume that this tunneling rate is small in comparison to the spacing between electronic levels and temperature. In that case, we may describe the state of the dot by a set of density matrices ρ_k for each many-electron level, and we can neglect correlations between states with different energy.

The tunneling Hamiltonian describing the coupling of the metal particle to lead α is determined by the $j_k \times j_{k'}$ matrix $v^{\pm}_{\alpha;k,k'}$ containing the matrix elements between the many-electron multiplets $|k,\cdot\rangle$ and $|k',\cdot\rangle$ with $N_k = N_{k'} \pm 1$. In order to make contact with the rate equations derived above, we define the $j_k \times j_{k'}$ matrix of transition amplitudes $\gamma^{\pm}_{\alpha;k,k'} = (2\pi\nu_\alpha/\hbar)^{1/2} v^{\pm}_{\alpha;k,k'}$, where ν_α is the density of states of lead α. We define $\gamma^{\pm}_{\alpha;k,k'} = 0$ if $N_k \neq N_{k'} \pm 1$. One may write $\gamma^{\pm}_{\alpha;k,k'} = (\Gamma_\alpha)^{1/2} w^{\pm}_{\alpha;k,k'}$, where $w^{\pm}_{\alpha;k,k'}$ is dimensionless and Γ_α is the tunneling rate through contact α if the metal island is replaced by an electron reservoir. For point contacts, the magnitude of $w^{\pm}_{\alpha;k,k'}$ is set by the value of a wave function

at the location of the contact [45]. If the degeneracy of the multiplets $|k,\cdot\rangle$ and $|k',\cdot\rangle$ arises from angular momentum, the matrix structure of $w^{\pm}_{\alpha;k,k'}$ is set by the Clebsch-Gordon coefficients. With this notation, virtual excitations lead to the effective Hamiltonian H_k for the multiplet $|k,\cdot\rangle$,

$$H_k = \frac{\hbar}{4\pi}\mathrm{P}\int d\xi \sum_{\alpha,k'}(1-2f_\alpha(\xi))\left[\frac{\gamma^+_{\alpha;k,k'}\gamma^-_{\alpha;k',k}}{\varepsilon_k-\varepsilon_{k'}-\xi}+\frac{\gamma^-_{\alpha;k,k'}\gamma^+_{\alpha;k',k}}{\varepsilon_{k'}-\varepsilon_k-\xi}\right]. \tag{3.7}$$

Then the appropriate generalization of the rate equations (3.3)–(3.5) and the current formula (3.6) is

$$\begin{aligned}\frac{\partial\rho_k}{\partial t} = {}& \frac{i}{\hbar}(\rho_k H_k - H_k\rho_k)\\ &+\sum_{\alpha,k'}\left[f_\alpha(\varepsilon_k-\varepsilon_{k'})\gamma^+_{\alpha;k,k'}\rho_{k'}\gamma^-_{\alpha;k',k}+(1-f_\alpha(\varepsilon_{k'}-\varepsilon_k))\gamma^-_{\alpha;k,k'}\rho_{k'}\gamma^+_{\alpha;k',k}\right]\\ &-\frac{1}{2}\sum_{\alpha,k}\left[f_\alpha(\varepsilon_{k'}-\varepsilon_k)(\gamma^-_{\alpha;k,k'}\gamma^+_{\alpha;k',k}\rho_k+\rho_k\gamma^-_{\alpha;k,k'}\gamma^+_{\alpha;k',k})\right.\\ &\qquad\left.+(1-f_\alpha(\varepsilon_k-\varepsilon_{k'}))(\gamma^+_{\alpha;k,k'}\gamma^-_{\alpha;k',k}\rho_k+\rho_k\gamma^+_{\alpha;k,k'}\gamma^-_{\alpha;k',k})\right],\end{aligned} \tag{3.8}$$

$$I_\alpha = e\sum_{k,k'}\left[f_\alpha(\varepsilon_k-\varepsilon_{k'})\gamma^+_{\alpha;k,k'}\rho_{k'}\gamma^-_{\alpha;k',k}-(1-f_\alpha(\varepsilon_{k'}-\varepsilon_k))\gamma^-_{\alpha;k,k'}\rho_{k'}\gamma^+_{\alpha;k',k}\right]. \tag{3.9}$$

Here the summation over k' extends over all many-electron states different from k. One easily verifies that Eq. (3.8) conserves the total probability $\sum_k \mathrm{tr}\,\rho_k = 1$.

3.2.3 Unpolarized leads

The density-matrix rate equations (3.8) do *not* necessarily reduce to the standard scalar rate equations of Refs. [34, 35] when all leads are unpolarized or when the leads have collinear spin polarizations. The reason for this, at first, surprising fact is that overlaps between different many-body states are not accurately described by scalar transition probabilities if there are degeneracies. With degeneracies,

non-orthogonal coherent superpositions of many-electron states are involved in the transport process.

Although level repulsion rules out degeneracies in the single-particle states in a generic metal grain or quantum dot, for large metal grains or quantum dots, (near) degeneracies may occur in the many-electron spectrum. The origin of the degeneracy is that electron-electron interactions in metal particles or quantum dots with large dimensionless conductance g are described by the 'universal interaction Hamiltonian' [39],

$$H_{\rm ee} = E_{\rm C} N^2 + J S^2, \tag{3.10}$$

where N is the total number of electrons on the metal particle, $E_{\rm C}$ is the charging energy, S is the total spin, and J is the exchange interaction strength. According to Eq. (3.10), the energy of a many-electron state depends on the occupation of the single-electron states and the total spin S only. This gives rise to degeneracies in many-electron states with three or more singly occupied single-electron levels. For example, in a metal grain with single-electron levels labeled 1, 2, and 3, the two states

$$|+\rangle \equiv \frac{1}{\sqrt{3}} \left(e^{\frac{2\pi i}{3}} c^\dagger_{\uparrow 1} c^\dagger_{\downarrow 2} c^\dagger_{\downarrow 3} |0\rangle + e^{\frac{-2\pi i}{3}} c^\dagger_{\downarrow 1} c^\dagger_{\uparrow 2} c^\dagger_{\downarrow 3} |0\rangle + c^\dagger_{\downarrow 1} c^\dagger_{\downarrow 2} c^\dagger_{\uparrow 3} |0\rangle \right), \tag{3.11a}$$

$$|-\rangle \equiv \frac{1}{\sqrt{3}} \left(e^{\frac{-2\pi i}{3}} c^\dagger_{\uparrow 1} c^\dagger_{\downarrow 2} c^\dagger_{\downarrow 3} |0\rangle + e^{\frac{2\pi i}{3}} c^\dagger_{\downarrow 1} c^\dagger_{\uparrow 2} c^\dagger_{\downarrow 3} |0\rangle + c^\dagger_{\downarrow 1} c^\dagger_{\downarrow 2} c^\dagger_{\uparrow 3} |0\rangle \right), \tag{3.11b}$$

both have three singly occupied single-electron levels with total spin $S = 1/2$ and $S_z = -1/2$. Hence, according to the 'universal interaction Hamiltonian', they are degenerate. Since both states have the same value of S_z, the degeneracy is not broken by a magnetic field. However, in principle it may be lifted by non-universal residual interactions that are not included in the 'universal interaction Hamiltonian' [39], but such residual interactions are weak if $g \gg 1$, and they can be

neglected if the level splitting that they cause is smaller than the level broadening due to escape through the tunnel contacts. The degeneracy may also be lifted in metal particles with spin-orbit scattering if the spin-orbit rate $\hbar/\tau_{\mathrm{so}}$ is comparable to the mean spacing Δ between single-electron levels [46, 47].

We now illustrate how this degeneracy necessitates the use of a matrix rate equation using the example of a metal particle with three spin-degenerate single-electron levels. For the ease of argument, a magnetic field is applied along the negative z axis. We consider transitions from the three two-electron states with $S = 1$, $S_z = -1$,

$$|1\rangle \equiv c^\dagger_{\downarrow 2} c^\dagger_{\downarrow 3} |0\rangle \,, \tag{3.12a}$$

$$|2\rangle \equiv c^\dagger_{\downarrow 1} c^\dagger_{\downarrow 3} |0\rangle \,, \tag{3.12b}$$

$$|3\rangle \equiv c^\dagger_{\downarrow 1} c^\dagger_{\downarrow 2} |0\rangle \,, \tag{3.12c}$$

to the degenerate three-electron states (3.11). As the states (3.12) are non-degenerate, they are described by means of the probability p_j of finding the system in state $|j\rangle$, $j = 1, 2, 3$. On the other hand, the states (3.11) are degenerate and we need to describe their occupation by a 2×2 density matrix ρ,

$$\rho = \begin{pmatrix} \rho_{++} & \rho_{+-} \\ \rho_{-+} & \rho_{--} \end{pmatrix} . \tag{3.13}$$

Transitions from the states (3.12) to the doublet (3.11) occur at rates Γ_j, $j = 1, 2, 3$. Writing down the time evolution of ρ that results from those transitions, we find

$$\frac{\mathrm{d}\rho}{\mathrm{d}t} = \frac{\Gamma_1}{3} p_1 \begin{pmatrix} 1 & e^{\frac{2\pi i}{3}} \\ e^{\frac{-2\pi i}{3}} & 1 \end{pmatrix} + \frac{\Gamma_2}{3} p_2 \begin{pmatrix} 1 & e^{\frac{-2\pi i}{3}} \\ e^{\frac{2\pi i}{3}} & 1 \end{pmatrix} + \frac{\Gamma_3}{3} p_3 \begin{pmatrix} 1 & 1 \\ 1 & 1 \end{pmatrix} + \ldots , \tag{3.14}$$

where the remaining terms describe processes that do not depend on the p_j, $j = 1, 2, 3$. Clearly, there is no basis that would diagonalize all three matrices in Eq. (3.14) simultaneously for arbitrary choice of the p_j. This proves that it is imperative to use the full matrix structure for ρ in order to properly deal with correlations between the states (3.11).

3.3 Application to Spin-Polarized Transport

We now apply the formalism of the previous section to transport through metal particles with ferromagnetic contacts. We first consider the simpler case of a metal particle in which only one energy level participates in transport and then turn our attention to the case of multiple levels.

3.3.1 Single doubly occupied level

The linear-response conductance G of a metal particle coupled to two fully polarized ferromagnetic leads, labeled L and R, respectively, is easily calculated from Eqs. (3.3)–(3.6),

$$G = G_0 \cos^2(\theta/2) \left[1 - \frac{4a^2 \Gamma_L \Gamma_R \sin^2(\theta/2)}{[a^2 + (1 - f(\varepsilon_1 - \varepsilon_0) + f(\varepsilon_2 - \varepsilon_1))^2](\Gamma_L + \Gamma_R)^2} \right]^{-1}, \tag{3.15}$$

where θ is the angle between the polarizations of the ferromagnets, G_0 is the linear conductance for $\theta \to 0$,

$$G_0 = \frac{e^2}{\hbar T} \frac{\Gamma_L \Gamma_R (1 - f(\varepsilon_2 - \varepsilon_1)) f(\varepsilon_1 - \varepsilon_0)(1 - f(\varepsilon_1 - \varepsilon_0) + f(\varepsilon_2 - \varepsilon_1))}{(\Gamma_L + \Gamma_R)(1 + f(\varepsilon_1 - \varepsilon_0) - f(\varepsilon_2 - \varepsilon_1))}, \tag{3.16}$$

and

$$a = \mathrm{P} \int \frac{d\xi}{2\pi} \frac{(1 - 2f(\xi))(\varepsilon_2 + \varepsilon_0 - 2\varepsilon_1)}{(\varepsilon_1 - \varepsilon_0 - \xi)(\varepsilon_2 - \varepsilon_1 - \xi)}. \tag{3.17}$$

For partially polarized leads with polarization $P_\alpha \equiv (\Gamma_\alpha - \bar{\Gamma}_\alpha)/(\Gamma_\alpha + \bar{\Gamma}_\alpha)$, where $\bar{\Gamma}_\alpha$ is the tunneling rate for electrons with spin $\bar{m}_\alpha$, one finds

$$G = \frac{2G_0}{D}\left[\Gamma_L(1-P_L) + \Gamma_R(1-P_R) + \frac{P_L^2 P_R^2 \Gamma_L \Gamma_R \sin^2\theta}{\Gamma_L(1+P_R) + \Gamma_R(1+P_L) - DE}\right], \tag{3.18}$$

where G_0 is given by Eq. (3.16) above, and we abbreviated

$$D = \Gamma_R(1+P_L)(1-P_R) + \Gamma_L(1-P_L)(1+P_R) + 4\Gamma_L\Gamma_R P_L P_R \sin^2(\theta/2)/(\Gamma_L+\Gamma_R), \tag{3.19}$$

$$E = a^2(1+P_L)(1+P_R)(\Gamma_L+\Gamma_R)\left[a^2 + (1 - f(\varepsilon_1-\varepsilon_0) + f(\varepsilon_2-\varepsilon_1))^2\right]^{-1} \times \left[\Gamma_L(1+P_R) + \Gamma_R(1+P_L)\right]^{-1}. \tag{3.20}$$

For symmetric contacts, $\Gamma_L = \Gamma_R$ and $P_L = P_R$, Eqs. (3.15) and (3.18) were previously obtained in Refs. [29, 30]. Without the spin-precession term (the first term on the right-hand side of Eq. (3.5)), we recover the linear conductance calculated by Usaj and Baranger [16], after correction of a technical mistake in Ref. [16].

As pointed out by König and Martinek, the role of the spin-precession term is to reduce the angular dependence of the conductance. Our general results (3.15) and (3.18) show how this reduction depends on the symmetry of the contacts: the reduction is strongest for symmetric contacts ($\Gamma_R = \Gamma_L$), whereas it vanishes in the generic case of very asymmetric contacts ($\Gamma_R \ll \Gamma_L$). In the latter case, the spin precession axis is aligned with m_L; precession around m_L does not change the angular dependence of the conductance.

3.3.2 Case of up to three electrons on the dot

For a metal particle in which more than one level contributes to transport we calculate the differential conductance $G = \partial I/\partial V$ numerically as a function of the

bias voltage V.

The numerical calculation is done for a metal particle in which five single-electron levels, with a total of two or three electrons, contribute to the current. The lead polarizations are chosen parallel or anti-parallel, with polarizations $P_L = P_R \equiv P$. With a maximum of three singly occupied levels, the largest possible spin on the dot is 3/2. The positions of the single-electron energy levels are taken from the center of a matrix drawn from the Gaussian Orthogonal Ensemble of random-matrix theory, and the temperature T is set at one percent of the mean spacing Δ between single-electron levels, to ensure that all features in the current-voltage characteristic can be resolved in the numerical calculations. Electron-electron interactions are described using Eq. (3.10). In the numerical calculations, we set $E_{\rm C} = 25\Delta$, and $J = -0.32\Delta$. (Values of the exchange constant J are tabulated in Ref. [47] for most normal metals.) The tunneling rates Γ_L and Γ_R are chosen $\lesssim 0.1 k_B T$ and equal for all levels, as is appropriate for metal particles with wide tunnel barriers. The source-drain voltage V is applied to the right lead and is assumed to change the effective chemical potential in the right lead only.

The use of leads with collinear polarizations in the numerical calculations eliminates most of the necessity of using density-matrix rate equations, except for the degenerate $S = 1/2$ states with three singly occupied levels. These states are fourfold degenerate. We denote them

$$|\frac{1}{2}, +\rangle \equiv \frac{1}{\sqrt{3}}(e^{\frac{2\pi i}{3}} |\uparrow\uparrow\downarrow\rangle + e^{\frac{-2\pi i}{3}} |\uparrow\downarrow\uparrow\rangle + |\downarrow\uparrow\uparrow\rangle), \tag{3.21a}$$

$$|\frac{1}{2}, -\rangle \equiv \frac{1}{\sqrt{3}}(e^{\frac{-2\pi i}{3}} |\uparrow\uparrow\downarrow\rangle + e^{\frac{2\pi i}{3}} |\uparrow\downarrow\uparrow\rangle + |\downarrow\uparrow\uparrow\rangle), \tag{3.21b}$$

$$|-\frac{1}{2},+\rangle \equiv \frac{1}{\sqrt{3}}(e^{\frac{2\pi i}{3}}\,|\uparrow\downarrow\downarrow\rangle + e^{\frac{-2\pi i}{3}}\,|\downarrow\uparrow\downarrow\rangle + |\downarrow\downarrow\uparrow\rangle), \tag{3.22a}$$

$$|-\frac{1}{2},-\rangle \equiv \frac{1}{\sqrt{3}}(e^{\frac{-2\pi i}{3}}\,|\uparrow\downarrow\downarrow\rangle + e^{\frac{2\pi i}{3}}\,|\downarrow\uparrow\downarrow\rangle + |\downarrow\downarrow\uparrow\rangle). \tag{3.22b}$$

However, only the twofold degeneracy inside the pairs with S_z=1/2 and S_z=$-1/2$ is relevant, and it is sufficient to describe the occupation of the four $S = 1/2$ states with two 2×2 density matrices $\rho(S_z$=1/2) and $\rho(S_z$=$-1/2)$ as in Eq. (3.13).

To illustrate the use of the matrix rate equations in this case, we write down the full transition vectors for the transition between the $S = 1$ triplet states and the two doublets (3.21) and (3.22). We denote the $S = 1$ triplet state by $|S_z\rangle$, with $S_z = -1, 0, 1$. In relation to the two energy levels already occupied in the triplet state, we consider adding an electron in a single-electron level with higher, lower, or intermediate energy and denote the different vectors by superscripts h, l, and m, respectively. Choosing the orientation of the leads as the spin quantization axis, the nonzero transition vectors for addition of an electron with spin up from lead α as they appear in the rate equation (3.8) are $\gamma_\alpha^{+,h} = (\Gamma_\alpha^h)^{1/2} w^{+,h}$, $\gamma_\alpha^{+,l} = (\Gamma_\alpha^l)^{1/2} w^{+,l}$, and $\gamma_\alpha^{+,m} = (\Gamma_\alpha^m)^{1/2} w^{+,m}$, with

$$w^{+,h}_{|\frac{1}{2}\rangle,|0\rangle} = \frac{-1}{\sqrt{6}} \begin{pmatrix} e^{-2\pi i/3} \\ \\ e^{2\pi i/3} \end{pmatrix}, \tag{3.23a}$$

$$w^{+,h}_{|-\frac{1}{2}\rangle,|-1\rangle} = \frac{1}{\sqrt{3}} \begin{pmatrix} 1 \\ \\ 1 \end{pmatrix}, \tag{3.23b}$$

$$w^{+,l}_{|\frac{1}{2}\rangle,|0\rangle} = \frac{-1}{\sqrt{6}} \begin{pmatrix} 1 \\ \\ 1 \end{pmatrix}, \tag{3.23c}$$

$$w^{+,l}_{|-\frac{1}{2}\rangle,|-1\rangle} = \frac{1}{\sqrt{3}} \begin{pmatrix} e^{-2\pi i/3} \\ \\ e^{2\pi i/3} \end{pmatrix}, \tag{3.23d}$$

$$w^{+,m}_{|\frac{1}{2}\rangle,|0\rangle} = \frac{1}{\sqrt{6}} \begin{pmatrix} e^{2\pi i/3} \\ e^{-2\pi i/3} \end{pmatrix}, \tag{3.23e}$$

$$w^{+,m}_{|-\frac{1}{2}\rangle,|-1\rangle} = \frac{1}{\sqrt{3}} \begin{pmatrix} e^{2\pi i/3} \\ e^{-2\pi i/3} \end{pmatrix}. \tag{3.23f}$$

The transition vectors for adding a spin-down electron follow straightforwardly from the above, and the amplitudes for removing electrons are obtained from the above by hermitian conjugation. Although these were not considered in the numerical calculations, we mention that the overlap matrices for non-collinear lead polarizations can be obtained from Eqs. (3.23) by combining the transition vectors into 4×3 matrix amplitudes for the full transition from the spin-1 triplet to the three-electron spin-$\frac{1}{2}$ quadruplet, followed by multiplication with appropriate representations of rotation matrices. In this particular case, the transition matrix amplitude would have to be multiplied with a four-dimensional representation from the left and a three-dimensional representation from the right. The relevant rotation matrices are listed in Appendix A.

We now turn to the results of our numerical calculations. One expects that anti-parallel lead polarizations cause spin accumulation on the metal island. This can indeed be observed in our solution of the rate equations, as shown in Fig. 3.2, where we plot the probability of finding spin $S = 3/2$ (as opposed to $S = 1/2$) on the metal particle for different lead polarizations P. For anti-parallel lead polarizations, the probability to find $S = 3/2$ increases with increasing polarization, whereas it is virtually independent of polarization for parallel lead polarizations.

In Figs. 3.3 and 3.4 we address the dependence of peaks of the differential conductance on the lead polarization P. The former figure displays both parallel lead polarizations (positive P in the figure) and anti-parallel lead polarizations (nega-

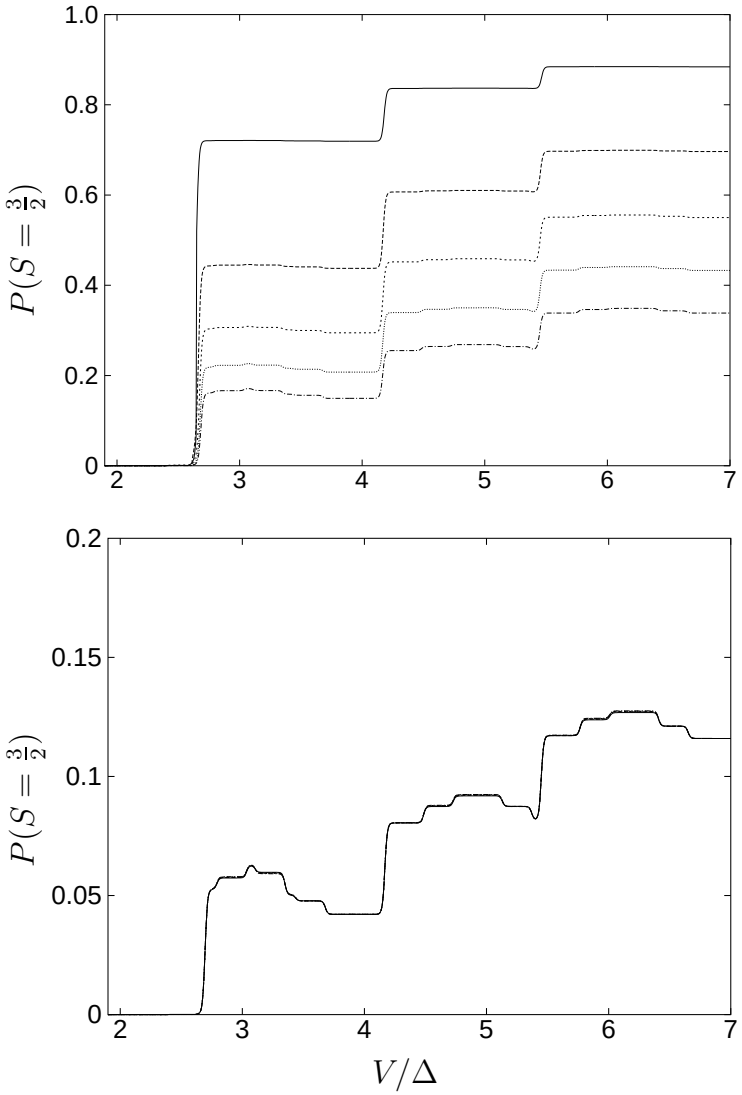

Figure 3.2: Spin on the dot as a function of source-drain voltage.

Probability of finding total spin 3/2 on the dot as a function of the source-drain voltage V (in units of the mean level spacing Δ) for anti-parallel (top panel) and parallel lead polarizations (bottom panel) featuring polarizations $P{=}P_L{=}P_R{=}0.95$, 0.85, 0.75, 0.65, 0.55 (top to bottom), with $\Gamma_R/\Gamma_L = 0.2$.

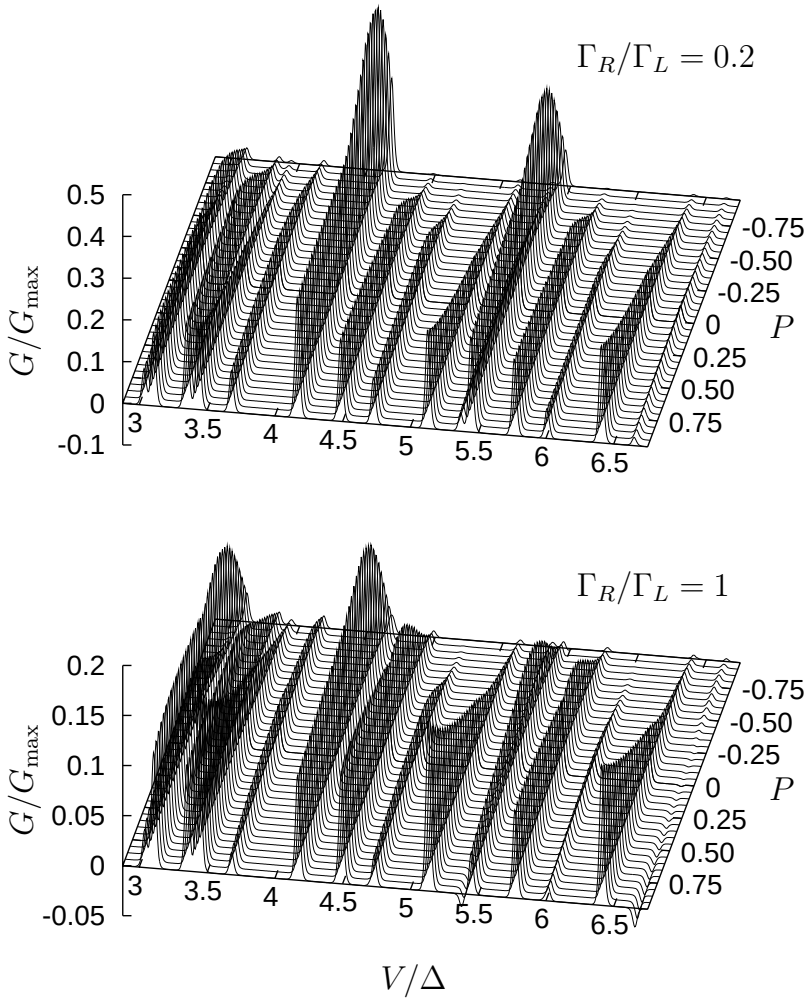

Figure 3.3: Excerpt from the conductance peak spectrum.

We show several conductance peaks for anti-parallel and parallel lead orientations as a function of the source-drain voltage V (in units of the mean level spacing Δ) and of lead polarization $P = P_L = P_R$. For ease of presentation, the case of anti-parallel polarization is plotted against *negative* polarization. The excerpt shown here does not include the dominant low-energy peak.

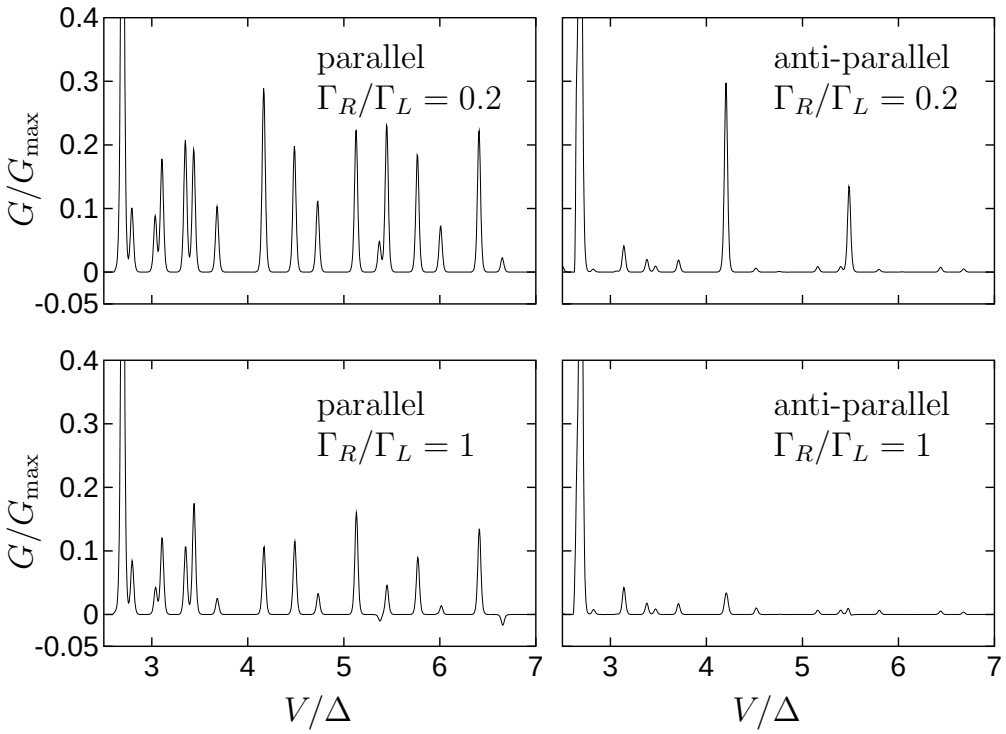

Figure 3.4: Normalized conductance peaks for different polarization orientations.

We show the normalized differential conductance as a function of the source-drain voltage V (in units of the mean level spacing Δ) for parallel (left panels) and anti-parallel (right panels) lead polarizations $P{=}P_L{=}P_R{=}0.9$. The vertical scale has been normalized to the magnitude $G_{\max}$ of the largest (first) conductance peak.

tive P in the figure). Some peaks evolve non-monotonously, whereas others rise or fall monotonously in magnitude. Of particular interest are those conductance peaks that evolve from positive to negative values. Negative conductance peaks at voltage V arise if, upon reaching that voltage, a many-body state that is poorly connected to other states is made accessible. (This type of behavior is not limited to ferromagnetic leads.) Not only does there seem to be a tendency toward negative differential conductance upon going from anti-parallel to parallel leads but also when making the transition from $\Gamma_R \ll \Gamma_L$ to a more symmetric coupling $\Gamma_R \sim \Gamma_L$, as shown in Fig. 3.4. In general, conductance peak spectra for different polarization orientations can therefore look very different in terms of both position and magnitude of the most dominant peaks, even if recorded for the same sample.

3.4 Influence of Spin-Orbit Scattering

The role of spin-orbit scattering inside the metal particle is best illustrated by considering the case of transport through one doubly (Kramers) degenerate level. (Spin-orbit scattering in the reservoirs instead of in the metal island was considered in Ref. [48].) With spin-orbit scattering, the two eigenfunctions of the level are spinor wave functions. Once the spin quantization axes are fixed at a reference point in the metal particle, the two spinor wave functions define a spatially dependent spin quantization axis in the metal particle. The spinors m_α and $\bar{m}_\alpha$ that define directions parallel and anti-parallel to the polarization direction in lead α are defined with respect to the quantization axis at the contact with lead α. Hence, the presence of spin orbit scattering in the normal-metal particle alters the spinor structure of the transition amplitudes γ_α, but it does not change the general

structure of the rate equations. The same conclusions hold for the general case.

The above considerations imply that, for a metal particle coupled to ferromagnetic source and drain reservoirs via two *point* contacts and with only a *single* level contributing to transport, the sole effect of spin-orbit scattering is a sample-specific shift of the angle between the polarizations in the two leads. On the other hand, for a metal particle coupled to source and drain leads via many-channel tunneling contacts, or for a metal particle in which more than one level contributes to transport, the effect of spin-orbit scattering is more complicated since different levels and different channels experience different rotations of the spin reference frame. In particular, with strong spin-orbit scattering, (spin) transport through different channels or through different levels will involve completely different rotation angles, so that the effective degree of spin polarization in the junction is greatly reduced. In the limit of a large number of channels and strong spin-orbit scattering, the rate equations in fact reduce to the unpolarized case.

3.5 Conclusion

We have extended the rate-equation formalism to the case of a normal island (metal nanoparticle, quantum dot, or single molecule) attached to spin-polarized contacts with non-collinear polarization directions. Our formalism provides a transparent description of the sequential tunneling processes in this system, and is suitable for application to both linear and nonlinear transport.

Whether one has to employ matrix rate equations or the simpler scalar rate equations is determined by the symmetries and energy degeneracies of the metal island and the leads. We distinguish the following cases: (i) leads and island have

the same symmetries and degeneracies, (ii) some symmetries present on the island are broken in the leads, and (iii) leads and island feature the same symmetries but there are additional degeneracies on the dot. Case (i) corresponds, e.g., to a normal-metal island with unpolarized leads and spin-degenerate energy levels on the dot, or to a normal-metal metal island with spin-polarized leads with collinear polarization directions. In that case, the standard rate equations of Refs. [34, 35] are applicable if there are no further degeneracies on the island. Case (i) also describes spin-polarized leads with non-collinear polarization directions if spin degeneracy on the island is lifted by a magnetic field, be it an applied field or the stray field of the ferromagnetic leads. In contrast, the other two situations require matrix rate equations: Case (ii) applies to normal-metal particles with ferromagnetic leads that are polarized in non-collinear directions so that tunneling occurs into coherent superpositions of states on the dot. The additional degeneracies required for case (iii) arise in the many-electron spectrum of generic metal particles with or without spin-polarized leads if the 'universal interaction Hamiltonian' describes the electron-electron interactions on the metal particle. Such degeneracies can be lifted by non-universal interaction corrections if the resulting energy splitting is larger than the level broadening due to escape to the leads. These corrections scale as $1/g$, where g is the dimensionless conductance of the metal particle, and as a consequence, the larger the size of the normal-metal island, the more important the use of matrix rate equations becomes.

BIBLIOGRAPHY

[1] I. Žutić, J. Fabian, and S. D. Sarma, Rev. Mod. Phys. **76**, 323 (2004).

[2] L. Berger, Phys. Rev. B **54**, 9353 (1996).

[3] J. C. Slonczewski, J. Magn. Magn. Mater. **159**, 1 (1996).

[4] M. Jullière, Phys. Lett. A **54**, 225 (1975).

[5] *Single Charge Tunneling*, Vol. 294 of *Nato ASI Series B*, edited by H. Grabert and M. H. Devoret (Plenum, New York, 1992).

[6] S. Guéron, M. M. Deshmukh, E. B. Myers, and D. C. Ralph, Phys. Rev. Lett. **83**, 4148 (1999).

[7] M. M. Deshmukh, S. Kleff, S. Guéron, E. Bonet, A. N. Pasupathy, J. von Delft, and D. C. Ralph, Phys. Rev. Lett. **87**, 226801 (2001).

[8] M. M. Deshmukh and D. C. Ralph, Phys. Rev. Lett. **89**, 266803 (2002).

[9] R. M. Potok, J. A. Folk, C. M. Marcus, V. Umansky, M. Hanson, , and A. C. Gossard, Phys. Rev. Lett. **91**, 016802 (2003).

[10] A. Pasupathy, R. Bialczak, J. Martinek, J. Grose, L. Donev, P. McEuen, and D. C. Ralph, Science **306**, 86 (2004).

[11] J. Barnaś and A. Fert, Phys. Rev. Lett. **80**, 1058 (1998).

[12] S. Takahashi and S. Maekawa, Phys. Rev. Lett **80**, 1758 (1998).

[13] A. Brataas, Y. V. Nazarov, J. Inoue, and G. E. W. Bauer, Phys. Rev. B **59**, 93 (1999).

[14] J. Barnaś, J. Martinek, G. Michalek, B. R. Bulka, and A. Fert, Phys. Rev. B **62**, 12363 (2000).

[15] W. Rudzinski and J. Barnaś, Phys. Rev. B **64**, 085318 (2001).

[16] G. Usaj and H. U. Baranger, Phys. Rev. B **63**, 184418 (2001).

[17] J. Martinek, J. Barnaś, S. Maekawa, H. Schoeller, and G. Schön, Phys. Rev. B **66**, 014402 (2002).

[18] N. Sergueev, Q. F. Sun, H. Guo, B. G. Wang, and J. Wang, Phys. Rev. B **65**, 165303 (2002).

[19] J. Fransson, O. Eriksson, and I. Sandalov, Phys. Rev. Lett. **88**, 226601 (2002).

[20] A. Cottet, W. Belzig, and C. Bruder, Phys. Rev. Lett. **92**, 206801 (2004).

[21] A. Cottet and W. Belzig, Europhys. Lett. **66**, 405 (2004).

[22] J. Ma and X. L. Lei, Europhys. Lett **67**, 432 (2004).

[23] J. Martinek, Y. Utsumi, H. Imamura, J. Barnaś, S. Maekawa, J. König, and G. Schön, Phys. Rev. Lett. **91**, 127203 (2003).

[24] J. Martinek, M. Sindel, L. Borda, J. Barnaś, J. König, G. Schön, and J. von Delft, Phys. Rev. Lett. **91**, 247202 (2003).

[25] M.-S. Choi, D. Sánchez, and R. López, Phys. Rev. Lett. **92**, 056601 (2004).

[26] J. Martinek, M. Sindel, L. Borda, J. Barnaś, R. Bulla, J. König, G. Schön, S. Maekawa, and J. von Delft, cond-mat/0406323 (2004).

[27] J. N. Pedersen, J. Q. Thomassen, and K. Flensberg, cond-mat/0412145 (2004).

[28] X. Waintal and P. W. Brouwer, Phys. Rev. Lett. **91**, 247201 (2003).

[29] J. König and J. Martinek, Phys. Rev. Lett. **90**, 166602 (2003).

[30] M. Braun, J. König, and J. Martinek, Phys. Rev. B **70**, 195345 (2004).

[31] R. I. Shekhter, Zh. Eksp. Teor. Fiz. **63**, 1410 (1972), [Sov. Phys. JETP **36**, 747 (1973)].

[32] I. O. Kulik and R. I. Shekhter, Zh. Eksp. Teor. Fiz. **68**, 623 (1975), [Sov. Phys. JETP **41**, 308 (1975)].

[33] D. V. Averin and K. K. Likharev, J. Low Temp. Phys. **62**, 345 (1986).

[34] C. W. J. Beenakker, Phys. Rev. B **44**, 1646 (1991).

[35] D. V. Averin, A. N. Korotkov, and K. K. Likharev, Phys. Rev. B **44**, 6199 (1991).

[36] Yu. V. Nazarov, Physica B **189**, 57 (1993).

[37] S. A. Gurvitz, Phys. Rev. B **57**, 6602 (1998).

[38] J. von Delft and D. C. Ralph, Phys. Rep. **345**, 61 (2001).

[39] I. L. Aleiner, P. W. Brouwer, and L. I. Glazman, Phys. Rep. **358**, 309 (2002).

[40] Y. Alhassid, T. Rupp, A. Kaminski, and L. I. Glazman, Phys. Rev. B **69**, 115331 (2002).

[41] A. Kaminski and L. I. Glazman, Phys. Rev. B **61**, 15927 (2000).

[42] B. Dong, H. L. Cui, and X. L. Lei, Phys. Rev. B **69**, 035324 (2004).

[43] T. K. Ng and P. A. Lee, Phys. Rev. Lett. **61**, 1768 (1988).

[44] L. I. Glazman and M. E. Raikh, Pis'ma Zh. Eksp. Teor. Fiz. **47**, 378 (1988), [JETP Lett. **47**, 452 (1988)].

[45] R. A. Jalabert, A. D. Stone, and Y. Alhassid, Phys. Rev. Lett. **68**, 3468 (1992).

[46] D. A. Gorokhov and P. W. Brouwer, Phys. Rev. Lett **91**, 186602 (2003).

[47] D. A. Gorokhov and P. W. Brouwer, Phys. Rev. B **69**, 155417 (2004).

[48] D. Mozyrsky, L. Fedichkin, S. A. Gurvitz, and G. P. Berman, Phys. Rev. B **66**, 161313(R) (2002).

Chapter 4

Vibrational Sidebands and Dissipative Tunneling in Molecular Transistors

4.1 Introduction

In the emerging field of single-molecule electronics, there is large interest in transport through mesoscopic systems with strong electron-phonon coupling. There has been a number of experiments in which transport through a single molecule has been reported [1, 2, 3, 4, 5, 6]. One example is the series of experiments by Park *et al.* [2] where it was shown that the current through a single C_{60} molecule was strongly coupled to a single vibrational mode. The single phonon mode was associated with the motion of the molecule in the confining potential created by the van der Waals interaction with the electrodes. Later, similar devices with more complicated molecules were investigated [3, 6], and they also showed excitation

spectra which may be associated with emission of vibrational quanta.

Theoretically, there has been a large amount of work on the problem of tunneling through a single level with coupling to phonon modes. In many experimental realizations the tunnel coupling to the leads is rather weak, and the transport is dominated by the well-known Coulomb blockade effect. In this regime, where the transport is sequential, the use of a rate-equation approach is appropriate rather than a coherent scattering approach. Motivated by the above mentioned single-molecule experiments, the rate-equation approach has been used in a number of recent papers [7, 8, 9]. These studies also dealt with the issue of non-equilibrium phonon states and with the possibility of having negative differential conductance in such molecular systems. Physically, it is an essential question how the excited vibrational levels are allowed to relax, either through coupling to the environment, for example the phonons or plasmons of the metal substrate, or by virtue of the tunneling electrons [10]. In the case where the relaxation of the vibrational modes is faster than the tunneling rate one can assume an equilibrium phonon distribution.

The coupling between the vibrational mode and the environment depends strongly on which vibrational mode is considered. For intra-molecular vibrations the lifetime can be very long [11, 12]. However, for the experiments of Ref. [2], it was suggested that the vibrational motion was associated with a center-of-mass motion, which is coupled to the environment more strongly as we discuss in this chapter. A sketch of the physical setup that we consider is shown in Fig. 4.1.

In this chapter, we assume that the tunneling rate is much smaller than the rate of relaxation to other degrees of freedom. Hence, the usual rate-equation approach is applicable, and we can assume that the phonons relax between each tunneling

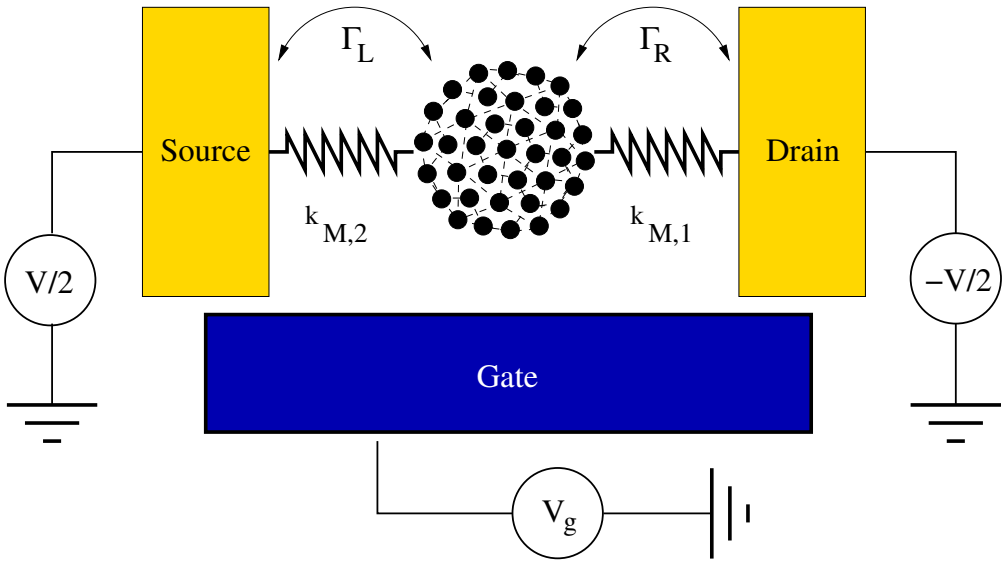

Figure 4.1: Illustration of the molecular transistor.

The molecule is attached to substrates, for instance by van der Waals interactions, and the movement in this potential is modeled by springs with spring constants $k_{M,1}$ and $k_{M,2}$. When an electron hops onto the molecule, the force created by image charges or local electric fields causes a shift of the equilibrium position of the oscillator and consequently emission of quanta. The weights of the different final states are given by the well-known Franck-Condon overlap factors. The main objective of this chapter is to consider the influence of damping of the molecular motion by emission of phonons into the substrates.

event according to a thermal boson distribution. We study a model of one single molecular orbital with strong Coulomb repulsion coupled to a dissipative environment. The dissipation is caused by coupling to phonon modes of the electrodes as well as electromagnetic modes and it is represented by a bath of harmonic oscillators. The description is thus similar to the well-known theory of Coulomb blockade in an electromagnetic environment [13, 14, 15, 16]. However, there is a difference in how the coupling to the environment appears. In the electromagnetic environment case, the tunneling of an electron results in a sudden displacement of the position of the charge, while here the tunneling results in a sudden appearance of a force on the oscillator. For this reason, we go through the derivations in some detail and derive a general formula for the I-V curves. This general result does not depend on the nature of the environment but we then specialize to two cases. We consider a molecule attached to a substrate, using a continuum model for the substrate, and compare our result to a reference model featuring frequency-independent damping and quality factor. The I-V curves, as a function of the elastic parameters of the substrate and the size of the molecule, feature quite different line shapes as compared to the assumption of constant friction.

To get a simple estimate of the importance of the coupling to the substrate, consider a model in which the molecule position x_0 is coupled to a one-dimensional substrate through a spring with spring constant k_M. For small substrate displacements, force balance gives that

$$-k_M x_0 \approx v_s^2 \rho_{1\mathrm{D}} \left(\frac{\partial u(x)}{\partial x} \right)_{x=0}, \tag{4.1}$$

where $u(x)$ is the substrate displacement, $\rho_{1\mathrm{D}}$ is the 1D mass density, and v_s is the sound velocity. At a given frequency ω, the outgoing sound waves are $u(x,\omega) = ae^{ix\omega/v_s}$, where a is a constant. Finding a from (4.1), we can insert it

into the equation of motion for x_0 to obtain the quality factor Q at the resonance frequency ω_0:

$$Q = \frac{m_0 \rho_{1\mathrm{D}} v_s \omega_0^3}{k_M^2} = \frac{\rho_{1\mathrm{D}} v_s}{m_0 \omega_0} = \frac{m}{m_0}, \tag{4.2}$$

where m_0 is the molecule mass with $\omega_0^2 = k_M/m_0$, and $m = \rho_{1\mathrm{D}} v_s/\omega_0$ is the mass of a wavelength long piece of the substrate. With realistic parameters for a C_{60} molecule on a gold substrate, as was used in the experiments of Ref. [2], the quality factor is between 1 and 10, and therefore we expect the broadening to be substantial. This furthermore confirms the assumption that, for this type of molecular device, relaxation through the environment is much faster than through tunneling.

The chapter is organized as follows. The model Hamiltonian is defined in Sec. 4.2, and in Sec. 4.3 we derive an expression for the current from rate equations. The function that describes the tunneling density of states is then solved in absence of the dissipative environment in Sec. 4.4 and with coupling to the environment in Sec. 4.5. We discuss different models for the dissipative coupling in Sec. 4.6, where we also discuss the physical implications. In Sec. 4.7, examples of I-V curves are displayed, and finally, a summary as well as a comparison with the experiments of Ref. [2] can be found in Sec. 4.8.

4.2 Model Hamiltonian

We consider a model of one single spin-degenerate molecular level coupled to two leads (generalization to more molecular levels is straightforward). The single level is coupled to the vibrational mode of the molecule through the charge on the dot. The coupling between the oscillator and the environment is included as a linear

coupling to a bath of harmonic oscillators in the spirit of the theory by Caldeira and Leggett [17]. The model Hamiltonian then reads

$$H = H_{LR} + H_D + H_B + H_{DB} + H_{\text{bath}} + H_{B\text{bath}} + H_T, \tag{4.3}$$

with

$$H_{LR} = \sum_{k\sigma,\,\alpha=L,R} \xi_{k\alpha} c^\dagger_{k\sigma,\alpha} c_{k\sigma,\alpha}, \tag{4.4a}$$

$$H_D = \sum_\sigma \xi_0 d^\dagger_\sigma d_\sigma + U n_{d\uparrow} n_{d\downarrow}, \tag{4.4b}$$

$$H_{\text{B}} = \frac{p_0^2}{2m_0} + \frac{1}{2} m_0 \omega_0^2 x_0^2, \tag{4.4c}$$

$$H_{DB} = \lambda x_0 \sum_\sigma d^\dagger_\sigma d_\sigma, \tag{4.4d}$$

$$H_{\text{bath}} = \sum_j \left(\frac{p_j^2}{2m_j} + \frac{1}{2} m_j \omega_j^2 x_j^2 \right), \tag{4.4e}$$

$$H_{B\text{bath}} = \sum_j \beta_j x_j x_0, \tag{4.4f}$$

where the $c^\dagger_{k\sigma,\alpha}$, $c_{k\sigma,\alpha}$ and the $d^\dagger_\sigma$, d_σ are creation and annihilation operators for the leads and the dot, respectively, x_0 is the oscillator degree of freedom, $\{x_j\}$ describes the set of environmental degrees of freedom and m_j, ω_j their respective masses and frequencies, ξ_0 is the on-site energy, and U is the Coulomb interaction on the molecule. The coupling constants for the electron-oscillator interaction and the oscillator-bath interaction are λ and $\{\beta_j\}$, respectively. The lead electron energies are given by

$$\xi_{k\alpha} = \varepsilon_{k\alpha} - \mu_\alpha, \tag{4.5}$$

where $\varepsilon_{k\alpha}$ is the energy of electron state k in lead α, and μ_α is the chemical potential of lead α. Finally, the tunnel Hamiltonian is

$$H_T = \sum_{k\sigma,\,\alpha=L,R} t_{k\alpha} (c^\dagger_{k\sigma,\alpha} d_\sigma + d^\dagger_\sigma c_{k\sigma,\alpha}). \tag{4.6}$$

The tunneling amplitudes could in principle also depend on the oscillator position. In the experimental realizations in Refs. [2, 3, 4], this is probably a small effect since the oscillation amplitude is of order a few pm whereas the tunneling matrix element changes on the scale of nm. For simplicity, we do not take any such non-linear effects into account, but we note that a position dependence of the tunneling amplitudes, for example of the form $\exp(-x_0/\ell_t)$, could easily be included in the present formalism.

The force acting on the charged molecule, represented by the term H_{DB}, is caused by electric fields originating from either static impurity charges or image charges. Since this force on the molecule is counteracted by a force on these charges and, hence, on the environment, we should in principle also include the interaction between the environmental coordinates and the charge on the molecule. This would in fact lead to a qualitatively different behavior since Ohmic dissipation is cut off at frequencies smaller than the inverse size of the total system, i.e., the inverse range of the interaction between the charge on the molecule and the charges in the environment. This interesting subtlety was pointed out in Ref. [18]. However, since the van der Waals interaction between molecule and substrate is short ranged compared to the electrostatic forces, we will consider the force acting on the molecule as an external quantity, which is thus not coupled to the dissipative environment. We do note, however, that including such a coupling would in fact lead to a small discontinuity at the onset of conductance in the I-V curve, see Chapter 5. The experimental data of, e.g., Ref. [2] do not seem to suggest such a discontinuity, and we therefore specialize to the case where the environmental coordinates are unaffected by the charge on the molecule.

We now want to relate the coupling constants in the boson-bath coupling to the

finite damping of the vibrational mode, which can be accomplished by studying the classical equations of motion. After removing the bath degrees of freedom, thereby neglecting the term H_{DB} that will be removed by a unitary transformation below, we end up with the following equation of motion in the frequency domain:

$$[\omega^2 - \omega_0^2 - \mathcal{S}(\omega)]x_0(\omega) = 0, \tag{4.7}$$

where we have defined

$$\mathcal{S}(\omega) = \frac{1}{m_0}\sum_j \frac{\beta_j^2}{m_j}\frac{1}{(\omega + i\eta)^2 - \omega_j^2}, \tag{4.8}$$

which is complex in general and gives rise to frictional damping and a frequency shift of the bare frequency ω_0. In Sec. 4.6.2, we will explicitly calculate $\mathcal{S}(\omega)$ for the case of a molecule attached to a semi-infinite substrate.

We eliminate the coupling term H_{DB} of the Hamiltonian (4.4) by a unitary transformation similar to the one used in the independent-boson model [19], at the cost of introducing displacement operators in the tunneling term. However, since we are dealing with a somewhat more complicated system due to the coupling to the bosonic bath, the unitary transformation in Ref. [19] has to be generalized. We define the transformation

$$\tilde{H} = SHS^\dagger, \quad S = e^{-iAn_d}, \quad A = p_0\ell + \sum_j p_j\ell_j, \tag{4.9}$$

where $n_d = \sum_\sigma d_\sigma^\dagger d_\sigma$. Using that

$$\tilde{x}_0 = x_0 - \ell n_d, \quad \tilde{x}_j = x_j - \ell_j n_d, \tag{4.10}$$

it is a matter of simple algebra to show that the linear coupling term H_{DB} cancels if we set

$$\ell = \frac{\lambda}{m_0[\omega_0^2 + \mathcal{S}(0)]}, \quad \ell_j = \frac{-\ell\beta_j}{m_j\omega_j^2}, \tag{4.11}$$

and the Hamiltonian then transforms into

$$\tilde{H} = H_{LR} + \tilde{H}_D + H_B + H_{\text{bath}} + H_{B\text{bath}} + \tilde{H}_T, \tag{4.12}$$

where

$$\tilde{H}_T = \sum_{k\sigma,\,\alpha=L,R} t_{k\sigma,\alpha} \left(c^\dagger_{k\sigma,\alpha} e^{iA} d_\sigma + d^\dagger_\sigma e^{-iA} c_{k\sigma,\alpha} \right) \tag{4.13}$$

and

$$\tilde{H}_D = \varepsilon_0 \sum_\sigma d^\dagger_\sigma d_\sigma + \tilde{U} n_{d\downarrow} n_{d\uparrow}, \quad \varepsilon_0 = \xi_0 - \frac{1}{2}\lambda\ell. \tag{4.14}$$

Here, $\tilde{U} = U - \lambda\ell$ is the Coulomb repulsion modified by the phonon-mediated interaction. For weak Coulomb interaction, this can result in a negative effective U, which was discussed in Ref. [20].

4.3 Rate Equations and Current Formula

We derive an expression for the current in the weak tunneling limit using the usual kinetic-equation approach. As mentioned in Sec. 4.1, the most important assumption here is that the tunneling rate is much smaller than all other time scales, which means that we can assume the vibrational degrees of freedom and the Fermi seas in the two electrodes to be in equilibrium at all times. For simplicity, we consider only two charge states and therefore let $U = \infty$, which leaves us with only three states: empty, and occupied by either spin up or spin down. The probabilities for the three states are denoted P_0, $P_\uparrow$, and $P_\downarrow$, respectively. The rate equations are

$$\begin{pmatrix} -2\Gamma_{10} & \Gamma_{01} & \Gamma_{01} \\ \Gamma_{10} & -\Gamma_{01} & 0 \\ \Gamma_{10} & 0 & -\Gamma_{01} \end{pmatrix} \begin{pmatrix} P_0 \\ P_\uparrow \\ P_\downarrow \end{pmatrix} = 0, \tag{4.15}$$

which, combined with the condition $P_0 + P_\uparrow + P_\downarrow = 1$, has the solution

$$P_0 = \frac{\Gamma_{01}}{\Gamma_{01} + 2\Gamma_{10}}, \quad P_\downarrow = P_\uparrow = \frac{\Gamma_{10}}{\Gamma_{01} + 2\Gamma_{10}}, \tag{4.16}$$

where Γ_{10} is the tunneling rate for tunneling from the empty state to a singly occupied state, and Γ_{01} is the rate for the reverse process. Since the electron can tunnel out of both left and right leads, both rates have left and right contributions: $\Gamma_{ij} = \Gamma_{ij}^L + \Gamma_{ij}^R$. The tunneling rates are calculated using Fermi's Golden Rule, thereby treating $\tilde{H}_T$ of Eq. (4.13) as the perturbation and assuming a thermal equilibrium distribution of the lead electrons and the phonon bath. Following standard derivations, we obtain

$$\Gamma_{10}^\alpha = \Gamma_\alpha \int \frac{d\omega}{2\pi} F(\omega) n_\alpha(\varepsilon_0 + \omega), \tag{4.17a}$$

$$\Gamma_{01}^\alpha = \Gamma_\alpha \int \frac{d\omega}{2\pi} F(-\omega)(1 - n_\alpha(\varepsilon_0 + \omega)), \tag{4.17b}$$

where we have defined the function

$$F(\omega) = \int_{-\infty}^{\infty} dt\, e^{i\omega t} F(t), \quad F(t) = \langle e^{iA(t)} e^{-iA} \rangle, \tag{4.18}$$

in addition to the Fermi distributions of the two leads, $n_\alpha(\varepsilon) = (e^{\beta(\varepsilon - eV_\alpha)} + 1)^{-1}$, and the bare rates $\Gamma_\alpha = 2\pi \sum_k |t_{k\alpha}|^2 \delta(\xi_k)$. The function F has the properties

$$F(\omega) = F(-\omega) e^{\beta\omega}, \quad \int_{-\infty}^{\infty} \frac{d\omega}{2\pi} F(\omega) = 1. \tag{4.19}$$

We can use Eq. (4.19) to show that the rates in Eq. (4.17) can be written as

$$\Gamma_{10}^\alpha = \Gamma_\alpha \tilde{n}_\alpha, \quad \Gamma_{01}^\alpha = \Gamma_{10}^\alpha e^{\beta(\varepsilon_0 - eV_\alpha)}, \tag{4.20}$$

where we have defined

$$\tilde{n}_\alpha = \int \frac{d\omega}{2\pi} F(\omega) n_\alpha(\omega + \varepsilon_0). \tag{4.21}$$

The current through the molecule is given by

$$I = -e(2P_0\Gamma_{10}^L - \left(P_\uparrow + P_\downarrow\right)\Gamma_{01}^L) = 2e\frac{\Gamma_{10}^R\Gamma_{01}^L - \Gamma_{01}^R\Gamma_{10}^L}{\Gamma_{01} + 2\Gamma_{10}}. \tag{4.22}$$

Using Eq. (4.20), this can also be written as

$$I = \frac{2e\Gamma_L\Gamma_R\tilde{n}_R\tilde{n}_L\left(e^{\beta(\varepsilon_0 - eV_L)} - e^{\beta(\varepsilon_0 - eV_R)}\right)}{\Gamma_L\tilde{n}_L(2 + e^{\beta(\varepsilon_0 - eV_L)}) + \Gamma_R\tilde{n}_R(2 + e^{\beta(\varepsilon_0 - eV_R)})}. \tag{4.23}$$

4.4 Without Coupling to the Environment

We start by discussing the limit when the oscillator is not coupled to the environment, which means that thermal smearing dominates over dissipative broadening. However, we still assume that the coupling is stronger than the tunnel coupling so that the molecule equilibrates between each tunneling event. This section is thus equivalent to the results in other rate-equation calculations, but for completeness and later comparison we write down this limiting case explicitly.

The phonon average is performed assuming thermal equilibrium, and we have

$$\begin{aligned} F_0(t) &= \left\langle e^{ip_0(t)\ell}e^{-ip_0(0)\ell}\right\rangle, \\ &= \exp\left\{g\left(e^{-i\omega_0 t} - 1\right)(1+N) + g\left(e^{i\omega_0 t} - 1\right)N\right\}, \end{aligned} \tag{4.24}$$

where

$$g = \frac{1}{2}\left(\frac{\ell}{\ell_0}\right)^2, \quad \ell_0^2 = \frac{1}{m_0\omega_0}, \quad N = n_B(\omega_0). \tag{4.25}$$

Here, g is an important parameter determined by the ratio of the classical displacement length and the quantum mechanical oscillator length. The evaluation of $F_0(\omega)$ from Eq. (4.24) is equivalent to the independent-boson model [19], and using the result from there we get

$$F_0(\omega) = 2\pi\sum_{n=-\infty}^{\infty} P_n(g)\delta(\omega - n\omega_0), \tag{4.26}$$

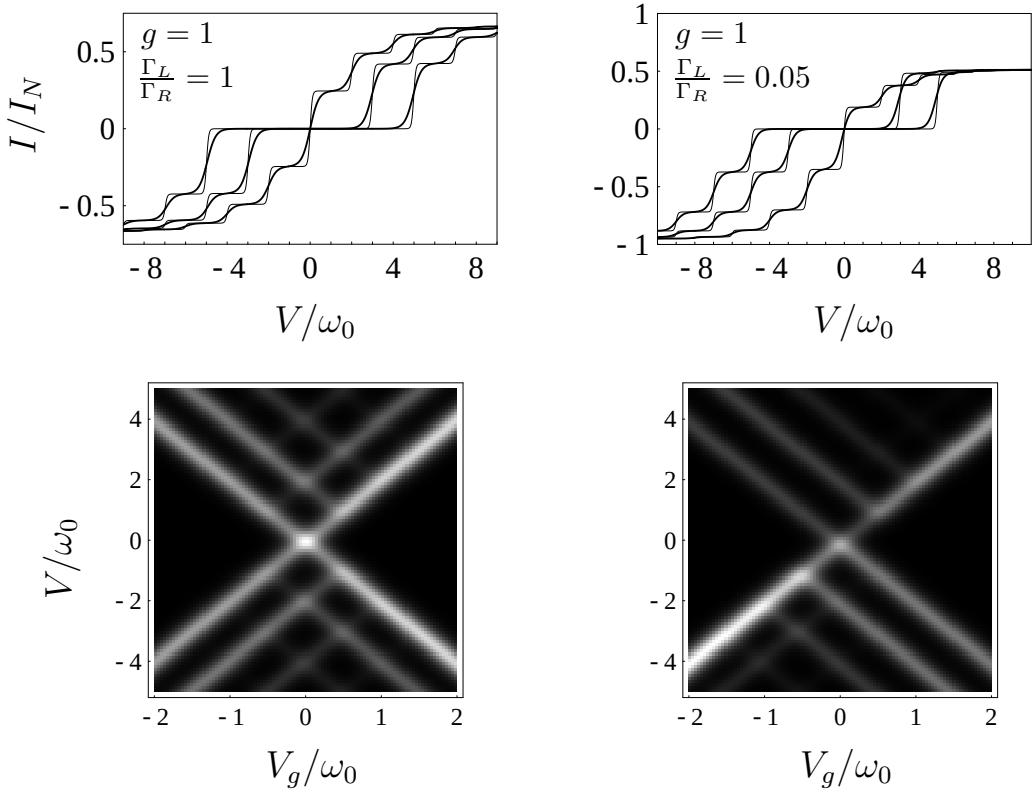

Figure 4.2: I-V characteristics without coupling to the environment.

Upper panels: I-V characteristics for a device without coupling to the environment for symmetric ($\Gamma_R = \Gamma_L$) and asymmetric ($\Gamma_R = 0.05\Gamma_L$) tunneling contacts. Lower panels: contour plot of the differential conductance in the voltage-gate voltage plane, where $eV_g = \varepsilon_0$. The curves have been calculated using the analytic result Eq. (4.23), valid in the limit where the lifetime broadening of the oscillator is negligible. The temperature is $k_BT = 0.1\omega_0$ for the thick lines and in the contour plots, while the thin lines are for $k_BT = 0.025\omega_0$. The bias is applied symmetrically $V_L = V/2 = -V_R$, and in the I-V curves we take ε_0 to be 0, 1.5, and 2.5 times ω_0. The current is measured in units of $I_N = e\Gamma_L\Gamma_R/(\Gamma_L + \Gamma_R)$.

where

$$P_n(g) = \exp(-g\coth(b))e^{nb}I_n\left(\frac{g}{\sinh(b)}\right), \quad b = \frac{\beta\omega_0}{2}, \tag{4.27}$$

and I_n is the modified Bessel function of the first kind. The finite-temperature result involves both positive and negative values of n, corresponding to emission and absorption of phonons, respectively. At zero temperature, this reduces to having only positive values of n because of the factor $e^{n\beta\omega_0/2}$, and hence only emission processes are possible. In the limit $T \to 0$, we thus have a series of emission peaks at $\omega = n\omega_0$ for positive n and with weights given by the Poisson distribution $P_n \to e^{-g}g^n/n!$.

The current can now be found from Eq. (4.23). In Fig. 4.2, we show examples of I-V characteristics using Eq. (4.23) for symmetric and asymmetric junctions. In the following, we study how the physics gets modified by the coupling to the environment.

4.5 With Coupling to the Environment

In presence of coupling to the environment, the evaluation of the function $F(t)$ in Eq. (4.18) is in principle straightforward since the Hamiltonian is quadratic in the oscillator and bath degrees of freedom. We obtain

$$F(t) = \exp\left(B(t) - B(0)\right), \quad B(t) = \langle A(t)A(0)\rangle_0, \tag{4.28}$$

where the operator A is defined in Eqs. (4.9) and (4.11). The expectation value $\langle\ldots\rangle_0$ is to be evaluated with respect to $\tilde{H}$ without the tunneling term. At this point, it is convenient to use the fluctuation-dissipation theorem,

$$B(\omega) = -2\,\mathrm{Im}[B^R(\omega)](1 + n_B(\omega)), \tag{4.29}$$

to express $B(t)$ in terms of the corresponding retarded Green's function

$$B^R(t) = -i\theta(t)\langle[A(t), A(0)]\rangle_0. \tag{4.30}$$

Here, $n_B(\omega) = (e^{\beta\omega} - 1)^{-1}$ is the usual Bose function. In order to find this retarded correlation function, we define the following auxiliary Green's functions:

$$G^R_{\mathcal{O}}(t) = -i\theta(t)\frac{1}{\ell}\langle[\mathcal{O}(t), A(0)]\rangle, \tag{4.31}$$

from which we obtain B^R as

$$\begin{aligned} B^R &= (\ell G^R_{p_0} + \sum_j \ell_j G^R_{p_j})\ell \\ &= \ell^2(G^R_{p_0} - \sum_j \frac{\beta_j}{m_j\omega_j^2} G^R_{p_j}). \end{aligned} \tag{4.32}$$

The equations of motion for these functions are in frequency domain given by

$$\begin{pmatrix} \omega & -i/m_0 \\ im_0\omega_0^2 & \omega \end{pmatrix} \begin{pmatrix} G^R_{x_0} \\ G^R_{p_0} \end{pmatrix} = \begin{pmatrix} i \\ 0 \end{pmatrix} - \sum_j \begin{pmatrix} 0 \\ i\beta_j G^R_{x_j} \end{pmatrix}, \tag{4.33}$$

$$\begin{pmatrix} \omega + i\eta & -i/m_j \\ im_j\omega_j^2 & \omega + i\eta \end{pmatrix} \begin{pmatrix} G^R_{x_j} \\ G^R_{p_j} \end{pmatrix} = \begin{pmatrix} \frac{-i\beta_j}{m_j\omega_j^2} \\ 0 \end{pmatrix} - \begin{pmatrix} 0 \\ i\beta_j G^R_{x_0} \end{pmatrix}. \tag{4.34}$$

Solving this linear set of equations for the Green's functions and inserting the results into Eq. (4.32), we obtain

$$B^R(\omega) = \frac{2g\bar{\omega}_0}{\omega^2 - \bar{\omega}_0^2 - \bar{\mathcal{S}}(\omega)}\left(1 - \frac{\bar{\mathcal{S}}(\omega)}{\omega^2}\right), \tag{4.35}$$

where we have defined $\bar{\mathcal{S}}(\omega) \equiv \mathcal{S}(\omega) - \mathcal{S}(0)$ and the experimentally observable renormalized frequency $\bar{\omega}_0^2 \equiv \omega_0^2 + \mathcal{S}(0)$. Using (4.29), the function $B(\omega)$ thus follows as

$$B(\omega) = -4g\,\frac{1 + n_B(\omega)}{\omega^2}\,\mathrm{Im}\left[\frac{\bar{\omega}_0^3}{\omega^2 - \bar{\omega}_0^2 - \bar{\mathcal{S}}(\omega)}\right], \tag{4.36}$$

where now $g = \ell^2/2\ell_0^2$ is defined with respect to the renormalized frequency $\bar{\omega}_0$, i.e., $\ell_0^2 = 1/m_0\bar{\omega}_0$. This result can then be used to find

$$F(t) = \exp\left(\int_{-\infty}^{\infty} \frac{d\omega}{2\pi}(e^{-i\omega t} - 1)B(\omega)\right). \tag{4.37}$$

Eq. (4.37) is equivalent to the result for the Coulomb blockade of a single tunnel junction with coupling to the electromagnetic environment [14, 15]. In the Coulomb-blockade problem, the tunneling density of states was related to the impedance as seen from the junction, here the I-V characteristic is in a similar way related to the frictional damping of the oscillator mode. In both cases, the low energy form of the spectrum is a power law at low temperatures. At small frequencies $\omega \ll \bar{\omega}_0$ and zero temperature, we get the following power-law behavior,

$$F(\omega) \propto \omega^{\alpha-1}, \quad \alpha = \frac{2g}{\bar{\omega}_0\pi} \lim_{\omega\to 0}\left(\frac{-\mathrm{Im}\bar{\mathcal{S}}(\omega)}{\omega}\right). \tag{4.38}$$

Furthermore, we use the trick by Minnhagen [21] to find the F-function as the solution of the integral equation

$$F(\omega) = \frac{1}{\omega}\int_0^{\omega} \frac{d\zeta}{2\pi} F(\zeta)B(\zeta-\omega)(\zeta-\omega), \tag{4.39}$$

which is useful for the numerical evaluation of F.

4.6 Models for $\mathcal{S}(\omega)$

4.6.1 Frequency-independent quality factor Q

As a first attempt, we can assume $\mathcal{S}$ to be of the form

$$\mathcal{S}(\omega) = \mathcal{S}(0) - i\frac{\omega\bar{\omega}_0}{Q}, \tag{4.40}$$

which leads to a frequency-independent quality factor Q of the single vibrational mode, similar to the Ohmic-dissipation model by Caldeira and Leggett in Ref. [17]. The model is also similar to the Coulomb blockade problem of an LCR circuit [16], which is described by the same formula. The limit $Q \to \infty$ is seen to coincide with the results in Sec. 4.4 since in this limit $B(\omega) \to 2\pi(1 + n_B(\omega))(\pm)\delta(\omega \pm \bar{\omega}_0)$, and when this is inserted into Eq. (4.37), we get (4.24). We also see that, for a critical value of $Q_c = 2g/\pi$, the function F and, hence, the differential conductance change from having a divergence at small energies to vanish at small energies.

In Fig. 4.3, we plot the function F and its integral for different values of g and Q. It is clearly seen how the increasing dissipation smears the Franck-Condon steps. For strongly under-damped coupling to the environment, the steps are only weakly smeared, and still visible even for $Q = 2.5$. For the special value of

$$Q = Q_c = \frac{2g}{\pi}, \tag{4.41}$$

the first step disappears and eventually for very small Q the function F goes toward a delta function, $F \to 2\pi\delta(\omega - g\bar{\omega}_0)$. Physically, this means that in the small-Q limit, the system relaxes immediately to the classical state and tunneling is only possible by paying the total classical energy cost of the displacement. To see this, we rewrite $g\bar{\omega}_0$ in terms of the coupling constant λ and get $\lambda\ell/2 = \lambda^2/2m_0\bar{\omega}_0^2$, which is the classical energy for displacing the oscillator by increasing the occupation n_d by one.

The crossover to the classical regime occurs when the lifetime of the oscillator, $Q/\bar{\omega}_0$, is comparable to the Heisenberg uncertainty time associated with the classical energy of the displaced oscillator, i.e., when (reinserting $\hbar$)

$$\frac{Q_q}{\bar{\omega}_0} \equiv \frac{\hbar}{\lambda\ell/2}, \quad \Rightarrow \quad Q_q = \frac{1}{g}\,. \tag{4.42}$$

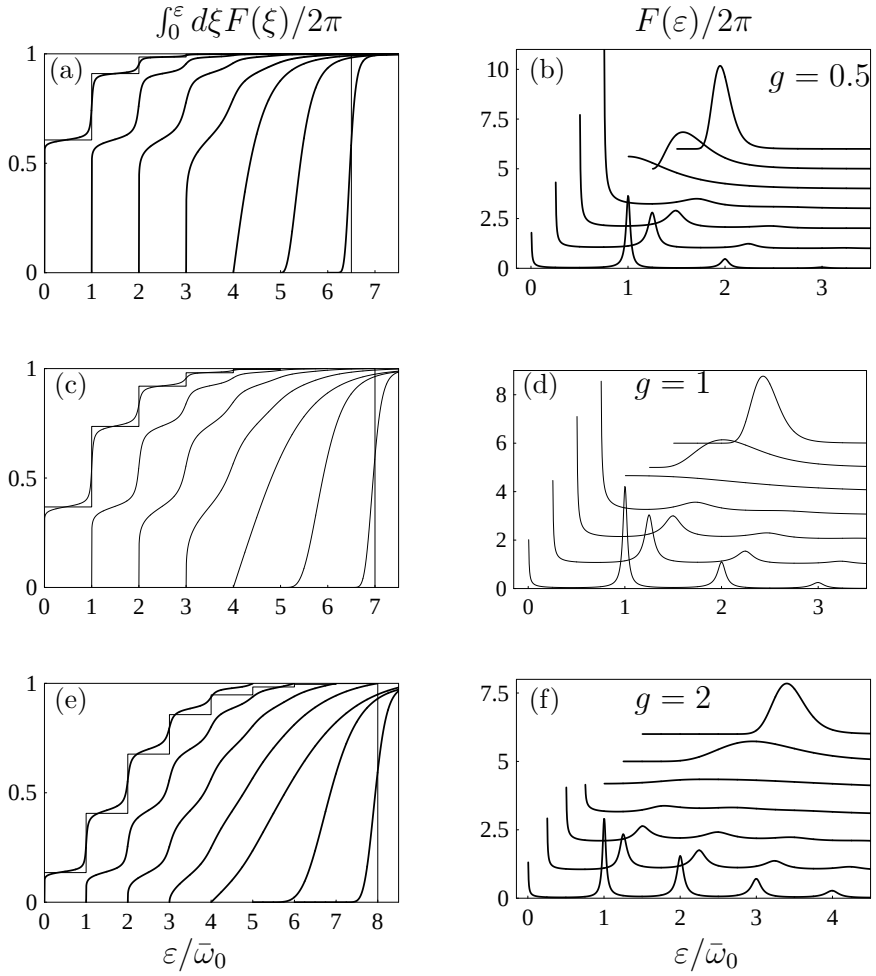

Figure 4.3: The function $F(\xi)$ and its integral for different values of g and frequency-independent Q.

The curves have been calculated from Eq. (4.39) at zero temperature. We take Q=20, 10, 5, 2.5, 2g/π, 0.1, 0.01, where $g = 0.5$ in (a) and (b), $g = 1$ in (c) and (d), and $g = 2$ in (e) and (f). The curves have been displaced for clarity by multiples of (1,0) in (a), (c), and (e), and by multiples of (0.25,1) in (b), (d), and (f) (largest Q to the left). For large Q, the integrated function goes to the dissipationless results, where the step heights are given by the Poisson distribution (leftmost staircase in (a), (c), and (e)), whereas for small Q it goes to a step function at $\varepsilon = g\bar{\omega}_0$ (vertical line). Note also that the differential conductance at the first step remains sharp while the higher order steps are smeared when $Q > Q_c$.

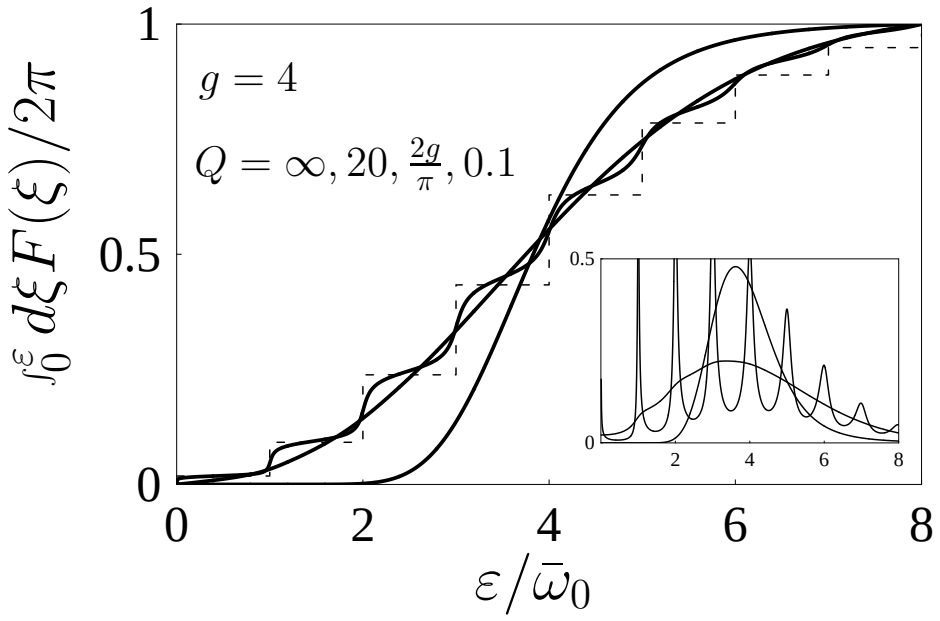

Figure 4.4: The integral of the function F for $g = 4$ and different Q at zero temperature.

We take $Q = \infty$ (dashed line), 20, $8/\pi$, 0.1. At $Q \lesssim Q_c$ the steps disappear, while for $Q \lesssim Q_q$ the curves approach the classical limit, which is a step function at $\varepsilon = 4\bar{\omega}_0$. The inset shows the F-function itself for the same parameters.

The disappearance of the steps, which happens at Q_c, is therefore different from the crossover to the classical regime. This is shown in Fig. 4.4 where we plot the integral of F for $g = 4$ for different values of Q. For $Q = 20$, the steps are only slightly broadened, while for $Q = Q_c$, the steps are almost fully broadened but the line still follows the quantum behavior. Only for smaller Q do we approach the classical result, which is a step function at $g\bar{\omega}_0$.

4.6.2 Coupling to a substrate

We consider a molecule of mass m_0 attached to a substrate that extends over the semi-infinite half-space $x \geq 0$. The case of two substrates, as is shown in Fig. 4.1, is a straightforward generalization and will be discussed at the end of the calculation. The 3D Lagrangian density for the substrate is given by [22]

$$\mathcal{L}(\vec{r},t) = \frac{1}{2}\rho\left[(\partial_t\vec{u})^2 - (v_l^2 - 2v_t^2)\left(\vec{\nabla}\vec{u}\right)^2 - v_t^2(\vec{\nabla}\times\vec{u})^2 - 2v_t^2\frac{\partial u_i}{\partial x_j}\frac{\partial u_j}{\partial x_i}\right], \quad (4.43)$$

where v_l and v_t are the longitudinal and transverse sound velocities, and ρ is the mass density. This Lagrangian leads to the following equation of motion,

$$\partial_t^2\vec{u} - v_l^2\vec{\nabla}(\vec{\nabla}\vec{u}) + v_t^2\vec{\nabla}\times\vec{\nabla}\times\vec{u} = 0. \quad (4.44)$$

Having in mind a small molecule attached to the origin, the assumption of cylindrical symmetry around the x-axis seems reasonable. We define u_r and u_x as the displacements in radial direction and parallel to the x-axis, respectively.

We consider the case that the molecule only exerts a total force $\mathcal{F}$ perpendicular to the substrate surface,

$$\mathcal{F} = k_M\left[x - \int_0^\infty 2\pi r f(r) u_x^0(r) dr\right], \quad (4.45)$$

where $u_x^0(r)$ is the parallel displacement at the surface defined by $x = 0$, and $f(r)$ is a normalized distribution function, $\int 2\pi r f(r) dr = 1$. This imposes the following boundary conditions on the stress tensor T:[1]

$$T_{xr}|_{x=0} = 0, \qquad T_{xx}|_{x=0} = -\mathcal{F} f(r), \tag{4.46}$$

where the components T_{xr} and T_{xx} can be written as functions of the displacements u_r and u_x (see for instance Refs. [23, 24]). The solution is then a straightforward generalization of the procedure for a point source with $f(r) \propto \delta(r)/r$ outlined by Lamb in Ref. [25]. We obtain in frequency space

$$u_x^0(r) = \mathcal{F} \frac{\omega^2}{v_t^2} \int_0^\infty \frac{k \nu_l f_k}{G(k,\omega)} J_0(kr) dk, \tag{4.47}$$

where we have defined the following quantities:

$$\nu_{t,l} = \begin{cases} \sqrt{k^2 - \frac{\omega^2}{v_{t,l}^2}} & \text{if } k^2 \geq \frac{\omega^2}{v_{t,l}^2}, \\ -i\sqrt{k^2 - \frac{\omega^2}{v_{t,l}^2}} & \text{if } k^2 < \frac{\omega^2}{v_{t,l}^2}, \end{cases} \tag{4.48}$$

$$G(k,\omega) = 4\mu_L \nu_l \nu_t k^2 - (\lambda_L + 2\mu_L)(\nu_t^2 + k^2)\nu_l^2 + \lambda_L k^2 \nu_t^2 + \lambda_L k^4, \tag{4.49}$$

where μ_L and λ_L are the Lamé coefficients, which are related to the sound velocities as

$$v_l = \sqrt{\frac{\lambda_L + 2\mu_L}{\rho}}, \qquad v_t = \sqrt{\frac{\mu_L}{\rho}}, \tag{4.50}$$

and f_k is the Fourier-Bessel transform of the force distribution $f(r)$,

$$f_k = \int_0^\infty f(r) J_0(kr) r dr. \tag{4.51}$$

The $(-)$-sign in the definition of $\nu_{t,l}$ in Eq. (4.48) is necessary for selecting the retarded response $\omega \to \omega + i\eta$ corresponding to outgoing waves since the square-root function has a branch cut on the negative real axis.

[1]The stress tensor is defined as $d\vec{F} = T d\vec{A}$, where $d\vec{F}$ is an infinitesimal force, and $d\vec{A}$ is an infinitesimal area element.

The total force $\mathcal{F}$ involves $u_x^0(r)$ and vice versa, see Eqs. (4.45) and (4.47), so that we obtain

$$\int_0^\infty 2\pi r f(r) u_x^0(r) dr = x \frac{R(\omega)}{1+R(\omega)}, \tag{4.52}$$

where

$$R(\omega) = k_M \frac{2\pi\omega^2}{v_t^2} \int_0^\infty \frac{k\nu_l f_k^2}{G(k,\omega)} dk. \tag{4.53}$$

The function of interest, $\mathcal{S}(\omega)$, can then be deduced from the equation of motion for the molecule in frequency space,

$$-M\omega^2 x_0(\omega) = -k_M \left[x_0(\omega) - \int_0^\infty 2\pi r f(r) u_x^0(r) dr \right]. \tag{4.54}$$

Identifying k_M/ω_M with the bare frequency ω_0^2, we obtain

$$\left[\omega^2 - \omega_0^2 + \omega_0^2 \frac{R(\omega)}{1+R(\omega)} \right] x_0(\omega) = 0, \tag{4.55}$$

which implies upon comparison with Eq. (4.7)

$$\mathcal{S}(\omega) = -\omega_0^2 \frac{R(\omega)}{1+R(\omega)}. \tag{4.56}$$

For the situation where the molecule is attached to two substrates it can be seen that the function $\mathcal{S}(\omega)$ becomes instead

$$\mathcal{S}(\omega) = -\frac{k_{M,1}}{M} \frac{R_1(\omega)}{1+R_1(\omega)} - \frac{k_{M,2}}{M} \frac{R_2(\omega)}{1+R_2(\omega)}, \tag{4.57}$$

where $R_{1,2}$ is given by Eq. (4.53) but with k_M replaced by $k_{M1,2}$ and, if the two substrates are different, with substrate parameters changed accordingly. However, because of the lack of detailed knowledge about the actual geometry of the device, and since the coupling to the two sides of the junction is very likely to be asymmetric, we will in the following make the simplifying assumption that the molecule only couples to one substrate.

Our results for $R(\omega)$ in Eq. (4.53) imply that the imaginary part of $\mathcal{S}(\omega)$ (which will eventually be responsible for the frictional damping) has contributions not only from extended waves in the substrate but also from waves that are confined to the surface, the so-called *Rayleigh* waves. Mathematically, this contribution arises from $G(k,\omega)$ being zero for a specific value of k. This value falls into the regime where both ν_t and ν_l are real, i.e., where wave vectors k are larger than allowed for transversal and longitudinal waves, see Eq. (4.48) [25].

In order to compare our result (4.56) to experimental data, we need to choose a specific model for the force distribution function $f(r)$. The most realistic model would involve a distribution in accord with the van der Waals potential, however, as a result of that f_k is a rather involved function of k. For simplicity, we therefore choose

$$f(r) = \frac{1}{2\pi D^2} e^{-r/D}, \quad \Rightarrow \quad f_k = \frac{1}{2\pi\sqrt{1+k^2D^2}^3}. \tag{4.58}$$

The parameter D is on the order of the width D_0 of the molecule, e.g., $D_0 = 10.4\text{Å}$ for a C_{60} molecule. For this model, we can explicitly extract $\mathcal{S}(0)$, since then

$$R(0) = \frac{3}{64} \frac{\omega_0^2 M \alpha^4}{(\alpha^2-1)\,\rho v_l^2 D}, \tag{4.59}$$

where $\alpha \equiv v_l/v_t$. Note that $R(0)$ is proportional to the squared bare frequency $\omega_0^2 = \bar{\omega}_0^2 - \mathcal{S}(0)$ so that we end up with

$$\mathcal{S}(0) = -\bar{\omega}_0^2 \frac{\bar{\omega}_0^2 R(0)/\omega_0^2}{1+\bar{\omega}_0^2 R(0)/\omega_0^2}. \tag{4.60}$$

This result has the particular effect on the damping coefficient $\text{Im}\mathcal{S}(\omega)/\omega$ that it is independent of D/D_0 at zero frequency. We show plots of the real and imaginary parts of $\mathcal{S}(\omega)$ in Fig. 4.5. The real part, and thus the renormalization of the bare frequency as a function of energy, goes to zero rather quickly, whereas the imaginary

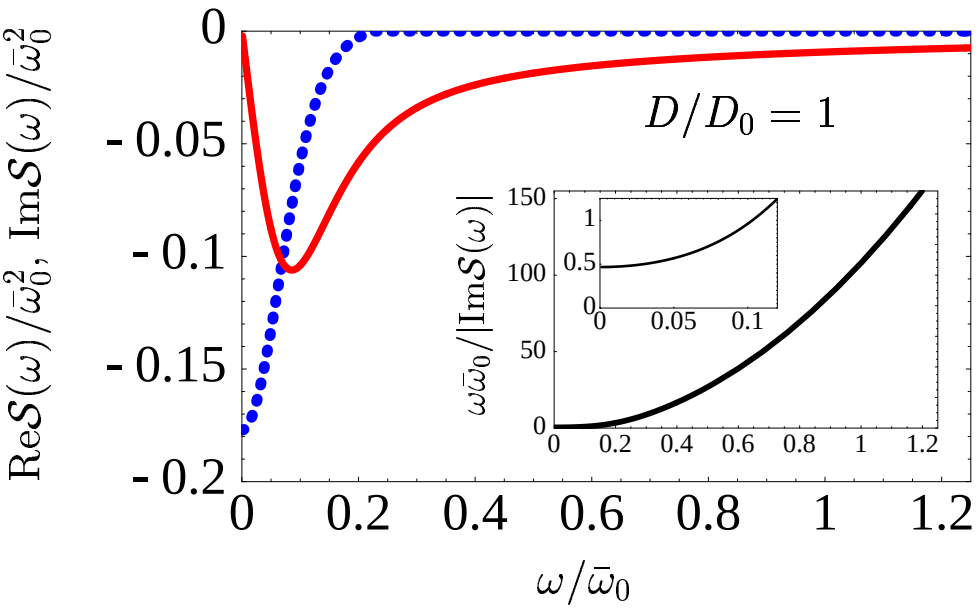

Figure 4.5: Frictional damping term $\mathcal{S}(\omega)$.

Real part (dotted line) and imaginary part (solid line) of $\mathcal{S}(\omega)$ as a function of frequency for a C_{60} molecule on a gold substrate and the particular choice $D/D_0 = 1$. The imaginary part tends toward zero linearly which is illustrated in the inset: the "quality factor" $\omega\bar{\omega}_0/|\mathrm{Im}\mathcal{S}(\omega)|$ tends toward a constant at zero frequency.

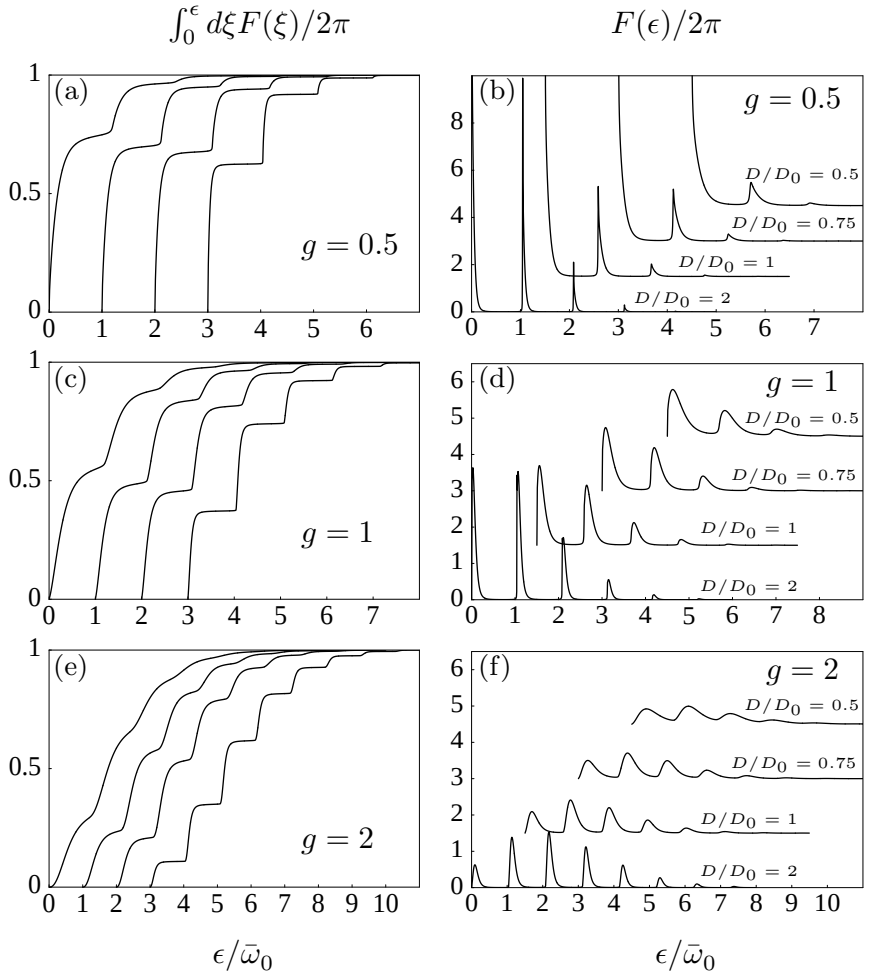

Figure 4.6: The function $F(\xi)$ and its integral for different values of g, making use of Eq. (4.56) for $\mathcal{S}(\omega)$.

The curves have been calculated from Eq. (4.39) at zero temperature, assuming a C_{60} molecule attached to a gold substrate. We take $D/D_0 = 0.5$, 0.75, 1, 2, where g=0.5 in (a) and (b), g=1 in (c) and (d), and g=2 in (e) and (f). The curves have been displaced for clarity by multiples of (1,0) in (a), (c), and (e) (largest D/D_0 to the right), and by multiples of (1.5,1.5) in (b), (d), and (f) (largest D/D_0 at the bottom). The staircases in (a), (c), and (e) feature sharper and less asymmetric steps for larger D/D_0 but are clearly visible in any case. The asymmetry is even more apparent in the plots of F in (b), (d), and (f). In contrast to the constant Q-factor results in Fig. 4.3, even the first step in the staircase gets smeared for smaller D/D_0. However, we recover the large constant-Q limit for large D/D_0.

part remains nonzero over a large frequency range. The latter is important for the damping since the quantity $\omega\bar{\omega}_0/|\mathrm{Im}\mathcal{S}(\omega)|$ takes the place of the quality factor. The fact that this quantity tends toward a constant at zero frequency illustrates that the imaginary part of $\mathcal{S}(\omega)$ rises linearly with ω for small ω.

We plot the results for F and its integral in Fig. 4.6. First we note that the shape of the staircases is markedly different from the constant Q-factor model: they are asymmetric and less steep on the rising side with a rather sharp transition to the next step. The asymmetry is even more obvious in the peaks of F itself. We also note that a larger spread of the coupling over the surface, i.e., larger D/D_0, makes the peaks in F and the steps in its integral sharper and less asymmetric. For large D/D_0, the staircase tends toward the large constant-Q limit of before since then $\omega/|\mathrm{Im}\mathcal{S}(\omega)|$ grows rapidly with ω and at the same time $\mathcal{S}(0) \to 0$.

4.7 I-V Curves

In this section, we show a number of I-V curves based on the F-function using the expression in Eq. (4.23) at zero temperature, both for the case of frequency-independent quality factor and for the substrate model (4.56) for $\mathcal{S}(\omega)$, which were discussed in Sec. 4.6.

In Fig. 4.7, we show I-V characteristics for constant Q=5 and g = 0.5, 1, 2. For this value of Q, the Franck-Condon steps are still visible. If we take even smaller values of Q (not shown) such that the steps disappear, the characteristics are still strongly modified by the electron-phonon coupling in the sense that a gap develops in the I-V curve. Such an effect was recently claimed to be observed in a different type of device [26].

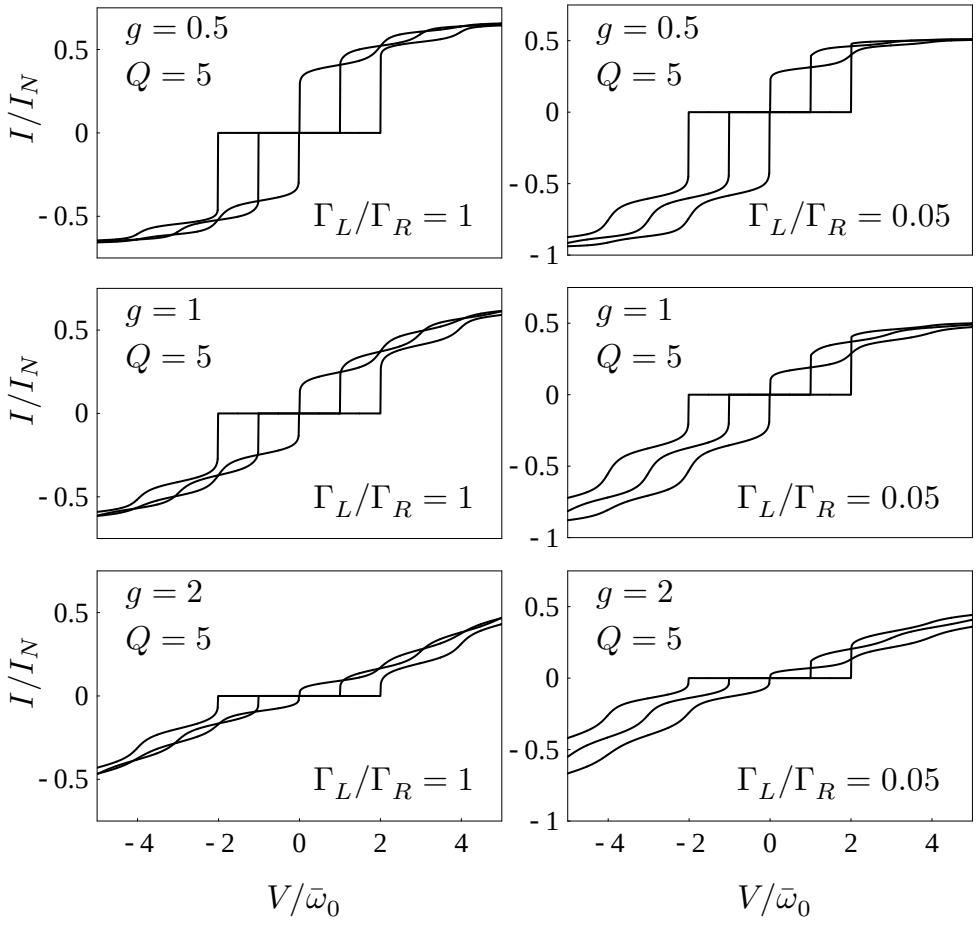

Figure 4.7: I-V characteristics for $g = 0.5$, 1, 2, and frequency-independent $Q = 5$ at zero temperature.

In each panel, we have taken $\varepsilon_0 = 0$, $0.5\omega_0$, and ω_0, and the voltage is applied symmetrically across the device, so that $V_L = V/2 = -V_R$. The current is measured in units of $I_N = e\Gamma_L\Gamma_R/(\Gamma_L + \Gamma_R)$. The panels on the left show the case of symmetric tunneling contacts, whereas the panels on the right side correspond to asymmetric tunneling contacts with $\Gamma_L/\Gamma_R = 0.05$.

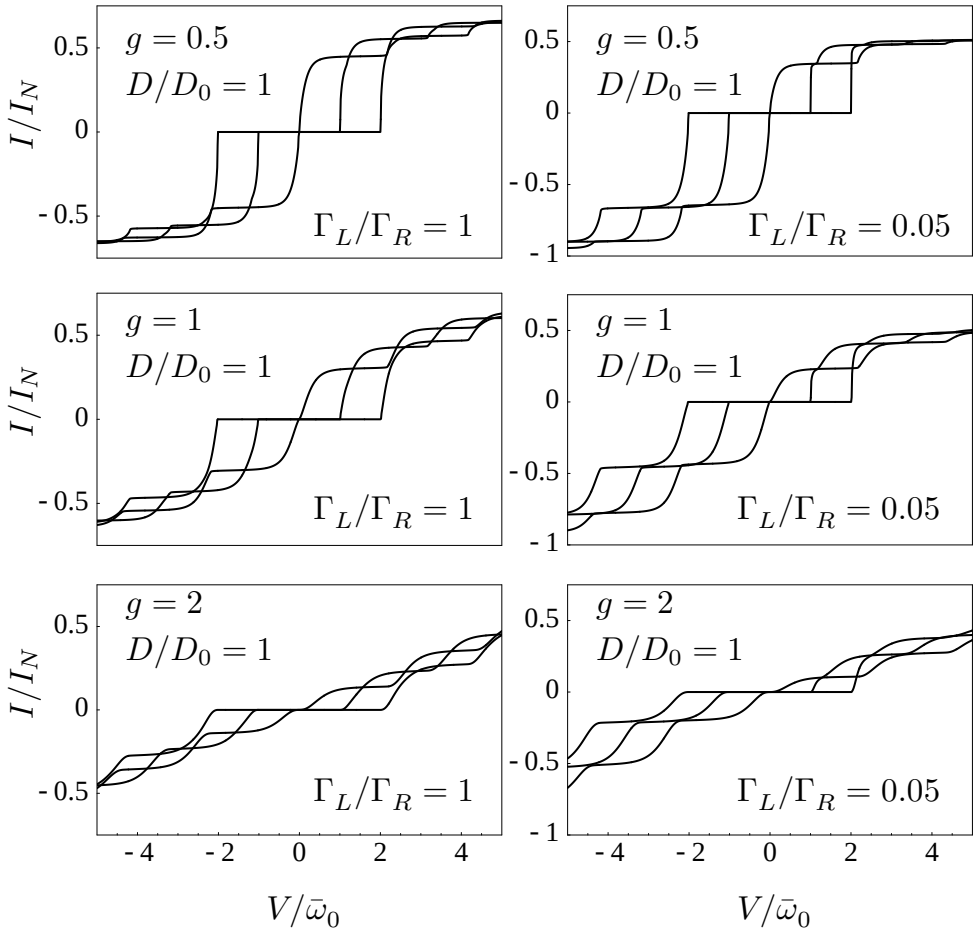

Figure 4.8: I-V characteristics for $g = 0.5$, 1, and 2 using Eq. (4.56) for $\mathcal{S}(\omega)$ at zero temperature, calculated for a C_{60} molecule on gold.

In each panel, we have taken $\varepsilon_0 = 0$, $0.5\omega_0$, and ω_0, and the voltage is applied symmetrically across the device, so that $V_L = V/2 = -V_R$. The current is measured in units of $I_N = e\Gamma_L\Gamma_R/(\Gamma_L + \Gamma_R)$. The panels on the left show the case of symmetric tunneling contacts, whereas the panels on the right side correspond to asymmetric tunneling contacts with $\Gamma_L/\Gamma_R = 0.05$.

We also show I-V curves corresponding to a C_{60} molecule coupled to a gold substrate, using the substrate model of Sec. 4.6.2, see Fig. 4.8. We display the I-V curves for $g = 0.5,\ 1,\ 2$, both for symmetric and for asymmetric tunneling contacts, however, we restrict ourselves to $D/D_0 = 1$ since the general features are very similar for other choices of D/D_0. Upon comparison with the frequency-independent Q-factor model, we note that the I-V staircases are in general less steep and smoother but still clearly exhibit the expected Franck-Condon steps.

4.8 Summary and Discussion

4.8.1 Summary

We have included broadening of the phonon sidebands due to frictional coupling of the oscillator mode within a kinetic-equation approach. Since we have worked in the limit where the tunneling time is much smaller than the lifetime of the oscillator, we have assumed that the oscillator and the environment are in thermal equilibrium, and for this case an analytical result for the current is obtained.

In the reference model featuring the frequency-independent oscillator quality factor Q, we recover the usual Franck-Condon physics for large values of Q. The transition between the two different charge states is then given by the usual overlap of two displaced oscillator wave functions, the governing parameter being the ratio of the displacement length ℓ and the oscillator length ℓ_0, or $g = \ell^2/2\ell_0^2$. For moderate quality factors $Q > Q_c = 2g/\pi$, the steps are smeared but still visible. For even smaller values of the quality factor, the decay time of the oscillations becomes shorter than the quantum mechanical uncertainty time, which happens when $Q < 1/g$. In this strongly damped case the tunneling process crosses over to

a regime with a gap given by the classical displacement energy.

Furthermore, we were able to calculate $\mathcal{S}(\omega)$ for a molecule that is attached to a substrate and showed how the molecule loses energy to the substrate. The model features similar general results as the constant Q-factor model, however, it is different in that the steps in the I-V curves rise more smoothly but feature a rather sharp transition to the next step, which then again rises up smoothly. The underlying reason is the peak structure of F, which exhibits asymmetric peaks due to the frequency-dependent damping coefficient. We also note the dependence on the spread of the coupling over the substrate surface, parameterized by D/D_0, where our results tend toward the large constant-Q limit for large D/D_0.

4.8.2 Comparison with experiments

We have also tried to fit the present theoretical results to the experiments in Ref. [2], for which the theory should be appropriate since the tunneling broadening is much smaller than temperature, oscillator quantum, and observed widths. For these experiments, in which C_{60} molecules were attached to two leads, it therefore seems likely that the broadening is dominated by coupling to the environment.

A rough qualitative agreement, except for the steepness on the rising side of the steps, can be achieved for the frequency-independent quality factor if we assume $g \approx 1-2$ and $Q \approx 2-6$. However, in order to obtain quantitative agreement, it is necessary to assume different values for g and Q for different values of the gate and source-drain voltages.

Our model for $\mathcal{S}(\omega)$ that corresponds to a molecule attached to a substrate, see Sec. 4.6.2, features qualitative agreement with experiment if we assume g and D/D_0 to be on the order of unity. The asymmetry in the peak structure of F

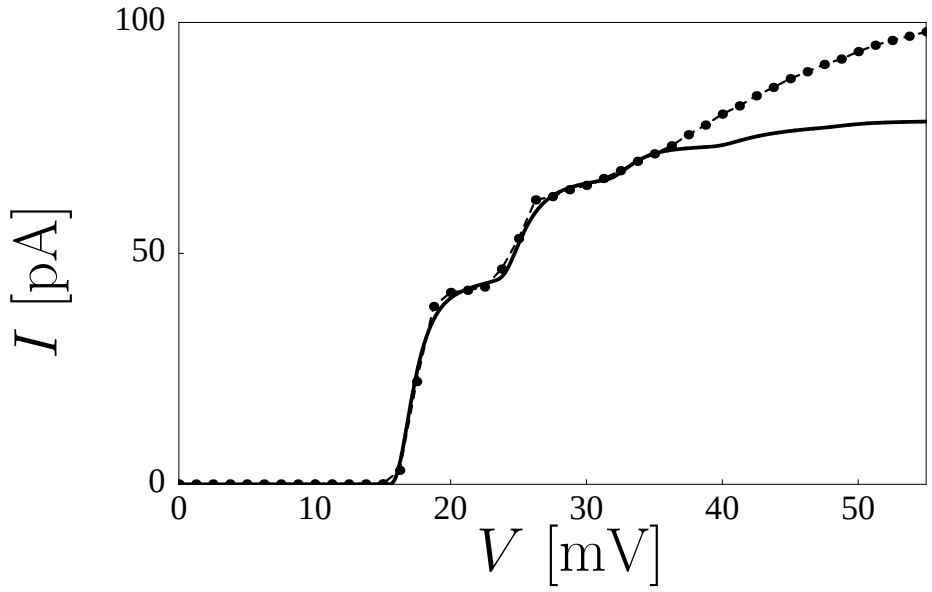

Figure 4.9: Example of a fit to the experimental curves of Ref. [2] using the substrate model (4.56) for a C_{60} molecule on gold, with $g = 2$ and $D/D_0 = 0.75$.

The dots are experimental data points for a gate voltage of 6.8V and positive bias voltage, and the solid line is the theoretical curve. The smearing of the first step is seen to be reproduced well, while at the same time showing a sharp rise for the second step. This kind of smearing could not be produced by thermal smearing, which would smear both steps equally. However, it is not possible to make consistent fits for the entire I-V curve and for different gate voltages. This suggests that the molecule might be changing position and/or coupling with changing voltages.

actually provides for a better quantitative fit to the experimental data than is possible for the constant Q-factor model. This is illustrated in Fig. 4.9.

BIBLIOGRAPHY

[1] M. A. Reed, C. Zhou, C. J. Muller, T. P. Burgin, and J. M. Tour, Science **278**, 252 (1997).

[2] H. Park, J. Park, A. K. L. Lim, E. H. Anderson, A. P. Alivisatos, and P. L. McEuen, Nature **407**, 57 (2000).

[3] J. Park, A. N. Pasupathy, J. I. Goldsmith, C. Chang, Y. Yaish, J. R. Petta, M. Rinkoski, J. P. Sethna, H. D. Abruna, P. L. McEuen, and D. C. Ralph, Nature **417**, 722 (2002).

[4] W. Liang, M. P. Shores, M. Bockrath, J. R. Long, and H. Park, Nature **417**, 725 (2002).

[5] R. H. M. Smit, Y. Noat, C. Untiedt, N. D. Lang, M. C. van Hemert, and J. M. van Ruitenbeek, Nature **419**, 906 (2002).

[6] N. B. Zhitenev, H. Meng, and Z. Bao, Phys. Rev. Lett. **88**, 226801 (2002).

[7] D. Boese and H. Schoeller, Europhys. Lett. **54**, 668 (2001).

[8] K. D. McCarthy, N. Prokof'ev, and M. T. Tuominen, Phys. Rev. B **67**, 245415 (2003).

[9] A. Mitra, I. Aleiner, and A. J. Millis, Phys. Rev. B **69**, 245302 (2004).

[10] V. Aji, J. E. Moore, and C. M. Varma, cond-mat/0302222.

[11] V. L. Gurevich and H. R. Schober, Phys. Rev. B **57**, 11295 (1998).

[12] K. R. Patton and M. R. Geller, Phys. Rev. B **67**, 155418 (2003).

[13] Y. V. Nazarov, Zh. Eksp. Teor. Fiz. **95**, 975 (1989), [Sov. Phys. JETP **68**, 561 (1989)].

[14] M. H. Devoret, D. Esteve, H. Grabert, G.-L. Ingold, H. Pothier, and C. Urbina, Phys. Rev. Lett. **64**, 1824 (1990).

[15] S. M. Girvin, L. I. Glazman, M. Jonson, D. R. Penn, and M. D. Stiles, Phys. Rev. Lett. **64**, 3183 (1990).

[16] G.-L. Ingold and H. Grabert, Europhys. Lett. **14**, 371 (1991).

[17] A. O. Caldeira and A. J. Leggett, Ann. Phys. **149**, 374 (1983).

[18] A. A. Louis and J. P. Sethna, Phys. Rev. Lett. **74**, 1363 (1995).

[19] G. D. Mahan, *Many-Particle Physics*, 2nd ed. (Plenum Press, New York, 1990).

[20] A. Alexandrov and A. Bratkovsky, Phys. Rev. B **67**, 235312 (2003).

[21] P. Minnhagen, Phys. Lett. **56A**, 327 (1976).

[22] H. Ezawa, Ann. Phys. **67**, 438 (1971).

[23] L. D. Landau and E. M. Lifshitz, *Theory of Elasticity* (Pergamon Press, New York, 1959).

[24] W. M. Ewing, W. S. Jardetzky, and F. Press, *Elastic Waves in Layered Media* (McGraw-Hill, New York, 1957).

[25] H. Lamb, Phil. Trans. Roy. Soc. A **203**, 1 (1904).

[26] E. M. Höhberger, R. H. Blick, T. Brandes, J. Kirschbaum, W. Wegscheider, M. Bichler, and J. P. Kotthaus, Phys. Rev. Lett. **92**, 046804 (2004).

Chapter 5

Dissipative Tunneling and Orthogonality Catastrophe in Molecular Transistors

5.1 Introduction

The possibility of creating devices on a molecular level has opened up the field of single-molecule electronics in recent years. The transport properties of such mesoscopic systems have been investigated in numerous experiments [1, 2, 3, 4, 5, 6, 7, 8]. Of particular interest has been the influence of strong electron-phonon coupling on electron transport [2, 3, 6], which manifests itself as emission and absorption of vibrational quanta observable in the excitation spectra. One example is the series of experiments by Park *et al.* [2] where it was shown that the current through a single C_{60} molecule was strongly coupled to a single vibrational mode.

A large number of theoretical works has dealt with the problem of tunneling through a single molecular electronic level that is coupled to phonon modes. Since in many experimental realizations the tunnel coupling of the molecule to the leads is rather weak compared to the other energy scales in the problem, transport is dominated by Coulomb-blockade effects and occurs sequentially. An approach based on rate equations can thus be justified and has been used in a number of recent papers [9, 10, 11, 12]. Physically, it is an essential question how the excited vibrational levels are allowed to relax, either through coupling to the environment, for example the phonons or plasmons of the metal substrate, or by virtue of the tunneling electrons [13, 14, 15]. In the case where the relaxation of the vibrational modes is faster than the tunneling rate one can assume an equilibrium phonon distribution.

The coupling between the vibrational mode of the molecule and the environment depends strongly on which vibrational mode is considered. For intramolecular vibrations the lifetime can be very long [16, 17]. However, we were able to show in Chapter 4 that the vibrational mode associated with the center-of-mass motion of the molecule is coupled more strongly to the environment and is thus exposed to an effective damping mechanism. The electron-phonon effects seen in the experiments of Ref. [2] are suggested to be due to such a center-of-mass motion.

In this chapter, we investigate how screening of the charge on the molecule influences the damping mechanism. A sketch of the physical setup that serves as starting point is shown in Fig. 5.1. If the molecule is not charged, it is held in place by an interaction of the van der Waals type. It can perform center-of-mass oscillations about its equilibrium position, and the characteristic energy $\hbar\omega$ of such an oscillation was found to be $\sim$ 5meV [2]. These oscillations also influence the

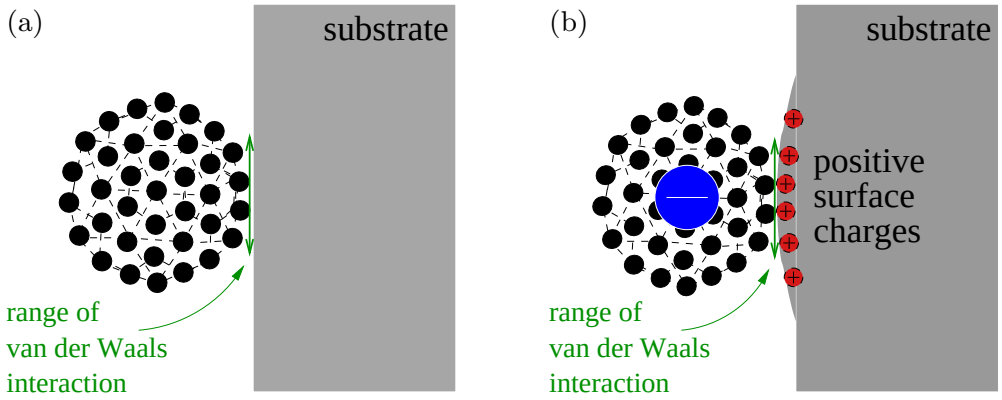

Figure 5.1: Illustration of the molecule attached to a substrate.

(a) The molecule is attached to a substrate, for instance by van der Waals interactions. The molecule can perform center-of-mass oscillations about its equilibrium position, which also exerts forces on the substrate. We label this interaction the *van der Waals* interaction in the following, and we focus on the linear regime where the interaction strength is independent of the position of the molecule. **(b)** When an electron hops onto the molecule, the force created by induced surface charges causes a shift of the equilibrium position of the oscillator and of the vibrational modes of the substrate. For a pointlike charge on the molecule, the shift of the equilibrium positions takes place in an effective dipole field (multipole field for non-pointlike charges). We label this interaction the *electrostatic* interaction.

substrate to which the molecule is attached, and we will call this interaction the *van der Waals* interaction in the following. On the other hand, if the molecule is charged, there will be additional electric forces on the molecule, which are either due to static electric charges on the surface, e.g., as a result of impurities, or due to surface charges in the substrate that are induced by the charge on the molecule. Hence, when an electron tunnels onto the molecule, this leads not only to a force on the molecule itself but also to electrostatic forces on the substrate to which it is attached, and the equilibrium positions of the vibrational modes in the substrate are shifted accordingly. In the following, we will focus on the case of surface charges only, but static impurity charges can be treated analogously and have the very same qualitative effect. We will refer to this type of interaction as the *electrostatic* interaction.[1]

Under the influence of the Coulomb interaction, the surface is attracted to the molecule (and vice versa), and substrate atoms will be shifted away from their equilibrium positions until van der Waals forces and electrostatic forces are in equilibrium. This shift, however, occurs in an effective dipole field (or multipole field for charges that are not pointlike) since the field between molecule and substrate due to the additional charge on the molecule is equivalent to the case without surface charges but an image charge located inside the substrate, see Fig. 5.2. Only in the limit of a very short-ranged van der Waals interaction compared to the separation of charge and image charge could we approximate the electric field at

[1]In fact, the electrostatic interaction changes with the displacement of the molecule x_0 from its equilibrium position ($\sim$ width of the molecule D_0 away from the substrate). To linear order, we can Taylor expand, so that the strength of the position-dependent force is smaller than the equilibrium electrostatic interaction by a factor x_0/D_0. Compared to van der Waals and electrostatic interaction, which have to be equal in equilibrium, the position dependence can thus be neglected.

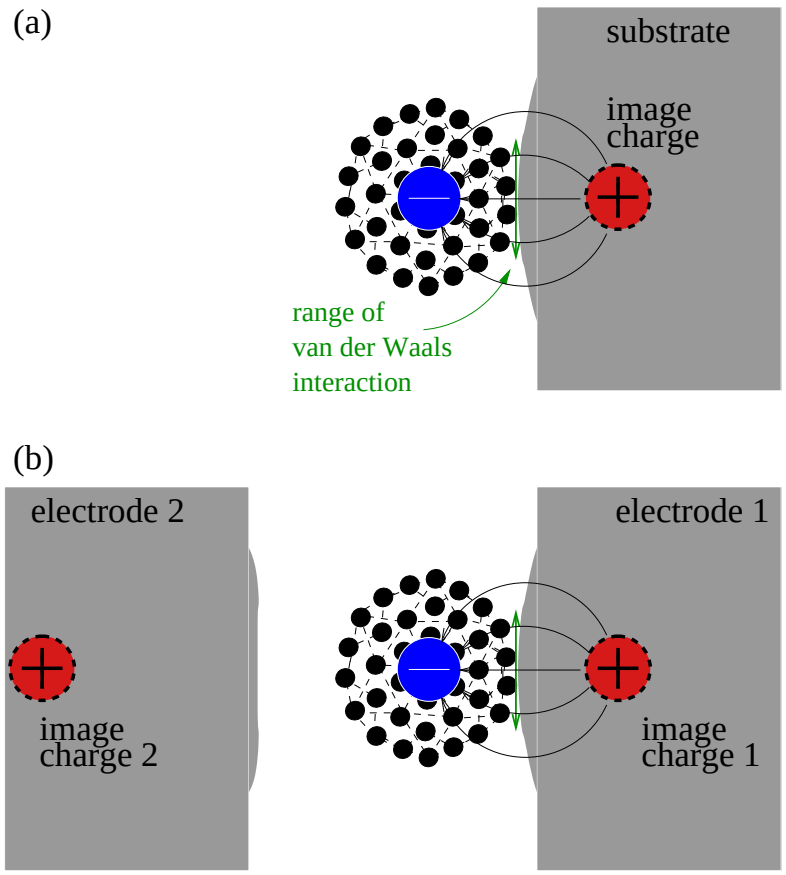

Figure 5.2: Electric fields induced by a charge on the molecule.

(a) Outside the substrate, the electric field between the charged molecule and the substrate is equivalent to the case of an image charge located inside the substrate and no surface charges. The shift of the equilibrium positions of the vibrational modes of the substrate can thus be understood to occur in an effective dipole field for pointlike charges (multipole field in general). Since the shift of the equilibrium positions then has an integrable long-range part (see text), the small-frequency part of the phonon spectrum is not shifted, and thus there will be no orthogonality catastrophe associated with the tunneling process. The situation is different in **(b)**, where the molecule interacts with image charges in both electrodes. If the two electrodes can be considered as mechanically independent, there will be long-range components of the displacement fields (the second electrode can be thought of as an external influence), and orthogonality is restored.

the surface as constant, and thus monopolar. Such a mismatch of length scales is rather unlikely for a situation as depicted in Figs. 5.1 and 5.2(a). However, a different experimental geometry as in Fig. 5.2(b) can introduce monopolar effects, see Chapter 4.

The shift of the equilibrium positions $\mathbf{a_k}$ for each phonon mode $\mathbf{k}$ can be calculated by resorting to the dynamical matrix $\mathbf{D}(\mathbf{k}, \mathbf{k}')$ which appears in the harmonic expansion of the Hamiltonian (see also Ref. [18]),

$$H_{\text{harm}} = \frac{1}{2} \sum_{\mathbf{k}\,\mathbf{k}'} \mathbf{a_k} \mathbf{D}(\mathbf{k}, \mathbf{k}') \mathbf{a_{k'}}. \tag{5.1}$$

If we denote the electrostatic force on the substrate as $\mathbf{G}(\mathbf{r})$ and choose a phonon eigenmode basis such that $\mathbf{D}(\mathbf{k}, \mathbf{k}')$ is diagonal, we can see that force equilibrium demands

$$\mathbf{D}(\mathbf{k}) \mathbf{a_k} \sim \sum_{\mathbf{r}} \mathbf{G}(\mathbf{r}) e^{i\mathbf{kr}}, \tag{5.2}$$

where the right-hand side is the Fourier component of the force $\mathbf{G}(\mathbf{r})$ acting on the plane-wave phonon state $\mathbf{k}$. The long-wavelength behavior can give rise to a version of orthogonality catastrophe, i.e., zero overlap between the ground states corresponding to the shifted and unshifted equilibrium positions. For small wave vectors k, we know that $\mathbf{D}(k) \sim k^2$, see Ref. [19]. Expanding $\mathbf{G}(\mathbf{r})$ in a multipole expansion, and expanding the exponential for small k, we can see that $\mathrm{a}_{\mathbf{k}} \sim k^{-1}$ for a dipole force since the volume integral of any multipole field is zero by definition [20], whereas $\mathrm{a}_{\mathbf{k}} \sim k^{-2}$ for a monopole field since this corresponds to the constant part in the multipole expansion. This difference in long-wavelength behavior gives rise to nonzero (dipole) or zero (monopole) overlap between the ground states in three dimensions, as one can see from the following simple argument. Let η be the ground-state overlap between a set of harmonic quantum oscillators and

its shifted counterparts, then

$$\eta \sim \exp\left(-\sum_{\mathbf{k}} \mathbf{a}_{\mathbf{k}}^2/2\ell_{\mathbf{k}}^2\right), \tag{5.3}$$

where $\ell_{\mathbf{k}}^2 = \hbar/m_{\mathbf{k}}\omega_{\mathbf{k}}$ is the oscillator quantum with $\ell_{\mathbf{k}}^2 \sim k^{-1}$ for small k. Converting the sum to an integration, we see that the question of zero or nonzero overlap is decided by both dimensionality and the small-k behavior of the equilibrium shifts $\mathbf{a}_{\mathbf{k}}$. In particular,

$$\eta \sim \exp\left(-\int \mathrm{d}k\, k^d \mathbf{a}_{\mathbf{k}}^2/A\right), \tag{5.4}$$

where d is the dimensionality, and A is a normalization factor. Thus, in one dimension, we encounter orthogonality catastrophe for both monopolar and dipolar shifts, whereas in two and three dimensions we see that dipolar equilibrium shifts feature nonzero overlap!

It is this effect that we investigate in this chapter in the context of how a single vibrational mode of the molecule dissipates energy into a phononic environment. Again referring to Fig. 5.2, if the range of the van der Waals interaction D is comparable to the dipole length scale (set by the separation of charge and image charge), we expect nonzero overlap between the two ground states in accord with a dipolar equilibrium shift, and we should thus see a step in the I-V characteristics, see Fig. 5.3. If, on the other hand, the van der Waals range is very small compared to the dipole length scale, we expect orthogonality catastrophe corresponding to the approximately constant (monopolar) force. The latter can also occur for particular geometries, see Fig. 5.2(b). The current then behaves according to a power law at the onset of conduction, see Chapter 4.

Another way of looking at the same problem is in terms of translational invariance. Suppose that the van der Waals range D and the dipole length scale are

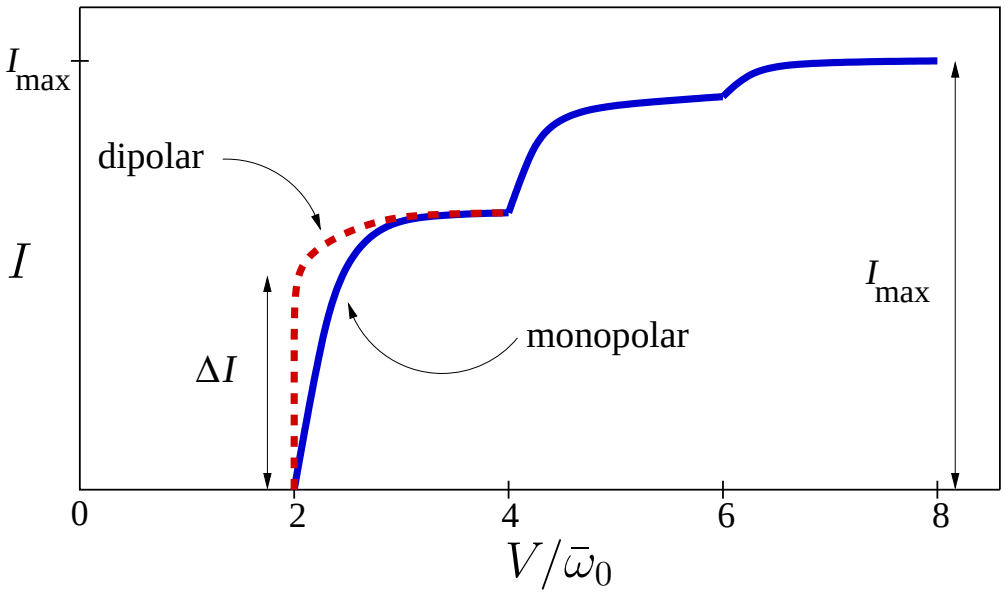

Figure 5.3: Sketch of the difference between dipolar (dashed line) and monopolar case (solid line) in the I-V characteristics.

We depict the situation for ε_0=$2\bar{\omega}_0$ and $V_L = V/2 = -V_R$ in the notation of Secs. 5.2, 5.3, and 5.4. The dipolar curve features a finite step of size ΔI at the onset of conduction, whereas the monopolar curve rises according to a power law.

comparable to each other. In this case, we could think of drawing a box around the whole system which contains both the van der Waals and the electrostatic interaction. Hence, all forces are internal, and we have a translationally invariant Hamiltonian. Small D, on the other hand, corresponds to the case that, from the point of view of the van der Waals interaction, the electrostatic interaction is extremely extended and spread out. Therefore, the electrostatic force acts approximately as an *external* force as far as the van der Waals interaction is concerned and translational invariance is broken. This case can be recovered in a physical setup where the molecule is located asymmetrically in between two substrates, see Fig. 5.2(b). Then, image charges in the substrate farther away can approximately have the effect of an external force on the substrate closer to the molecule.

The chapter is organized as follows. The model Hamiltonian is defined in Sec. 5.2, and in Sec. 5.3 we recapitulate the expression for the current derived on the basis of rate equations in Chapter 4. The function that describes the tunneling density of states is then solved in the case of equal spread of van der Waals and electrostatic interaction in the presence of the dissipative environment in Sec. 5.4. Finally, a discussion and summary of the results can be found in Sec. 5.5.

5.2 Model Hamiltonian

We consider a model of one single spin-degenerate molecular level coupled to two leads. The single level is coupled to the vibrational mode of the molecule through the charge on the molecule, as are the vibrational modes of the substrate. The coupling between the oscillator and the environment is included as a linear coupling to a bath of harmonic oscillators. Similar to the model studied in Chapter 4, the

model Hamiltonian then reads

$$H = H_{LR} + H_D + H_B + H_{\text{bath}} + H_{DB} + H_{D\text{bath}} + H_{B\text{bath}} + H_T, \tag{5.5}$$

with

$$H_{LR} = \sum_{k\sigma,\,\alpha=L,R} \xi_{k\alpha} c^\dagger_{k\sigma,\alpha} c_{k\sigma,\alpha}, \tag{5.6a}$$

$$H_D = \sum_\sigma \xi_0 d^\dagger_\sigma d_\sigma + U n_{d\uparrow} n_{d\downarrow}, \tag{5.6b}$$

$$H_{\text{B}} = \frac{p_0^2}{2m_0} + \frac{1}{2} m_0 \omega_0^2 x_0^2, \tag{5.6c}$$

$$H_{DB} = \lambda x_0 \sum_\sigma d^\dagger_\sigma d_\sigma, \tag{5.6d}$$

$$H_{\text{bath}} = \sum_j \left(\frac{p_j^2}{2m_j} + \frac{1}{2} m_j \omega_j^2 x_j^2 \right), \tag{5.6e}$$

$$H_{B\text{bath}} = \sum_j \beta_j x_j x_0, \tag{5.6f}$$

$$H_T = \sum_{k\sigma,\,\alpha=L,R} t_{k\alpha} c^\dagger_{k\sigma,\alpha} d_\sigma + h.c. \tag{5.6g}$$

where the $c^\dagger_{k\sigma,\alpha}$, $c_{k\sigma,\alpha}$ and the $d^\dagger_\sigma$, d_σ are creation and annihilation operators for the leads and the molecule, respectively, x_0 is the oscillator degree of freedom, $\{x_j\}$ describes the set of environmental degrees of freedom and m_j, ω_j their respective masses and frequencies, ξ_0 is the on-site energy, and U is the energy cost for having double electron occupancy on the molecule. The coupling constants for the electron-oscillator interaction and the oscillator-bath interaction are λ and $\{\beta_j\}$, respectively. The lead electron energies are given by

$$\xi_{k\alpha} = \varepsilon_{k\alpha} - \mu_\alpha, \tag{5.7}$$

where $\varepsilon_{k\alpha}$ is the energy of electron state k in lead α, and μ_α is the chemical potential of lead α. The tunneling amplitudes $t_{k\alpha}$ in the tunneling term H_T could

in principle also depend on the oscillator position, which should be a small effect for the experimental realizations in Refs. [2] and [3], see also Chapter 4.

We can explicitly write down how the β_j are connected to the displacement $u(\mathbf{r})$ perpendicular to the substrate if we assume that the force acting between the molecular vibrational mode and the substrate phonons is spread over the substrate according to a normalized distribution $f(\mathbf{r})$, i.e., $\int \mathrm{d}\mathbf{r} f(\mathbf{r}) = 1$. If we model the interaction as a harmonic spring potential, we can write

$$H_{\mathrm{int}} = \frac{1}{2} m_0 \omega_0^2 \left[x_0 - \int \mathrm{d}\mathbf{r} f(\mathbf{r}) u(\mathbf{r}) \right]^2 . \tag{5.8}$$

Expanding the square, we can combine the term $\frac{1}{2} m_0 \omega_0^2 \left[\int \mathrm{d}\mathbf{r} f(\mathbf{r}) u(\mathbf{r}) \right]^2$ with the part of the Hamiltonian that describes the "free" environmental bath and diagonalize the combination by introducing new coordinates x_j. These are related to $u(\mathbf{r})$ by a unitary transformation as

$$u(\mathbf{r}) = \sum_j c_j(\mathbf{r}) x_j, \tag{5.9}$$

with appropriately chosen coefficient functions $c_j(\mathbf{r})$. Defining

$$\beta_j \equiv -m_0 \omega_0^2 \int \mathrm{d}\mathbf{r} f(\mathbf{r}) c_j(\mathbf{r}), \tag{5.10}$$

we immediately see that we recover the structure of our original Hamiltonian H. The advantage of the form of H_{int} is that its translational invariance with respect to shifting both x_0 and $u(\mathbf{r})$ by the same constant displacement is immediately apparent since the distribution function $f(\mathbf{r})$ is normalized to 1.

The difference to Chapter 4 is the newly included coupling term $H_{D\mathrm{bath}}$ between the charge on the molecule and the bath of vibrational modes,

$$H_{D\mathrm{bath}} = \sum_j \lambda_j x_j \sum_\sigma d_\sigma^\dagger d_\sigma. \tag{5.11}$$

It is again instructive to rewrite this term as a function of $u(\mathbf{r})$ and a normalized distribution function $g(\mathbf{r})$ that characterizes the form and range of the electrostatic interaction between molecule and substrate:

$$H_{D\text{bath}} = -\lambda \int \mathrm{d}\mathbf{r} g(\mathbf{r}) u(\mathbf{r}) \sum_{\sigma} d_{\sigma}^{\dagger} d_{\sigma}, \tag{5.12}$$

so that the electrostatic force on the substrate $\mathbf{G}(\mathbf{r})$ mentioned in Sec. 5.1 has the form $\mathbf{G}(\mathbf{r}) = \lambda g(\mathbf{r}) \sum_{\sigma} d_{\sigma}^{\dagger} d_{\sigma}$. Since $u(\mathbf{r})$ can be written as a linear superposition of the eigenmodes x_j, see Eq. (5.9), we can express the coupling constants λ_j in terms of the distribution function $g(\mathbf{r})$ as

$$\lambda_j = -\lambda \int \mathrm{d}\mathbf{r} g(\mathbf{r}) c_j(\mathbf{r}). \tag{5.13}$$

Given Eq. (5.12), translational invariance of the total Hamiltonian with respect to shifting both x_0 and $u(\mathbf{r})$ by some constant displacement vector is ensured automatically if $g(\mathbf{r})$ is normalized properly, i.e., if $\int \mathrm{d}\mathbf{r} g(\mathbf{r}) = 1$.

We now want to relate the coupling constants in the boson-bath coupling to the finite damping of the vibrational mode, which can be accomplished by studying the classical equations of motion. After removing the bath degrees of freedom, we end up with the following equation of motion in the frequency domain, neglecting the coupling terms H_{DB} and $H_{D\text{bath}}$ that will be removed by a unitary transformation below:

$$[\omega^2 - \omega_0^2 - \mathcal{S}(\omega)] x_0(\omega) = 0, \tag{5.14}$$

where we have defined

$$\mathcal{S}(\omega) = \frac{1}{m_0} \sum_j \frac{\beta_j^2}{m_j} \frac{1}{(\omega + i\eta)^2 - \omega_j^2}, \tag{5.15}$$

which is complex in general and gives rise to frictional damping and a frequency shift of the bare frequency ω_0. In Chapter 4, we explicitly calculated $\mathcal{S}(\omega)$ for the

case of a molecule attached to a semi-infinite substrate. We will use these results throughout this chapter, again assuming that the van der Waals force $\mathcal{F}$ exerted by the molecule, see Fig. 5.1(a), is directed perpendicular to the substrate surface and is cylindrically symmetric. Also, we assume that both the van der Waals force and the electrostatic force only couple to the substrate surface, i.e., $g(\mathbf{r}), f(\mathbf{r}) \sim \delta(x)$, where the x axis is perpendicular to the substrate surface. The van der Waals force $\mathcal{F}$ on the molecule is thus understood to be of the form

$$\mathcal{F} = -m_0\omega_0^2 \left[x_0 - \int_0^\infty 2\pi r f(r) u_x(r) dr \right], \tag{5.16}$$

where $u_x(r)$ is the perpendicular displacement on the surface of the substrate, and r is the radial direction in the surface plane. For explicit numerical evaluations later in this chapter, we will use $f(r) = e^{-r/D}/2\pi D^2$ just as in Chapter 4, with D on the order of the width D_0 of the molecule.

We now eliminate the coupling terms H_{DB} and $H_{D\mathrm{bath}}$ of the Hamiltonian (5.5) by a unitary transformation similar to the one used in the independent boson model [21], at the cost of introducing displacement operators in the tunneling term. However, since we have a somewhat more complicated system here due to the coupling to the bosonic bath, the unitary transformation in Ref. [21] has to be generalized. We define the transformation

$$\tilde{H} = SHS^\dagger, \quad S = e^{-iAn_d}, \quad A = p_0\ell + \sum_j p_j \ell_j, \tag{5.17}$$

where $n_d = \sum_\sigma d_\sigma^\dagger d_\sigma$. Using that

$$\tilde{x}_0 = x_0 - \ell n_d, \quad \tilde{x}_j = x_j - \ell_j n_d, \tag{5.18}$$

both linear coupling terms, H_{DB} and $H_{D\mathrm{bath}}$, cancel if we set

$$\ell = \frac{\lambda - \sum_j \frac{\beta_j \lambda_j}{m_j\omega_j^2}}{m_0[\omega_0^2 + \mathcal{S}(0)]}, \qquad \ell_j = \frac{\lambda_j}{m_j\omega_j^2} - \frac{\ell\beta_j}{m_j\omega_j^2}. \tag{5.19}$$

The Hamiltonian then transforms into

$$\tilde{H} = H_{LR} + \tilde{H}_D + H_B + H_{\text{bath}} + H_{B\text{bath}} + \tilde{H}_T, \tag{5.20}$$

where

$$\tilde{H}_T = \sum_{k\sigma,\,\alpha=L,R} t_{k\sigma,\alpha} \left(c^\dagger_{k\sigma,\alpha} e^{iA} d_\sigma + d^\dagger_\sigma e^{-iA} c_{k\sigma,\alpha} \right) \tag{5.21}$$

and

$$\tilde{H}_D = \varepsilon_0 \sum_\sigma d^\dagger_\sigma d_\sigma + \tilde{U} n_{d\downarrow} n_{d\uparrow}. \tag{5.22}$$

Here we have defined

$$\tilde{U} \equiv U - \frac{\kappa}{m_0[\omega_0^2 + \mathcal{S}(0)]},\ \varepsilon_0 \equiv \xi_0 - \frac{1}{2}\frac{\kappa}{m_0[\omega_0^2 + \mathcal{S}(0)]}, \tag{5.23}$$

where

$$\kappa \equiv \frac{1}{2}\lambda^2 + \frac{1}{2}\sum_j \frac{\lambda_j^2}{m_j\omega_j^2}\left(1 - \sum_{i\neq j}\frac{\beta_i^2}{m_i\omega_i^2}\right) - \sum_j \frac{\beta_j\lambda_j}{m_j\omega_j^2}\left(\lambda - \sum_{i>j}\frac{\beta_i\lambda_i}{m_i\omega_i^2}\right). \tag{5.24}$$

Thus, the Coulomb repulsion U is modified by both the phonon mediated interaction and the electrostatic interaction between molecule and substrate.

It is important to note that for the particular choice $f(\mathbf{r}) = g(\mathbf{r})$, i.e., when the distribution functions of electrostatic and van der Waals interaction are equal, we obtain from Eqs. (5.10) and (5.13):

$$\lambda_j = \frac{\lambda\beta_j}{m_0\omega_0^2}, \qquad \ell = \frac{\lambda}{m_0\omega_0^2}, \qquad \ell_j = 0. \tag{5.25}$$

Furthermore, we can quantify the deviation of $f(\mathbf{r})$ from $g(\mathbf{r})$ by defining

$$\epsilon(\mathbf{r}) \equiv g(\mathbf{r}) - f(\mathbf{r}), \quad \epsilon_j \equiv -m_0\omega_0^2 \int \mathrm{d}\mathbf{r}\epsilon(\mathbf{r})c_j(\mathbf{r}), \tag{5.26}$$

where $\int \mathrm{d}\mathbf{r}\epsilon(\mathbf{r}) = 0$. We can thus rewrite λ_j as

$$\lambda_j = \frac{\lambda}{m_0\omega_0^2}\left(\beta_j + \epsilon_j\right). \tag{5.27}$$

This immediately leads to

$$\ell = \frac{\lambda}{m_0\omega_0^2}\left[1-\Delta(0)\right],\ \ell_j = \frac{\ell}{m_j\omega_j^2}\frac{\epsilon_j+\Delta(0)\beta_j}{1-\Delta(0)}, \tag{5.28}$$

where we defined

$$\Delta(\omega) \equiv -\frac{1}{m_0\bar{\omega}_0^2}\sum_n \frac{\beta_n\epsilon_n}{m_n}\frac{1}{(\omega+i\eta)^2-\omega_n^2}. \tag{5.29}$$

If the two distribution functions $f(\mathbf{r})$ and $g(\mathbf{r})$ deviate only slightly from each other, ϵ_j is small compared to β_j, and we see that $\Delta(\omega) \ll 1$. Also note that the qualitative frequency dependence of $\Delta(\omega)$ is exactly the same as that of $\mathcal{S}(\omega)$.

5.3 Current Formula

As mentioned in Sec. 5.1, the most important assumption here is that the tunneling rate is much smaller than all other time scales, which means that we can assume the vibrational degrees of freedom and the Fermi seas in the two electrodes to be in equilibrium at all times. For simplicity, we consider only two charge states and therefore let $U = \infty$, which leaves us with only three states playing a role in the rate equations: empty, and occupied by either spin up or down. Treating the tunneling term H_T as a perturbation and accordingly employing Fermi's Golden Rule for the tunneling rates, the current I through the molecule is given by

$$I = 2e\frac{\Gamma_{10}^R\Gamma_{01}^L - \Gamma_{01}^R\Gamma_{10}^L}{(\Gamma_{01}^L+\Gamma_{01}^R)+2(\Gamma_{10}^L+\Gamma_{10}^R)}. \tag{5.30}$$

Here we have defined Γ_{ij}^α as the tunneling rate through lead α for tunneling from the state with occupation i to the state with occupation j (see for instance Ref. [22]):

$$\Gamma_{10}^{\alpha} = \Gamma_{\alpha} \int \frac{d\omega}{2\pi} F(\omega) n_{\alpha}(\varepsilon_0 + \omega), \tag{5.31a}$$

$$\Gamma_{01}^{\alpha} = \Gamma_{\alpha} \int \frac{d\omega}{2\pi} F(-\omega)(1 - n_{\alpha}(\varepsilon_0 + \omega)), \tag{5.31b}$$

with

$$F(\omega) = \int_{-\infty}^{\infty} dt\, F(t), \;\; F(t) = \langle e^{iA(t)} e^{-iA} \rangle, \tag{5.32}$$

where the operator A is defined in Eq. (5.17). Furthermore, we work in the wide-band limit with bare tunneling rates $\Gamma_{\alpha}{=}2\pi \sum_k |t_{k\alpha}|^2 \delta(\xi_k)$, and we introduced the Fermi distributions of the two leads $n_{\alpha}(\varepsilon){=}(e^{\beta(\varepsilon - eV_{\alpha})} + 1)^{-1}$.

5.4 Influence of the Coupling to the Environment

In the presence of coupling to the environment, the evaluation of the function $F(t)$ in Eq. (5.32) is in principle straightforward since the Hamiltonian is quadratic in the oscillator and bath degrees of freedom. We obtain

$$F(t) = \exp\left(B(t) - B(0)\right), \quad B(t) = \langle A(t) A(0) \rangle_0, \tag{5.33}$$

where the operator A is defined in Eqs. (5.17) and (5.19). The expectation value $\langle \ldots \rangle_0$ is to be evaluated with respect to $\tilde{H}$ without the tunneling term. We follow the same procedure as in Chapter 4 and use the fluctuation-dissipation theorem,

$$B(\omega) = -2\, \mathrm{Im}[B^R(\omega)](1 + n_B(\omega)), \tag{5.34}$$

to express $B(t)$ in terms of the corresponding retarded Green's function

$$B^R(t) = -i\theta(t) \langle [A(t), A(0)] \rangle_0. \tag{5.35}$$

Here, $n_B(\omega) = (e^{\beta\omega} - 1)^{-1}$ is the usual Bose function. We obtain

$$\begin{aligned} B^R(\omega) = &\ell^2 m_0 \left(\frac{\omega^2}{\omega^2 - \bar{\omega}_0^2 - \bar{\mathcal{S}}(\omega)} - 1 \right) + 2 \frac{\ell^2 m_0}{1 - \Delta(0)} \frac{\Delta(0)\bar{\mathcal{S}}(\omega) - \bar{\omega}_0^2 \bar{\Delta}(\omega)}{\omega^2 - \bar{\omega}_0^2 - \bar{\mathcal{S}}(\omega)} \\ &+ \frac{\ell^2 m_0}{[1 - \Delta(0)]^2} \left[\Delta(0)^2 \bar{\mathcal{S}}(\omega) - 2\Delta(0)\bar{\Delta}(\omega) \right] \\ &+ \frac{\ell^2 m_0}{[1 - \Delta(0)]^2} \sum_j \frac{\epsilon_j^2}{m_j \omega_j^2} \frac{1}{(\omega + i\eta)^2 - \omega_j^2} \\ &+ \frac{\ell^2 m_0}{\omega^2 [1 - \Delta(0)]^2} \frac{[\Delta(0)\bar{\mathcal{S}}(\omega) - \bar{\omega}_0^2 \bar{\Delta}(\omega)]^2}{\omega^2 - \bar{\omega}_0^2 - \bar{\mathcal{S}}(\omega)}, \end{aligned} \tag{5.36}$$

where we have defined $\bar{\mathcal{S}}(\omega) \equiv \mathcal{S}(\omega) - \mathcal{S}(0)$, $\bar{\Delta}(\omega) \equiv \Delta(\omega) - \Delta(0)$, and the experimentally observable renormalized frequency $\bar{\omega}_0^2 \equiv \omega_0^2 + \mathcal{S}(0)$.

If we choose a very wide-ranged distribution $g(\mathbf{r})$ as compared to $f(\mathbf{r})$, then the function $\epsilon(\mathbf{r})$ will be close to $-f(\mathbf{r})$, see Eq. (5.26). This leads to $\epsilon_j \approx -\beta_j$, and upon insertion into Eq. (5.28) we recover the expressions for ℓ and ℓ_j that we found in Chapter 4 since then $\Delta(\omega) \approx \mathcal{S}(\omega)$. In effect, the electrostatic interaction is thus so widespread compared to the van der Waals interaction that it can be considered as an external influence on the system. In this case, we are justified to neglect the term $H_{D\text{bath}}$ in our Hamiltonian altogether since translational invariance is broken by this external force. It is a matter of straightforward algebra to show that $B^R(\omega)$ indeed reduces to the same expression as in Chapter 4.

If, on the other hand, the spread of the two interactions over the surface is comparable to each other, i.e., $g(\mathbf{r}) \approx f(\mathbf{r})$, we have the situation where $\epsilon_j \ll \beta_j$ and $\Delta(\omega) \ll 1$ in Eq. (5.28). The first term in Eq. (5.36) is of zeroth order in ϵ_j, the second term is of first order, and all the remaining terms are of second order. Furthermore, it is important to see that the imaginary part of all terms except of the last one are convergent for small ω since the small-frequency dependence of $\mathrm{Im}\bar{\Delta}(\omega)$ is identical to that of $\mathrm{Im}\bar{\mathcal{S}}(\omega) \sim \omega$. However, the last term is of second order in ϵ_j, so that to leading order, $\mathrm{Im}B^R(\omega)$ is convergent for small ω if the

distribution functions $f(\mathbf{r})$ and $g(\mathbf{r})$ feature comparable ranges.

How small the ϵ_j really have to be in comparison to the β_j (i.e., how similar in range $f(\mathbf{r})$ and $g(\mathbf{r})$ have to be) in order for such a first-order expansion to make sense can be deduced from the following argument: by virtue of Chapter 4, we know that the divergent terms in $\mathrm{Im}B^R(\omega)$ for small ω behave like C/ω, where C is a numerical constant of second order in the ϵ_j. The divergence shows its predominant influence in the large-time behavior of $F(t)$,

$$F(t) = \exp\left(\int_{-\infty}^{\infty} \frac{d\omega}{2\pi}(e^{-i\omega t} - 1)B(\omega)\right). \tag{5.37}$$

For large times t, the integral in the exponent diverges logarithmically, where the physical cutoff for the integration is given by the smallest frequency of the phonon spectrum $\omega_{\min} \ll \bar{\omega}_0$.[2] In order for a first-order expansion in the ϵ_j to hold, we therefore have to demand that the following be true:

$$\ln\left[\frac{\bar{\omega}_0}{\omega_{\min}}\right]|C| \ll 1, \quad \Rightarrow \quad \frac{\bar{\omega}_0}{\omega_{\min}} \ll e^{1/|C|}. \tag{5.38}$$

Even if $\epsilon_j \ll \beta_j$ is enforced only moderately, this condition is not very restrictive. We should therefore expect a step in the conductance even if $f(\mathbf{r})$ and $g(\mathbf{r})$ are more than just "slightly" different!

In the following, we will examine the particular case $f(\mathbf{r}) = g(\mathbf{r})$, i.e., $\lambda_j = \lambda\beta_j/m_0\omega_0^2$, see Eq. (5.25), for which the small-frequency behavior changes quite dramatically. (This is the case most different from Chapter 4.) Then we have $\ell_j = 0$, and thus

$$B^R(\omega) = \ell^2 m_0 \left(\frac{\omega^2}{\omega^2 - \bar{\omega}_0^2 - \bar{\mathcal{S}}(\omega)} - 1\right), \tag{5.39}$$

[2]If we denote L as the range over which the equilibrium positions of the substrate surface are displaced (i.e., the size of the "box" outside of which there are no forces), then $\omega_{\min} \sim v_s/L$, where v_s is the sound velocity.

which leads to

$$B(\omega) = -\frac{4g}{\bar{\omega}_0} \frac{\omega^2[1+n_B(\omega)]\,\mathrm{Im}\bar{\mathcal{S}}(\omega)}{\left[\omega^2 - \bar{\omega}_0^2 - \mathrm{Re}\bar{\mathcal{S}}(\omega)\right]^2 - [\mathrm{Im}\bar{\mathcal{S}}(\omega)]^2}. \tag{5.40}$$

Here, we have defined the experimental parameter

$$g \equiv \frac{1}{2}\ell^2 \frac{m_0\bar{\omega}_0}{\hbar} = \frac{1}{2\hbar}\frac{\lambda^2\bar{\omega}_0}{m_0\omega_0^4}, \tag{5.41}$$

which is a measure of how much the equilibrium position of the molecular vibrational mode is shifted compared to the oscillator quantum $\sqrt{\hbar/m_0\bar{\omega}_0}$. Note the appearance of both the renormalized and bare frequency in Eq. (5.41) and thus in Eq. (5.40).

One can then find $F(t)$ from Eq. (5.37). For large times t, the integral in the exponent is convergent and yields a nonzero finite number since $\mathrm{Im}\bar{\mathcal{S}}(\omega) \propto \omega$ for small frequencies in the case of coupling to a semi-infinite substrate, see Chapter 4. In particular, we obtain

$$\lim_{t\to\infty} F(t) = \exp\left(\frac{4g}{\bar{\omega}_0}\int_{-\infty}^{\infty}\frac{d\omega}{2\pi}\frac{\omega^2[1+n_B(\omega)]\,\mathrm{Im}\bar{\mathcal{S}}(\omega)}{\mathcal{G}(\omega)}\right), \tag{5.42}$$

where we defined

$$\mathcal{G}(\omega) \equiv \left[\omega^2 - \bar{\omega}_0^2 - \mathrm{Re}\bar{\mathcal{S}}(\omega)\right]^2 - [\mathrm{Im}\bar{\mathcal{S}}(\omega)]^2 \tag{5.43}$$

for the convenience of shorter formulas. Thus, we expect a δ-function at $\omega = 0$, which in turn results in a finite step-like discontinuity in the I-V curves at zero temperature according to Eqs. (5.30) and (5.31). We define

$$f(t) = F(t) - \lim_{t\to\infty} F(t), \tag{5.44}$$

and thus obtain at zero temperature:

$$F(\omega) = 2\pi\left(\lim_{t\to\infty} F(t)\right)\delta(\omega) + f(\omega), \tag{5.45}$$

with

$$f(\omega) = -\frac{4g}{\bar{\omega}_0}\frac{\omega^2\,\mathrm{Im}\bar{\mathcal{S}}(\omega)}{\mathcal{G}(\omega)}\left(\lim_{t\to\infty}F(t)\right) - \frac{4g}{\omega\bar{\omega}_0}\int_0^\omega \frac{d\xi}{2\pi}f(\xi)\frac{(\omega-\xi)^3\,\mathrm{Im}\bar{\mathcal{S}}(\omega-\xi)}{\mathcal{G}(\omega-\xi)}. \tag{5.46}$$

This implies that $f(\omega) \propto \omega^3$ for small ω. For small g, we can actually approximate $f(\omega)$ by the first term, since the other terms are of higher order in g.

The resulting discontinuity ΔI in the I-V characteristics calculated from Eq. (5.30) and measured in units of $I_N = e\Gamma_L\Gamma_R/(\Gamma_L+\Gamma_R)$ is given by

$$\frac{\Delta I}{I_N} = 2\,\mathrm{sign}(V)\left(\lim_{t\to\infty}F(t)\right)\frac{1+\Gamma_L/\Gamma_R}{2+\Gamma_L/\Gamma_R}. \tag{5.47}$$

We explicitly calculate ΔI for the case of a C_{60} molecule attached to a gold substrate, which is shown in Fig. 5.4 as a function of the experimental parameter g. The curves are parametrized by the spread D/D_0 of the van der Waals force over the surface of the substrate, see Eqs. (5.15) and (5.42). However, the dependence of the jump ΔI on D/D_0 is only weak, and the size is comparable to the step size encountered in the case without coupling to the environment, for which we had the same formula as above with $\lim_{t\to\infty}F(t) = e^{-g}$, see Chapter 4. The discontinuity appears at the voltage $eV = \pm 2\varepsilon_0$ for symmetric bias voltage $V_{L,R} = \pm V/2$, but is not present for $\varepsilon_0 = 0$ for reasons of symmetry.

Unless suppressed for reasons of device geometry, such a discontinuity at onset of conduction should be visible experimentally for weak tunneling into and out of the dot even when the effect of finite tunneling rates Γ is taken into account. Following the derivations by Meir and Wingreen [23], the differential conductance line shape is given by $A(\omega)\Gamma$, where $A(\omega)$ is the spectral function of the molecule. Taking the ground state phonon overlap η from Eq. (5.3) into account, it can be

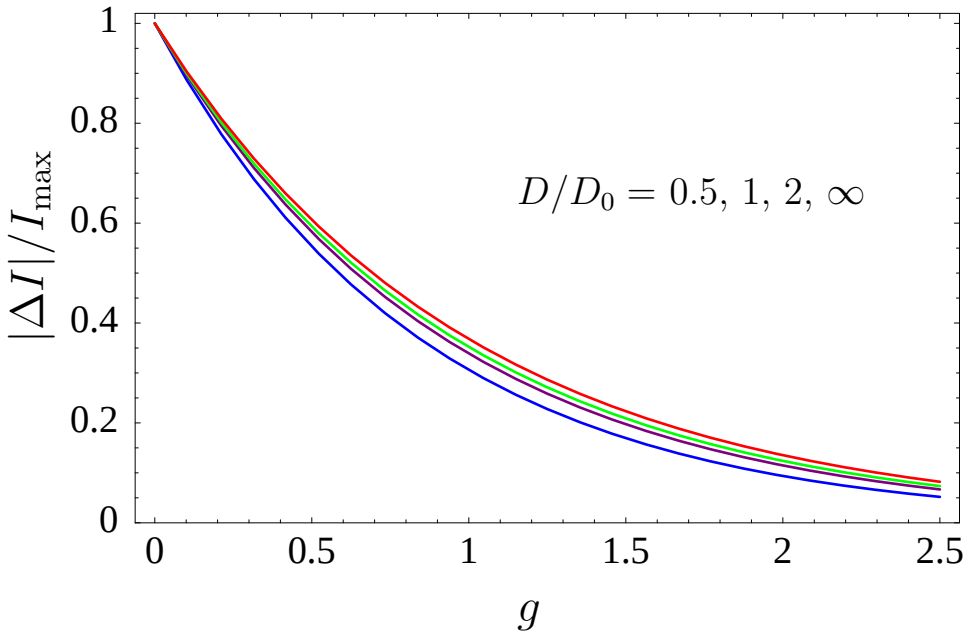

Figure 5.4: Size of the discontinuity in the I-V characteristics.

We depict the size of the discontinuity $|\Delta I|$ at $eV = \pm 2\varepsilon_0$ (see Fig. 5.3) calculated for a C_{60} molecule on gold, with symmetric tunneling contacts $\Gamma_L = \Gamma_R$ (in units of the maximum current through the molecule $I_{\max} = 4I_N/3$) as a function of g and the particular choices $D/D_0 = 0.5,\ 1,\ 2,\ \infty$ (bottom to top). The large D/D_0 limit coincides with the case of no vibrational coupling to the environment for which we have $|\Delta I| \propto e^{-g}$. The dependence on D/D_0 is rather weak but still visible.

shown that [14]

$$A(\omega) \sim \frac{\Gamma|\eta|^4}{\omega^2 + \Gamma^2|\eta|^4/4}. \tag{5.48}$$

Thus, the weight of the differential conductance step scales as $|\eta|^2$, whereas the characteristic width of the steps scales as $\Gamma|\eta|^2$. For small enough Γ compared to the width of the first Franck-Condon step in the I-V curve, we therefore see that we recover a sharp step-like discontinuity in the I-V curve. We can estimate Γ by virtue of the maximum current through the molecule $I_{\max} \sim e\Gamma$, which yields $\hbar\Gamma \sim 0.1\mu$eV since $I_{\max} \sim 100$pA for the experimental setup by Park *et al.* [2]. The Franck-Condon steps, on the other hand, feature a source-drain voltage width on the order of mV in the I-V curves [2], so that the discontinuity in the I-V curve will remain sharp even for finite tunneling.

5.5 Summary and Discussion

We have found that inclusion of the effects due to screening of the charge on the molecule can change the qualitative form of dissipation with which the molecular vibrational mode is faced. Such screening effects can be mediated by static surface charges on the substrate, or by surface charges that are induced in the substrate by the charge on the molecule. If the distribution functions that characterize the spatial form of the electrostatic interaction and of the van der Waals interaction of the molecule with the substrate are not too much different from each other, we encounter a step in the I-V curves at the onset of conduction. Such a discontinuity should be observable experimentally in the weak tunneling limit even with smearing due to finite tunneling effects. This is a result qualitatively different from treating the electrostatic forces as an external influence on the molecule-substrate system.

The step size is dependent on the experimental parameter g that reflects the shift of the equilibrium position of the molecular mode compared to the oscillator quantum $m_0\bar{\omega}_0$ and features an exponential dependence on g similar to what one would obtain for the case of no coupling to the environment. The exponent is weakly dependent on the spread D/D_0 of the van der Waals coupling between molecular mode and substrate modes, and we recover the decoupled limit for $D/D_0 \to \infty$ as expected from our results in Chapter 4.

However, we also find that the results in Chapter 4 are not changed qualitatively (but can be changed quantitatively) if the electrostatic interaction is very long ranged compared to the van der Waals interaction, and we recover a power law for the current at onset of conduction. In particular, the limit $\lambda_j \to 0$ implicitly taken in Chapter 4 is explicitly seen to coincide with treating the electrostatic interaction as an external influence on the system that breaks translational invariance.

The data in Ref. [2] do not exhibit a step in the I-V characteristics and thus feature agreement with the case of an external force as chosen in Chapter 4. It is quite possible, however, that in other experimental realizations, van der Waals interaction and electrostatic interaction are of comparable range, without the geometry of the system suppressing the effects that we found to arise due to the absence of external forces. According to our calculations, one would then indeed observe a significant step in the I-V curve at the onset of conduction.

BIBLIOGRAPHY

[1] M. A. Reed, C. Zhou, C. J. Muller, T. P. Burgin, and J. M. Tour, Science **278**, 252 (1997).

[2] H. Park, J. Park, A. K. L. Lim, E. H. Anderson, A. P. Alivisatos, and P. L. McEuen, Nature **407**, 57 (2000).

[3] J. Park, A. N. Pasupathy, J. I. Goldsmith, C. Chang, Y. Yaish, J. R. Petta, M. Rinkoski, J. P. Sethna, H. D. Abruna, P. L. McEuen, and D. C. Ralph, Nature **417**, 722 (2002).

[4] W. Liang, M. P. Shores, M. Bockrath, J. R. Long, and H. Park, Nature **417**, 725 (2002).

[5] R. H. M. Smit, Y. Noat, C. Untiedt, N. D. Lang, M. C. van Hemert, and J. M. van Ruitenbeek, Nature **419**, 906 (2002).

[6] N. B. Zhitenev, H. Meng, and Z. Bao, Phys. Rev. Lett. **88**, 226801 (2002).

[7] A. N. Pasupathy, J. Park, C. Chang, A. V. Soldatov, S. Lebedkin, R. C. Bialczak, J. E. Grose, L. A. K. Donev, J. P. Sethna, D. C. Ralph, and P. L. McEuen, Nano Lett. **5**, 203 (2005).

[8] L. H. Yu and D. Natelson, Nano Lett. **4**, 79 (2004).

[9] D. Boese and H. Schoeller, Europhys. Lett. **54**, 668 (2001).

[10] K. D. McCarthy, N. Prokof'ev, and M. T. Tuominen, Phys. Rev. B **67**, 245415 (2003).

[11] A. Mitra, I. Aleiner, and A. J. Millis, cond-mat/0302132.

[12] S. Braig and K. Flensberg, Phys. Rev. B **68**, 205324 (2003).

[13] V. Aji, J. E. Moore, and C. M. Varma, cond-mat/0302222.

[14] K. Flensberg, Phys. Rev. B **68**, 205323 (2003).

[15] A. Mitra, I. Aleiner, and A. J. Millis, Phys. Rev. B **69**, 245302 (2004).

[16] V. L. Gurevich and H. R. Schober, Phys. Rev. B **57**, 11295 (1998).

[17] K. R. Patton and M. R. Geller, Phys. Rev. B **67**, 155418 (2003).

[18] A. A. Louis and J. P. Sethna, Phys. Rev. Lett. **74**, 1363 (1995).

[19] N. W. Ashcroft and N. D. Mermin, *Solid State Physics* (Saunders College Publishing, Orlando, 1976), p. 437-440.

[20] J. D. Jackson, *Classical Electrodynamics* (John Wiley & Sons, Inc., New York, 1999), chapter 4.

[21] G. D. Mahan, *Many-Particle Physics*, 2nd ed. (Plenum Press, New York, 1990).

[22] S. M. Girvin, L. I. Glazman, M. Jonson, D. R. Penn, and M. D. Stiles, Phys. Rev. Lett. **64**, 3183 (1990).

[23] Y. Meir and N. S. Wingreen, Phys. Rev. Lett. **68**, 2512 (1992).

Chapter 6

Electron-Phonon Scattering in Metallic Carbon Nanotubes

6.1 Introduction

Carbon nanotubes have inspired a vast amount of research in recent years since they display a very rich spectrum of phenomena, one of which is the influence of phonons. The effects due to the presence of phonons can be observed experimentally in thermal transport [1, 2, 3], Raman scattering [4], and electron transport [5, 6, 7], to name only three examples. In fact, electron-phonon coupling is predicted to lead to a Peierls instability [8, 9, 10], superconductivity [11, 12], and to contribute to the resistivity of nanotubes [5, 13, 14, 15]. For the resistivity, we need to distinguish between the different types of phonons. At room temperature, the low-bias resistivity is believed to be determined by the low-energy acoustic phonons since the other high-energy phonons (such as breathing modes, optical phonons, or zone-boundary phonons) are not thermally populated at these temperatures nor can they be created due to the limited bias voltage. Both experimental mea-

surements and theoretical estimates suggest that the acoustic-phonon scattering is weak with long mean free paths on the order of several hundred nanometers to several micrometers [5, 7, 13, 15, 16, 17, 18, 19]. At high enough bias voltages, the situation is different since high-energy phonons can be emitted. Yao *et al.* [6] showed that the corresponding high-energy phonon scattering rate is rapid enough to lead to a saturation of the current, but no exact value was extracted. It is therefore of interest to accurately determine the high-energy phonon scattering length, which, in conjunction with previously determined acoustic-phonon scattering lengths, allows for making statements about the strength of the electron-phonon coupling for all types of phonons.

In a recent paper [18], the mean free paths for electrons scattering off low-energy acoustic phonons and high-energy optical and zone-boundary phonons were investigated more thoroughly for a metallic single-walled carbon nanotube (SWNT). The mean free paths in the low-bias regime (ℓ_{low}) and high-bias regime (ℓ_{high}) were extracted from the experimental I-V curves and were compared to theoretical estimates. The values that were found in this experiment suggested that ℓ_{high} is on the order of 10nm, in agreement with the general predictions of Ref. [6], and another experimental group independently found similar results [19]. Theoretical estimates for ℓ_{high} based on Fermi's Golden Rule resulted in values of the same order of magnitude, and the main subject of this chapter is to show how these theoretical estimates were obtained and how the theoretical parameters relate to experimental observables.

From Fermi's Golden rule, the natural theoretical quantity to arise is the electron-phonon scattering rate for the various types of phonons (acoustic, optical, zone boundary). Given the Fermi velocity of electrons in SWNTs, these

immediately translate to electron scattering lengths, i.e., electron mean free paths. The effect of electron-phonon scattering is apparent in the resistance of the SWNT, and since the experimental observable is the current as a function of the applied voltage, we are interested in calculating the current through the nanotube under the influence of an external electric field $\mathcal{E}$ and internal scattering as described above. We can accomplish this task by finding the occupation functions for right and left movers as a function of energy, $f^R(\varepsilon)$ and $f^L(\varepsilon)$. Without scattering and without external voltage, these occupation functions have the familiar form of Fermi-distributions with chemical potential zero across the SWNT,

$$f_0^R(\varepsilon) = f_0^L(\varepsilon) = \frac{1}{1+\exp\left(\frac{\varepsilon}{k_B T}\right)}. \tag{6.1}$$

In general, $f^R(\varepsilon)$ and $f^L(\varepsilon)$ will of course deviate from this equilibrium form, and one would have to calculate $f^R(\varepsilon)$ and $f^L(\varepsilon)$ self-consistently from the Boltzmann equation for the case of a nanotube with phonon scattering. Once we know $f^R(\varepsilon)$ and $f^L(\varepsilon)$, we can immediately write down the current I as the total charge transported by right movers minus the total charge transported by left movers,

$$\begin{aligned} I &= -4e\left(\int \frac{\mathrm{d}k}{2\pi} v_k^R f_k^R + \int \frac{\mathrm{d}k}{2\pi} v_k^L f_k^L\right) = -4ev_F\left(\int \frac{\mathrm{d}k}{2\pi} f_k^R - \int \frac{\mathrm{d}k}{2\pi} f_k^L\right) \\ &= -\frac{4e}{h}\left(\int \mathrm{d}\varepsilon f^R(\varepsilon) - \int \mathrm{d}\varepsilon f^L(\varepsilon)\right), \end{aligned} \tag{6.2}$$

where we used that $|\partial k/\partial\varepsilon| = (\hbar v_F)^{-1}$, see Sec. 1.2. The factor four is due to the fact that we have four subbands: one pair of right and left movers at each of the two Fermi point, times a factor of two for spin degeneracy. Since we only consider emission processes for optical phonons (see Sec. 6.6), and since the phonons are spinless, the two spin channels can be considered independent.[1]

[1]If we were to consider high-energy phonon absorption in addition to emission,

It turns out that calculating $f^R(\varepsilon)$ and $f^L(\varepsilon)$ is not really necessary in the high-bias and low-bias limit so that the analysis can be simplified. In these bias regimes, the following arguments were shown numerically to provide a very good approximation to what one would obtain by solving the Boltzmann equation assuming phonons in thermal equilibrium.

In the incoherent limit, the resistivity ρ_R of a 1D channel with four subbands (i.e., the SWNT) is given by [20]

$$\rho_R = \frac{h}{4e^2}\frac{1}{\ell}, \tag{6.3}$$

where ℓ is the mean free path for backscattering. (This expression can be obtained analytically for low-energy acoustic phonons by solving the Boltzmann equation.) In the low-bias regime, and for long enough channel lengths, one can then deduce the low-bias scattering length ℓ_{low} from Eq. (6.3) and the low-bias resistance $R_{\text{low}} = \mathrm{d}V/\mathrm{d}I$, the latter of which is extracted from the low-bias region of the measured I-V curves:

$$R_{\text{low}} = \frac{h}{4e^2}\frac{L}{\ell} + R_{\text{cont}}, \tag{6.4}$$

where L is the channel length, and R_{cont} is the contact resistance between leads and SWNT (for perfect contacts and four channels, one would expect $R_{\text{cont}} = h/4e^2$). Combination of several values of R_{low} for different channel lengths L allows for determining the slope ρ_R, which then immediately translates to ℓ_{low}. (The ubiquitous contact resistance simply shows up as a constant resistance offset.)

we would have to take into account that phonons created in one spin channel could cause scattering in either of the two spin channels. For the low-energy acoustic phonons, on the other hand, we do have to include both emission and absorption processes. Nonetheless, the two spin channels can be considered independent since the equilibrium phonon distribution features many phonons at these low energies anyway.

Since the acoustic phonons with wave vector $q \approx 0$ are low-energy phonons, we do not need to worry about the electrons having to be accelerated to a certain energy by the applied electric field before they can scatter.

The situation is quite different for optical and zone-boundary phonons because of their finite energies $\hbar\omega \gg k_B T$. These high-energy phonon states are to good approximation not populated at all, see Sec. 6.6, so that the only possibility for scattering off these phonons is by virtue of emission processes. Thus, for backscattering to occur, the electrons first need to attain the phonon energy in the electric field, which implies that they need to travel a length

$$\ell_T = \frac{\hbar\omega}{eV} L. \tag{6.5}$$

If we denote the mean free path for scattering off the high-energy phonons as ℓ_{hp}, then the total scattering length in the high-bias regime ℓ_{high} is given by

$$\ell_{\mathrm{high}} = \ell_T + \ell_{\mathrm{hp}}. \tag{6.6}$$

For long channel lengths $L \gg \ell_{\mathrm{hp}}$, we see that ℓ_T is large, so that the high-bias scattering length is mostly determined by ℓ_T. In this case we expect current saturation with saturation current $I_0 = (4e/h)\hbar\omega$ since

$$R_{\mathrm{high}} = R_{\mathrm{low}} + \frac{h}{4e^2}\frac{L}{\ell_T} = R_{\mathrm{low}} + \frac{V}{I_0}. \tag{6.7}$$

For short channel lengths L, on the other hand, we would expect that the electrons attain the energy necessary for scattering almost immediately. This implies that ℓ_{high} is completely determined by ℓ_{hp}, the high-energy phonon scattering length. In the experiment of Ref. [18], channel lengths of less than 500nm are assumed to fulfill this criterion of short channel lengths, and the high-energy phonon scattering length can thus be read off the high-bias part of the I-V curves. The

analysis proceeds analogously to the low-bias regime, with

$$R_{\text{high}} = R_{\text{low}} + \frac{h}{4e^2}\frac{L}{\ell_{\text{hp}}}. \tag{6.8}$$

6.2 Electron-Phonon Scattering Hamiltonian

Given the simple yet reliable connection between scattering length and I-V curves, the only remaining task at hand is the calculation of the scattering rate. The interaction between electrons and phonons can be described by the following interaction Hamiltonian:

$$H_{\text{eph}} = \sum_{\mathbf{k},\mathbf{q},\alpha} D^{\alpha}_{\mathbf{k},\mathbf{q}} c^{\dagger}_{\mathbf{k}+\mathbf{q}} c_{\mathbf{k}} u^{\alpha}_{\mathbf{q}}, \qquad \text{with } u^{\alpha}_{\mathbf{q}} = \sqrt{\frac{\hbar}{2L\rho\omega^{\alpha}_{\mathbf{q}}}}\left(b_{\mathbf{q}} + b^{\dagger}_{-\mathbf{q}}\right), \tag{6.9}$$

where $\mathbf{q}$ and α label the phonon wave vector and branch, respectively, $u^{\alpha}_{\mathbf{q}}$ is the phonon displacement, $\omega^{\alpha}_{\mathbf{q}}$ is the phonon frequency, $c^{\dagger}$ and c ($b^{\dagger}$ and b) are electron (phonon) creation and annihilation operators, respectively, $D^{\alpha}_{\mathbf{k},\mathbf{q}}$ is the matrix element describing electron-phonon scattering, L is the length of the SWNT, and ρ is its linear mass density.

The normalization factor that appears in the phonon displacement can be derived from diagonalizing the Hamiltonian for a bath of harmonic oscillators, see for instance Ref. [21], but we can also give a more intuitive argument [22]. (From here on, the indices "ac", "opt", and "zb" refer to acoustic, optical, and zone-boundary phonons, respectively.) The displacement $u(r,t)$ of an atom along a one-dimensional system due to an acoustic phonon of wave vector q and frequency ω_q can be written as a cosine wave,

$$u^{\text{ac}}_{q}(r,t) = u^{\text{ac}}_{0}\cos(qr - \omega_q t). \tag{6.10}$$

The total energy stored in the phonon at any time t must be equal to $\hbar\omega_q$. Since average potential energy and average kinetic energy are equal, we can write

$$2\sum_{\{\vec{R}_i\}}\frac{1}{2}m\omega_q^2\overline{[u_q^{\rm ac}(r,t)]^2}=\hbar\omega_q,\qquad\Rightarrow\sum_{\{\vec{R}_i\}}m\omega_q^2u_0^2\cos^2(qr)=\hbar\omega_q. \tag{6.11}$$

Performing the sum over all lattice sites, we see that

$$u_0^{\rm ac}=\sqrt{\frac{2\hbar}{Nm\omega_q}}, \tag{6.12}$$

where N is the number of lattice sites.

The procedure is very much the same for optical phonons or zone-boundary phonons: within each unit cell, they feature *relative* displacements

$$u_q^{\rm op,zb}(r,t)=u_0^{\rm op,zb}v(r)\cos(qr-\omega_qt), \tag{6.13}$$

where $v(r)$ represents the phase difference between the basis atoms in each unit cell with $|v(r)|=1$. (Since $u_q^{\rm op,zb}(r,t)$ is the relative displacement, each atom is displaced by $\frac{1}{2}u_q^{\rm op,zb}(r,t)$.) In the energy argument, we need to replace the mass m by the reduced mass $\mu=\frac{1}{2}m$, and the final summation over lattice sites results in a factor $N/2$ since each unit cell contains two atoms, so that

$$u_0^{\rm op,zb}=\sqrt{\frac{8\hbar}{Nm\omega_q}}. \tag{6.14}$$

This is the normalization per *unit cell*, as pointed out above, which is why the normalization *per atom* is the same as for the acoustic phonons, and we define

$$u_0^{\rm cos}\equiv\sqrt{\frac{2\hbar}{Nm\omega_q}}. \tag{6.15}$$

In order to relate this result to the scattering Hamiltonian (6.9), we need to switch notation to traveling waves rather than standing waves:

$$u_0^{\rm cos}\cos(qr-\omega_qt)=\frac{u_0^{\rm cos}}{2}\left(e^{iqr-i\omega_qt}+e^{-iqr+i\omega_qt}\right), \tag{6.16}$$

which finally leads to the appropriate normalization factor

$$u_0 = \sqrt{\frac{\hbar}{2Nm\omega_q}} = \sqrt{\frac{\hbar}{2L\rho\omega_q}}. \tag{6.17}$$

6.3 Relevant Scattering Processes

For application to electron transport through metallic SWNTs, the electron wave vectors $\mathbf{k}$ and $\mathbf{k}+\mathbf{q}$ in the Hamiltonian (6.9) are taken in the vicinity of the Fermi points of the SWNT. Electron-phonon scattering takes place from an initial electron state with wave vector $\mathbf{k}$ and energy $\varepsilon_{\mathbf{k}}$ to a final electron state with wave vector $\mathbf{k}+\mathbf{q}$ and energy $\varepsilon_{\mathbf{k}+\mathbf{q}}$. Energy conservation dictates that

$$\varepsilon_{\mathbf{k}+\mathbf{q}} = \varepsilon_{\mathbf{k}} \pm \hbar\omega_{\mathbf{q}}^{\alpha}, \tag{6.18}$$

where the plus sign refers to absorption of a phonon with energy $\hbar\omega_{\mathbf{q}}^{\alpha}$ and wave vector $\mathbf{q}$, whereas the minus sign refers to emission of a phonon with wave vector $-\mathbf{q}$.

Combining momentum and energy conservation, we find that indeed only a very limited number of phonon modes can take part in the backscattering processes. There are two distinct Fermi points in the electronic band structure of a metallic SWNT, so that backscattering in a metallic SWNT with approximately half-filled electronic bands can either occur within each energy cone at the Fermi points or between the two energy cones at the two distinct Fermi points (see Fig. 1.4 in Sec. 1.2 for a depiction of the cone structure). Due to the quantization of transverse phonon momenta in the nanotube, electron-phonon backscattering can, in fact, only occur involving a phonon with wave vector parallel to the nanotube orientation. Thus, only *one* phonon mode per branch is allowed by energy

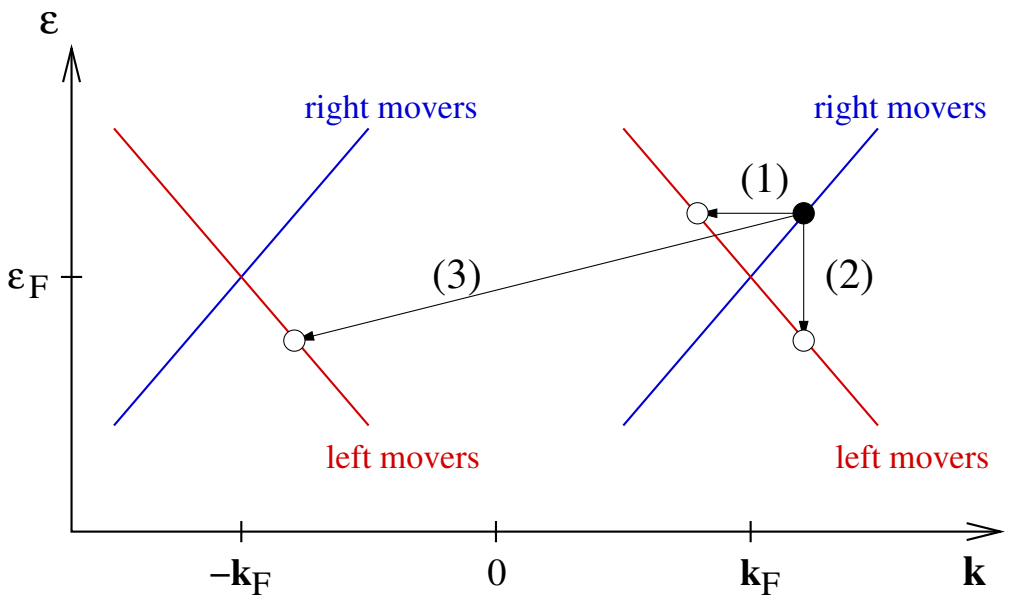

Figure 6.1: Sketch of the possible phonon scattering processes for right movers at approximately half-filled bands.

The numbers refer to: (1) emission and absorption of acoustic phonons with low energy and small momentum, (2) emission of optical phonons with high energy and small momentum, and (3) emission of zone-boundary phonons with high energy and large momentum.

and momentum conservation and we can approximate the band structure by the "crosses" depicted in Figs. 1.7 and 6.1.

In Fig. 6.1, we display the phonon scattering processes with which a right-moving electron can be faced at approximately half-filled bands (the following numbers in parentheses refer to Fig. 6.1): (1) emission and absorption of acoustic phonons with low energy and small momentum, (2) emission of optical phonons with high energy and small momentum, and (3) emission of zone-boundary phonons with high energy and large momentum. We only need to include the low-energy acoustic phonons with $\hbar\omega_{\mathbf{q}} \propto q$ since numerical simulations yielded [18] that the scattering rate is approximately zero for phonons at the zone boundary associated with the acoustic branch. The reason why only emission plays a role for the high-energy optical and zone-boundary phonons is exactly the fact that they are high-energy phonons, see also Sec. 6.6: assuming an equilibrium Bose-Einstein phonon distribution, these high-energy states are not occupied since $\hbar\omega_{\mathrm{opt}}, \hbar\omega_{\mathrm{zb}} \gg k_B T$ at room temperature.

6.4 Band Gap and Scattering Matrix Element

Having identified the relevant phonon modes in Sec. 6.3, the remaining task is to calculate the scattering matrix element $D^{\alpha}_{\mathbf{k},\mathbf{q}}$ for these modes. As mentioned before, all the scattering occurs either as intra-cross scattering or inter-cross scattering, see Fig. 6.1. For intra-cross scattering, we can write down a simplified scattering Hamiltonian by making use of basis wave functions describing right-moving and

left-moving electrons,

$$\begin{pmatrix} \varepsilon_{R,\mathbf{k}} & t_{\mathbf{q}} \\ t_{\mathbf{q}}^* & \varepsilon_{L,\mathbf{k}+\mathbf{q}} \end{pmatrix}. \tag{6.19}$$

Here $\varepsilon_{R/L,k}$ are the energies of right movers and left movers, respectively, with $\varepsilon_{R,k_F} = \varepsilon_{L,k_F}$ and k-dependence as described in Sec. 1.2, and the off-diagonal matrix $t_{\mathbf{q}}$ elements describe transitions between right movers and left movers, which is simply backscattering due to phonons of wave vector $\mathbf{q}$. If no backscattering mechanism exists, i.e., $t_{\mathbf{q}} = 0$, then right movers and left movers do not interact with each other, and the matrix is diagonal. Nonzero $t_{\mathbf{q}}$, on the other hand, introduces a band gap and lifts the degeneracy at $k = k_F$. The new two eigenenergies are simply

$$\frac{\varepsilon_{R,\mathbf{k}} + \varepsilon_{L,\mathbf{k}+\mathbf{q}}}{2} \pm \frac{\sqrt{\left(\varepsilon_{R,\mathbf{k}} - \varepsilon_{L,\mathbf{k}+\mathbf{q}}\right)^2 + 4|t_{\mathbf{q}}|^2}}{2}, \tag{6.20}$$

with a band gap $\Delta_{\mathbf{q}}$ equal to $2|t_{\mathbf{q}}|$, see also Fig. 6.2.

For inter-cross scattering, which involves zone-boundary phonons with wave vector $\mathbf{q} \approx \pm 2\mathbf{k}_F$, we can write down a similar Hamiltonian structure, only that in this case right movers and left movers from different bands participate in the scattering process,

$$\begin{pmatrix} \varepsilon_{R,\mathbf{k}_1} & t_{\mathbf{q}} & 0 & 0 \\ t_{\mathbf{q}}^* & \varepsilon_{L,\mathbf{k}_1+\mathbf{q}} & 0 & 0 \\ 0 & 0 & \varepsilon_{R,\mathbf{k}_2} & t_{\mathbf{q}} \\ 0 & 0 & t_{\mathbf{q}}^* & \varepsilon_{L,\mathbf{k}_2+\mathbf{q}} \end{pmatrix}. \tag{6.21}$$

The Hamiltonian is block diagonal, and we can diagonalize the Hamiltonian just as in the intra-cross case, leading to the same band gap(s) $\Delta_{\mathbf{q}} = 2|t_{\mathbf{q}}|$.

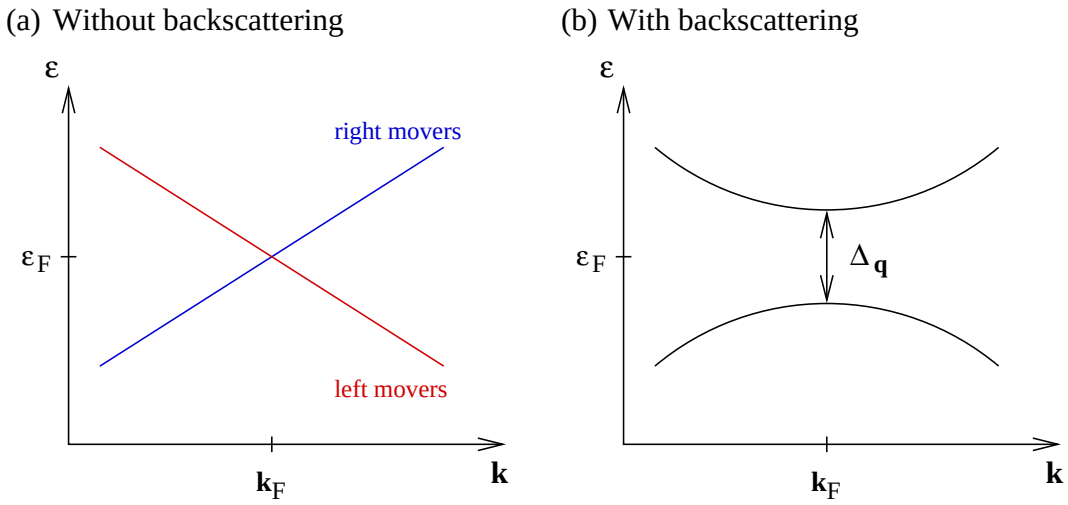

Figure 6.2: Sketch of the electronic band structure in a metallic SWNT with and without backscattering.

(a) Without backscattering, right movers and left movers are not coupled and we have the familiar "cross" structure at the Fermi point. **(b)** If, on the other hand, backscattering occurs, then right movers and left movers are no longer exact eigenstates of the Hamiltonian. Rather, the cross structure is split into an upper band and a lower band with band gap $\Delta_{\mathbf{q}}$.

It is the aforementioned band gap that can be obtained from numerical band structure calculations. Such calculations were not done for a nanotube structure, but rather for a graphene sheet with periodic boundary conditions. The resulting electronic band structure had been shown to be be in agreement with what one would expect for nanotubes as long as breathing modes could be neglected. In particular, it featured the double-cross structure as depicted in Figs. 1.7 and 6.1. Within this numerical framework, the atoms in the graphene sheet were displaced from their equilibrium positions according to a zone-boundary, optical, or acoustic mode with amplitude a_p, and the resulting electronic band structure indeed revealed a gap $\Delta_{\mathbf{q}}$. As argued above, this gap is exactly twice $|t_{\mathbf{q}}|$.

If the numerical simulations had been done using traveling waves, the potential term $D^{\alpha}_{\mathbf{k},\mathbf{q}}$ would follow immediately from the above, since $D^{\alpha}_{\mathbf{k},\mathbf{q}}$ is nothing but "$|t_{\mathbf{q}}|$ per unit displacement", so that we would simply have

$$D^{\alpha}_{\mathbf{k},\mathbf{q}} = \frac{\Delta_{\mathbf{q}}}{2a_p}. \tag{6.22}$$

However, the numerical calculations could only deal with *real* displacements, and thus had to use cosine wave functions as opposed to complex exponentials. This leads to the subtle effect of having to include additional factors of $\sqrt{2}$ for zone-boundary phonons, as we will discuss in Sec. 6.5.

For acoustic phonons, we can relate the quantity $D^{\mathrm{ac}}_{\mathbf{k},\mathbf{q}}$ to the so called *deformation potential* Ξ, which is a measure of the uniform strain that acoustic phonons induce in a nanotube,

$$D^{\mathrm{ac}}_{\mathbf{k},\mathbf{q}} = \Xi \cdot q. \tag{6.23}$$

The reason why such a definition works for acoustic phonons but not for optical or zone-boundary phonons is that carbon atoms in the nanotube are displaced

only slightly differently than their nearest neighbors for acoustic phonons, whereas they are displaced nearly completely out of phase for optical and zone-boundary phonons. Thus the concept of "uniform strain" only makes sense for acoustic phonons.

6.5 Fermi's Golden Rule and Factors of Two

Without including the effects of thermal averaging and population numbers, Fermi's Golden Rule as applied to the scattering Hamiltonian (6.9) immediately leads to the following "bare" backscattering rate for each contributing phonon mode,

$$\frac{1}{\tau^{\alpha}_{\mathbf{q},0}} = \frac{2\pi}{\hbar}\left(\frac{\hbar}{\rho\omega_{\mathbf{q}}}\right)\frac{1}{hv_F}|D^{\alpha}_{\mathbf{k}_F,\mathbf{q}}|^2, \tag{6.24}$$

where we used that scattering takes place only close to the Fermi surface.

In order to obtain this result, we need to calculate square matrix elements of the form

$$|\langle k_R|H_{\text{eph}}|k'_L\rangle|^2, \tag{6.25}$$

where the indices R and L denote right and left movers, respectively. It is important that the states used for the calculation of such matrix elements are properly normalized, which is why we need to examine the ramifications of using cosine waves for our numerical calculations more carefully.

6.5.1 Zone-boundary phonons with nonzero $\mathbf{q} \approx \pm 2\mathbf{k}_F$

Let $s_q^\dagger$ and s_q be creation and annihilation operators that create a cosine wave from the vacuum $|0\rangle$. Then the "natural" normalization of this wave is

$$\langle 0|s_q s_q^\dagger|0\rangle = \int \mathrm{d}r \langle 0|s_q|r\rangle\langle r|s_q^\dagger|0\rangle = \int \mathrm{d}r \cos^2(qr) = \frac{1}{2}. \tag{6.26}$$

For any quantity that is calculated using cosine waves, we therefore need to include an additional normalization factor $\sqrt{2}$ each time a cosine state enters the calculation in order to ensure proper normalization. This normalization factor enters the scattering rate in the square, see (6.25), and we thus need to modify the value we obtained for $D^{\mathrm{zb}}_{\mathbf{k},\mathbf{q}}$ in Sec. 6.4, see Eq. (6.22), by a factor of $\sqrt{2}$.

In addition, we neglected the fact that we do not only have cosine standing waves but also sine standing waves. These sine waves backscatter electrons exactly the same way cosine waves do, so that the scattering rate needs to be modified by an additional factor of two, which again translates to an additional factor of $\sqrt{2}$ for $D^{\mathrm{zb}}_{\mathbf{k},\mathbf{q}}$. In summary, we therefore have for zone-boundary phonons:

$$D^{\mathrm{zb}}_{\mathbf{k},\pm 2\mathbf{k}_F} = \underbrace{\sqrt{2}}_{\cos\text{ normalization}} \cdot \underbrace{\sqrt{2}}_{\cos+\sin} \frac{\Delta_{2\mathbf{k}_F}}{2a_p} = \frac{\Delta_{2\mathbf{k}_F}}{a_p}, \tag{6.27}$$

where $\Delta_{2\mathbf{k}_F}$ is, as before, the band gap obtained from the numerical calculations for an atomic displacement of a_p from equilibrium.

6.5.2 Optical and acoustic phonons with $\mathbf{q} \approx 0$

This case is the simpler one, since in this case cosine waves and traveling waves are identical. Or in other words, $e^{i\mathbf{qr}}|_{q=0} = \cos(\mathbf{qr})|_{q=0}$. This is simply due to the fact that sine standing waves do not exist at zero wave vector. The normalization of the cosine waves is therefore naturally one, and we also do not need to correct the scattering rate for the additional influence of scattering off sine waves. Thus, we simply have

$$D^{\mathrm{ac,op}}_{\mathbf{k},0} = \frac{\Delta_0}{a_p} \tag{6.28}$$

for both acoustic and optical phonons.[2]

[2]We should mention that the numerics were run for $\mathbf{q} = 0$, where the results are expected to be valid in a small region with $q \approx 0$.

6.6 Thermal Occupation

Now that we have made the connection between the numerical results and the theoretical quantity of interest, we can proceed to include the thermal occupation factors for the various types of phonons. These are necessary for making comparisons with real experiments that are performed at room temperature.

If we denote $N^{\alpha}(\hbar\omega^{\alpha}_{\mathbf{q}})$ as the occupation factor for a phonon of branch α with energy $\hbar\omega_{\mathbf{q}}$ and wave vector $\mathbf{q}$, then we need to include the following factors for absorption and emission:

$$N^{\alpha}(\hbar\omega^{\alpha}_{\mathbf{q}}) \qquad \text{Absorption,} \tag{6.29}$$

$$1 + N^{\alpha}(\hbar\omega^{\alpha}_{\mathbf{q}}) \qquad \text{Emission.} \tag{6.30}$$

We assume the phonons to be in thermal equilibrium so that we can express $N^{\alpha}(\hbar\omega_{\mathbf{q}})$ by the Bose-Einstein distribution,

$$N^{\alpha}(\hbar\omega^{\alpha}_{\mathbf{q}}) = \frac{1}{\exp\left(\frac{\hbar\omega^{\alpha}_{\mathbf{q}}}{k_B T}\right) - 1}. \tag{6.31}$$

Depending on whether the phonons feature low energies $\hbar\omega^{\alpha}_{\mathbf{q}} \ll k_B T$ (acoustic phonons) or high energies $\hbar\omega^{\alpha}_{\mathbf{q}} \gg k_B T$ (optical and zone-boundary phonons), the occupation factors can be approximated in different ways. For low energies, we can expand the exponential and obtain

$$N^{\mathrm{ac}}(\hbar\omega^{\mathrm{ac}}_{\mathbf{q}}) \approx \frac{k_B T}{\hbar\omega^{\alpha}_{\mathbf{q}}}. \tag{6.32}$$

This immediately implies that $N^{\mathrm{ac}}(\hbar\omega^{\mathrm{ac}}_{\mathbf{q}}) \approx 1 + N^{\mathrm{ac}}(\hbar\omega^{\mathrm{ac}}_{\mathbf{q}})$, i.e., the occupation factors for emission and absorption of acoustic phonons are approximately equal. For high energy optical or zone-boundary phonons, on the other hand, we have $\exp(\hbar\omega^{\alpha}_{\mathbf{q}}/k_B T) \gg 1$, and thus

$$N^{\mathrm{op,zb}}(\hbar\omega^{\mathrm{op,zb}}_{\mathbf{q}}) \approx 0. \tag{6.33}$$

This implies that only emission processes contribute to the backscattering rate for optical and zone-boundary phonons.

6.7 Results for the Mean Free Paths

Equipped with the above results, we can write down the final theoretical expressions for the backscattering rates due to each contributing acoustic, optical and zone-boundary phonon mode:

$$\frac{1}{\tau^{\mathrm{zb}}} = \frac{2\pi}{\hbar}\left|D^{\mathrm{zb}}_{\mathbf{k}_F,\mathbf{q}_{\mathrm{zb}}}\right|^2 \left(\frac{\hbar}{2\rho\omega^{\mathrm{zb}}_{\mathbf{q}_{\mathrm{zb}}}}\right)\frac{1}{hv_F}, \tag{6.34}$$

$$\frac{1}{\tau^{\mathrm{op}}} = \frac{2\pi}{\hbar}\left|D^{\mathrm{op}}_{\mathbf{k}_F,\mathbf{q}_{\mathrm{op}}}\right|^2 \left(\frac{\hbar}{2\rho\omega^{\mathrm{op}}_{\mathbf{q}_{\mathrm{op}}}}\right)\frac{1}{hv_F}, \tag{6.35}$$

$$\frac{1}{\tau^{\mathrm{ac}}} = \frac{2\pi}{\hbar}\Xi^2 \left(\frac{k_B T}{2\rho v_s^2}\right)\frac{1}{hv_F}. \tag{6.36}$$

where $\mathbf{q}_{\mathrm{zb}} = -2\mathbf{k}_F$, $\mathbf{q}_{\mathrm{op}} = 0$, $\mathbf{q}_{\mathrm{ac}} = 0$, and we used that $\omega^{\mathrm{ac}}_{\mathbf{q}} = v_s q$, where v_s is the sound velocity. (The numerical values later in this section are all calculated for a SWNT of diameter 1.8nm.)

It turns out that several of the phonon modes that would be allowed by energy and momentum conservation to be involved in backscattering processes do not couple to the electrons:

- **Zone-boundary phonons**

  Only one of the available modes couples to the electrons, and this mode belongs to an optical branch. Contributions from other optical or acoustic branches are small and can be neglected, and we find

$$D^{\mathrm{zb}} = 25.6\frac{\mathrm{eV}}{\mathrm{\AA}}. \tag{6.37}$$

The scattering length $\ell_{\rm zb}$ of Sec. 6.1 follows as

$$\ell_{\rm zb} = v_F \tau^{\rm zb} \approx 35\text{nm}. \tag{6.38}$$

This value does not depend on the type of nanotube as long as the nanotube is metallic [18].

- **Optical phonons**

Just as in the case of zone-boundary phonons, only one of the two degenerate modes at $\mathbf{q} = 0$ couples to the electrons. In accord with Ref. [23], we identified this mode as the longitudinal mode. A simple symmetry argument for why this is the case is given in Appendix B. We find

$$D^{\rm op} = 12.8 \frac{\text{eV}}{\text{Å}}, \tag{6.39}$$

which results in a scattering length

$$\ell_{\rm op} = v_F \tau^{\rm op} \approx 180\text{nm}. \tag{6.40}$$

This result does not depend on the type of nanotube since an appropriate longitudinal superposition of the two degenerate modes will always couple to the electrons with the above strength.

- **Acoustic phonons**

Depending on whether we deal with armchair nanotubes or zigzag nanotubes, we need to find the deformation potential Ξ due to torsional strain or uniaxial strain, respectively. A typical value in the literature is $\Xi \approx 5\text{eV}$ [24], consistent with our own calculations. This leads to

$$\ell_{\rm ac} = v_F \tau^{\rm ac} \approx 2.4\mu\text{m}. \tag{6.41}$$

Given the simplified recipe of Sec. 6.1, the high-bias mean free path $\ell_{\rm high}$ for short metallic SWNTs follows from the scattering lengths for optical and zone-boundary phonons as

$$\ell_{\rm high} = \frac{1}{\frac{1}{\ell_{\rm op}} + \frac{1}{\ell_{\rm zb}}} \approx 30{\rm nm}. \tag{6.42}$$

The experimentally extracted value $\ell_{\rm high}^{\rm exp}$ =10nm is of the same order but off by a factor of three. As pointed out in Ref. [18], the difference could arise from uncertainties in the parameters of the theory or from additional scattering mechanisms not considered here. These include multiple phonon scattering or stimulated phonon emission from high energy phonons created by other scattering events. Along these lines, it may be interesting to include the effects of non-equilibrium phonons into the theoretical estimates, for instance by solving the Boltzmann equation self-consistently with such a non-equilibrium phonon distribution.[3] Preliminary estimates on the basis of how fast internal vibrational modes of molecules dissipate their energy into substrates close by [25, 26] compared to the number of scattering events that create high-energy phonons do not exclude the possibility that, in fact, non-equilibrium phonons may be needed for an accurate theoretical description. In particular for suspended nanotubes, such a description may be inevitable.

[3] As mentioned before, solving the Boltzmann equation self-consistently with an *equilibrium* phonon distribution suggests that the experimentally extracted value is correct in the regimes of low bias and high bias.

BIBLIOGRAPHY

[1] J. Hone, M. Whitney, C. Piskoti, and A. Zettl, Phys. Rev. B **59**, R2514 (1999).

[2] P. Kim, L. Shi, A. Majumdar, and P. L. McEuen, Phys. Rev. Lett. **87**, 215502 (2001).

[3] J. P. Small and L. S. P. Kim, Solid State Commun. **127**, 181 (2003).

[4] M. S. Dresselhaus and P. C. Eklund, Adv. Phys. **49**, 705 (2000).

[5] C. L. Kane, E. J. Mele, R. S. Lee, J. E. Fischer, P. Petit, H. Dai, A. Thess, R. E. Smalley, A. R. M. Verschueren, S. J. Tans, and C. Dekker, Europhys. Lett. 1998 **41**, 683 (1998).

[6] Z. Yao, C. L. Kane, , and C. Dekker, Phys. Rev. Lett. **84**, 294 (2000).

[7] J. Appenzeller, R. Martel, P. Avouris, H. Stahl, and B. Lengeler, Appl. Phys. Lett. **78**, 3313 (2001).

[8] O. Dubay, G. Kresse, and H. Kuzmany, Phys. Rev. Lett. **88**, 235506 (2002).

[9] M. T. Figge, M. Mostovoy, and J. Knoester, Phys. Rev. B **65**, 125416 (2002).

[10] J. W. Mintmire, B. I. Dunlap, and C. T. White, Phys. Rev. Lett. **68**, 631 (1992).

[11] L. Benedict, V. H. Crespi, S. G. Louie, and M. L. Cohen, Phys. Rev. B **52**, 14935 (1995).

[12] A. D. Martino and R. Egger, Phys. Rev. B **67**, 235418 (2003).

[13] R. A. Jishi, M. S. Dresselhaus, and G. Dresselhaus, Phys. Rev. B **48**, 11385 (1993).

[14] L. M. Woods and G. D. Mahan, Phys. Rev. B **61**, 10651 (2000).

[15] H. Suzuura and T. Ando, Phys. Rev. B **65**, 235412 (2002).

[16] A. Bachtold, M. S. Fuhrer, S. Plyasunov, M. Forero, E. H. Anderson, A. Zettl, and P. L. McEuen, Phys. Rev. Lett. **84**, 6082 (2000).

[17] T. Hertel, R. Fasel, and G. Moos, Appl. Phys. A: Mater. Sci. Process. **75**, 449 (2002).

[18] J.-Y. Park, S. Rosenblatt, Y. Yaish, V. Sazonova, H. Ustunel, S. Braig, T. A. Arias, P. W. Brouwer, and P. L. McEuen, Nano Lett. **4**, 517 (2004).

[19] A. Javey, J. Guo, M. Paulsson, Q. Wang, D. Mann, M. Lundstrom, and H. Dai, Phys. Rev. Lett. **92**, 106804 (2004).

[20] S. Datta, *Electronic Transport in Mesoscopic Systems* (Cambridge University Press, London, 1995).

[21] H. Bruus and K. Flensberg, *Many-body Quantum Theory In Condensed Matter Physics: An Introduction* (Oxford University Press, Oxford, 2004).

[22] J. H. Davies, *The Physics of Low-Dimensional Semiconductors: An Introduction* (Cambridge University Press, New York, 1998), chapters 2 & 8.

[23] O. Dubay and G. Kresse, Phys. Rev. B **67**, 035401 (2003).

[24] L. Yang and J. Han, Phys. Rev. Lett. **85**, 154 (2004).

[25] V. L. Gurevich and H. R. Schober, Phys. Rev. B **57**, 11295 (1998).

[26] K. R. Patton and M. R. Geller, Phys. Rev. B **67**, 155418 (2003).

Appendix A

Chapter 3: Rotation Matrices

This appendix contains the rotation matrices for transformation from the basis aligned with the quantization axis to a basis forming a relative angle θ with the original quantization axis. We restrict ourselves to the case of up to three electrons on the dot, so that we only need representations up to dimensionality four. (The four-dimensional representations correspond to the quadruplets of total spin $S = 3/2$ and $S = 1/2$ in the case of three singly occupied single-electron levels.) Also, we only consider polarizations in the xz plane, so that any superposition of single spins can be expressed in terms of real coefficients.

A.1 Two Dimensions: Spin-1/2 Doublet

In the standard basis of spin up and spin down,

$$(1,0) \equiv |\uparrow\rangle\,, \qquad (0,1) \equiv |\downarrow\rangle\,, \tag{A.1}$$

the rotation matrix is

$$R_2 = \begin{pmatrix} \cos(\theta) & \sin(\theta) \\ -\sin(\theta) & \cos(\theta) \end{pmatrix}. \tag{A.2}$$

A.2 Three Dimensions: Spin-1 Triplet

In the basis created by successively applying the spin-lowering operator S_- to $|\uparrow\uparrow\rangle$,

$$\begin{aligned} &(1,0,0) \equiv |\uparrow\uparrow\rangle\,, \\ &(0,1,0) \equiv (|\uparrow\downarrow\rangle + |\downarrow\uparrow\rangle)/\sqrt{2}, \\ &(0,0,1) \equiv |\downarrow\downarrow\rangle\,, \end{aligned} \tag{A.3}$$

the rotation matrix reads

$$R_3 = \begin{pmatrix} \cos^2(\theta) & \sqrt{2}\cos(\theta)\sin(\theta) & \sin^2(\theta) \\ -\sqrt{2}\cos(\theta)\sin(\theta) & \cos^2(\theta) - \sin^2(\theta) & \sqrt{2}\cos(\theta)\sin(\theta) \\ \sin^2(\theta) & -\sqrt{2}\cos(\theta)\sin(\theta) & \cos^2(\theta) \end{pmatrix}. \tag{A.4}$$

A.3 Four Dimensions: Spin-3/2 Quadruplet

The maximum spin-3/2 states feature electrons in three singly occupied single-electron levels, and we can write down a basis obtained by successively applying the spin-lowering operator S_- to $|\uparrow\uparrow\uparrow\rangle$,

$$\begin{aligned} &(1,0,0,0) \equiv |\uparrow\uparrow\uparrow\rangle\,, \qquad (0,1,0,0) \equiv (|\uparrow\uparrow\downarrow\rangle + |\uparrow\downarrow\uparrow\rangle + |\downarrow\uparrow\uparrow\rangle)/\sqrt{3}, \\ &(0,0,1,0) \equiv (|\uparrow\downarrow\downarrow\rangle + |\downarrow\uparrow\downarrow\rangle + |\downarrow\downarrow\uparrow\rangle)/\sqrt{3}, \qquad (0,0,0,1) \equiv |\downarrow\downarrow\downarrow\rangle\,. \end{aligned} \tag{A.5}$$

In order to make the rotation matrix fit on the page, we define the following matrices:

$$A \equiv \begin{pmatrix} \cos^3(\theta) - \cos(\theta)\sin^2(\theta) & \sqrt{3}\cos^2(\theta)\sin(\theta) \\ -\sqrt{3}\cos^2(\theta)\sin(\theta) & \cos^3(\theta) - \cos(\theta)\sin^2(\theta) \end{pmatrix},$$

$$B \equiv \begin{pmatrix} \cos(\theta)\sin^2(\theta) & 0 \\ 0 & -\cos(\theta)\sin^2(\theta) \end{pmatrix},$$

$$C \equiv \begin{pmatrix} \sqrt{3}\cos(\theta)\sin^2(\theta) & \sin^3(\theta) - \cos^2(\theta)\sin(\theta) \\ -\sin^3(\theta) + \cos^2(\theta)\sin(\theta) & \sqrt{3}\cos(\theta)\sin^2(\theta) \end{pmatrix},$$

$$D \equiv \begin{pmatrix} 0 & \cos^2(\theta)\sin(\theta) \\ \cos^2(\theta)\sin(\theta) & 0 \end{pmatrix}.$$

The rotation matrix itself then reads

$$R_{4,\frac{3}{2}} = \begin{pmatrix} A+B & C+D \\ C-D & A-B \end{pmatrix}. \tag{A.6}$$

A.4 Four Dimensions: Spin-1/2 Quadruplet

For the four-fold degenerate many-electron state with total spin $S = 1/2$ and three singly occupied single-electron levels, we write the rotation matrix in the basis

$$\begin{aligned}
(1,0,0,0) &\equiv (e^{\frac{2\pi i}{3}}\,|\uparrow\uparrow\downarrow\rangle + e^{\frac{-2\pi i}{3}}\,|\uparrow\downarrow\uparrow\rangle + |\downarrow\uparrow\uparrow\rangle)/\sqrt{3}, \\
(0,1,0,0) &\equiv (e^{\frac{-2\pi i}{3}}\,|\uparrow\uparrow\downarrow\rangle + e^{\frac{2\pi i}{3}}\,|\uparrow\downarrow\uparrow\rangle + |\downarrow\uparrow\uparrow\rangle)/\sqrt{3}, \\
(0,0,1,0) &\equiv (e^{\frac{2\pi i}{3}}\,|\uparrow\downarrow\downarrow\rangle + e^{\frac{-2\pi i}{3}}\,|\downarrow\uparrow\downarrow\rangle + |\downarrow\downarrow\uparrow\rangle)/\sqrt{3}, \\
(0,0,0,1) &\equiv (e^{\frac{-2\pi i}{3}}\,|\uparrow\downarrow\downarrow\rangle + e^{\frac{2\pi i}{3}}\,|\downarrow\uparrow\downarrow\rangle + |\downarrow\downarrow\uparrow\rangle)/\sqrt{3}.
\end{aligned} \tag{A.7}$$

The first two vectors have $S_z = 1/2$, the other two have $S_z = -1/2$. In this basis, the rotation matrix then reads

$$R_{4,\frac{1}{2}} = \begin{pmatrix} 0 & \cos(\theta) & -\frac{1}{2}\sin(\theta)\, e^{\frac{2\pi i}{3}} & 0 \\ \cos(\theta) & 0 & 0 & -\frac{1}{2}\sin(\theta)\, e^{\frac{-2\pi i}{3}} \\ \frac{1}{2}\sin(\theta)\, e^{\frac{2\pi i}{3}} & 0 & 0 & \cos(\theta) \\ 0 & \frac{1}{2}\sin(\theta)\, e^{\frac{-2\pi i}{3}} & \cos(\theta) & 0 \end{pmatrix}. \quad \text{(A.8)}$$

Appendix B

Chapter 6: Symmetry Argument for Electron-Phonon Coupling

In this appendix, we give a simple symmetry argument as to why only one of the degenerate optical phonon modes at $\mathbf{q} = 0$ couples to the electrons, and why it is the longitudinal mode.

In Fig. B.1, we depict the displacements that correspond to (a) a transverse optical mode and (b) a longitudinal optical mode in an armchair nanotube. If we displace the carbon atoms sideways in accord with a transverse mode, then the only way in which the Fermi vector $\mathbf{k}_F$ can change is by changing in length, but not by changing direction. Otherwise, the symmetry imposed by the transverse mode would be broken. In an armchair nanotube, the direction of the tube is parallel to the depicted Fermi vector $\mathbf{k}_F$, and thus the cones that describe the electronic bands at the Fermi points will simply be shifted along the direction of the nanotube. Cutting the cones along the direction of the tube does therefore *not* result in a band gap since the crossing point still resides on the tube axis. The situation is quite different for the longitudinal mode. In this case, the carbon

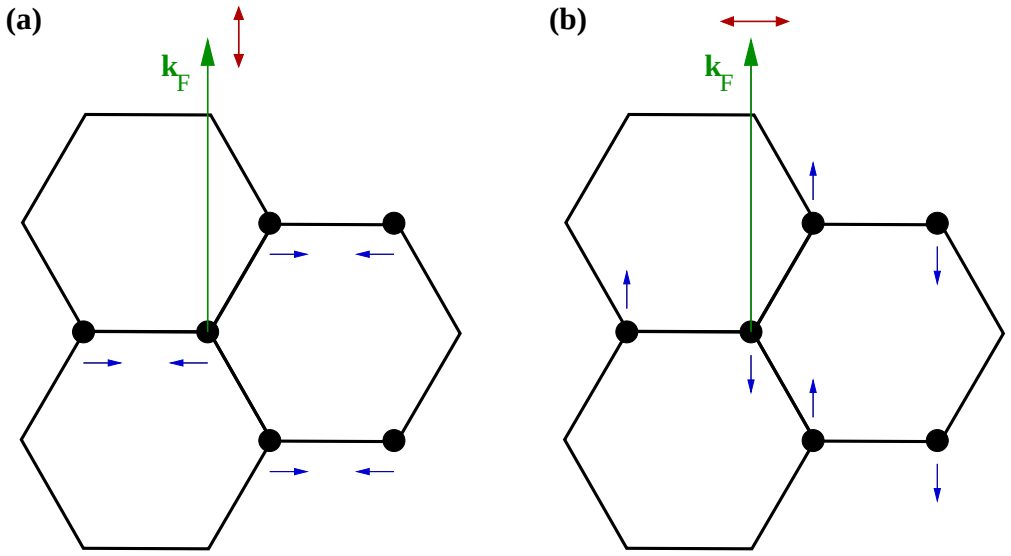

Figure B.1: Transverse and longitudinal optical mode in an armchair nanotube.

The arrows next to the carbon atoms depict the displacement of the atoms from their equilibrium positions corresponding to **(a)** a transverse optical mode or **(b)** a longitudinal optical mode. Symmetry allows the Fermi wave vector $\mathbf{k}_F$ to change only in certain directions as a result of these displacements, as indicated by the arrows next to the Fermi wave vectors. Due to the change in the Fermi vector, the mode either **(a)** does *not* induce a band gap or **(b)** does induce a band gap in the effective one-dimensional electronic band structure.

atoms are shifted back and forth along the direction of the tube, and thus symmetry demands that the Fermi vector $\mathbf{k}_F$ shift side to side away from the nanotube axis. Thus, cutting the electronic cones along the direction of the nanotube results in a band gap, which implies that we have effective backscattering coupling.

The arguments above hold for an armchair nanotube, but they can in fact be generalized to any type of tube: we can always find a linear combination of the two orthogonal modes depicted in Fig. B.1 that acts as an exactly transverse or exactly longitudinal mode for any direction of the nanotube axis.

As mentioned in Sec. 6.7, these observations also follow from performing numerical simulations for the electronic band structure of a graphene sheet in the presence of these phonon modes. We decided to elaborate on this symmetry argument because of the beauty of its simplicity.